Resonant scattering studies of ^{24}Mg and ^{28}Mg and the search for nuclear water

Joseph Walshe

A thesis submitted to
The University of Birmingham
for the degree of
Doctor of Philosophy

Nuclear Physics Group
School of Physics and Astronomy
College of Engineering and Physical Sciences
University of Birmingham
September 2015

Abstract

The neutron-rich nucleus ^{28}Mg has been studied for the first time above the particle decay threshold using α-particle resonant scattering with a beam of radioactive ^{24}Ne ions from the SPIRAL facility at GANIL. The thick target inverse kinematics technique was used to permit measurement of the differential cross section at 180° in the centre-of-mass frame, for the excitation energy region from 15 to 21 MeV, with a single beam energy. Since no previous experimental data exist with which to compare the current work, data were also taken for ^{24}Mg using a ^{20}Ne beam with the same experimental set-up. Comparison of these data with previous work yields excellent agreement and so validates the data collection method. In ^{28}Mg, energies and widths of thirteen new states are reported with relative strengths given for ten of these. For two states, spin-parity assignments are made and it is found, by calculation of the α-decay branching ratios and comparison to a theoretical model, that these two states do not appear to be strongly α clustered. The underlying structure of ^{28}Mg in this region is therefore not clear, and further experimental work is required in order to establish a full understanding, with a particular focus on the energy resolution of the measurement. The experimental technique is a powerful tool for the study of α elastic scattering cross sections, and combined with new radioactive beam facilities will prove an effective method of investigating α clustering in a wide range of unstable nuclei.

To my parents

Do not read so much, look around you and think of what you see there.

— Richard Feynman [1]

Acknowledgements

I think, on reflection, that I am really not the same person now as the one that started this Ph.D four years ago. I have learned a lot, from a lot of great people, so I will attempt to list some of them.

First and foremost, I want to thank my supervisors Martin and Carl. Martin, whose knowledge of the subject is matched only by how hard he works—perhaps that's not a coincidence. Plus, excellent taste in music! Carl, whose problem solving is tireless and unstoppable—definitely not a coincidence. Plus, excellent taste in sci-fi! A student simply couldn't ask for better supervisors.

I absolutely cannot go any further without thanking Neil, my unofficial (unwitting?) third supervisor, who has patiently explained the workings of detectors and accelerators over many a cup of tea, as well as providing lessons in unmatched patience and precision through the medium of Lego. 85,000 views and counting!

There are also a lot of people to thank who have made working in East 318 (or is it 320? 319?) a pleasure. During my stay I've played more board games, fired more Nerf darts, and climbed more routes than ever before. So to all residents of the office, be they past, present or wannabe: thank you! It's been great—from my perspective.

There are two people without whom this Ph.D would certainly not have been possible: my parents. When one ends up studying for a physics degree it puts into perspective how useful it is to have a mother who is a maths teacher and a father who worked twelve-hour days for months at a time so that I could have my own PC—even if I did use it mostly for playing games... And, of course, the world would be a better place if everyone had

the same access to baking or Lego-building advice that I do!

One final thing: at the start of this Ph.D, I entered a bet with two friends, Sean Elvidge and Jon Malcolm, concerning who could squeeze the most free travel out of their Ph.D, measured in miles travelled by plane. Since I am the last of us three to submit, I present the results of the Gentlemen's Ph.D Airmiles Wager. Congratulations to Dr Elvidge! Let it be recorded in the scientific literature that I owe you a pint.

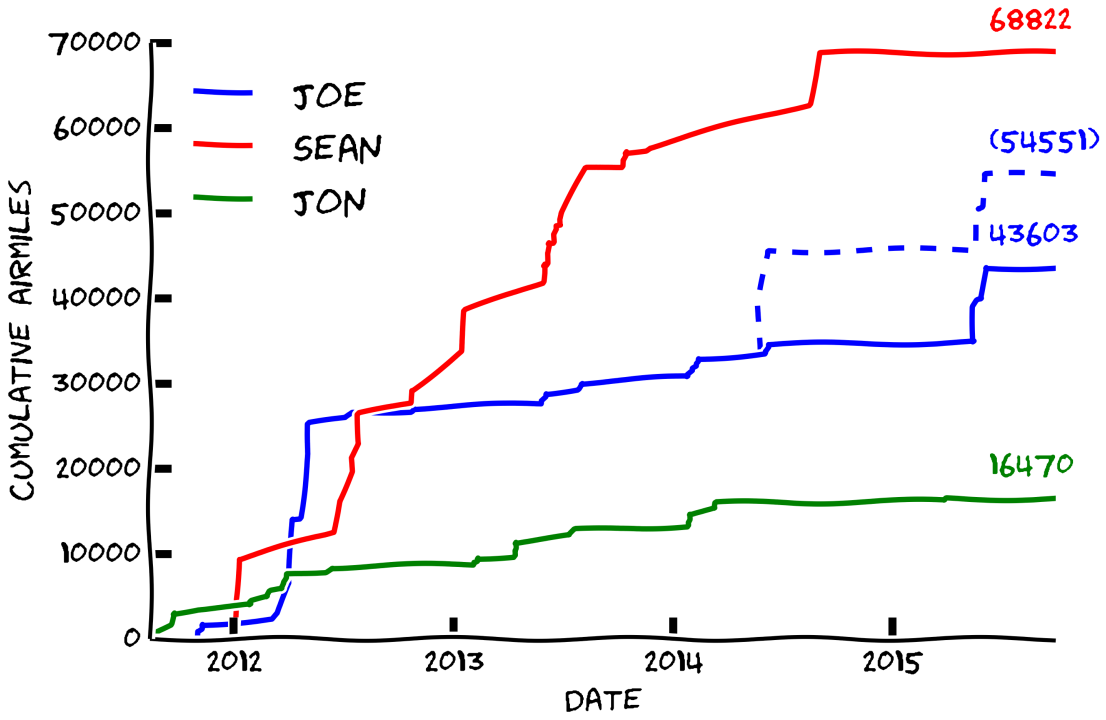

Figure 1: The results of the Gentlemens' Ph.D Airmiles Wager. The dashed line indicates what the result would have been if the author's conference in Yokohama had not been cancelled. It should be noted that the author is not bitter as he visited Japan later that year, and it wouldn't have made any difference to the wager, and anyway the experiment at GANIL was quite fun and the four broken strips on that wedge detector were an accident, really.

Publications

The work presented in this thesis has led to the following publications:

- J. Walshe *et al.*, The thick target inverse kinematics technique with a large acceptance silicon detector array, *J. Phys.: Conf. Ser.*, **569** 012052 (2014). Proceedings of the third international workshop on "State of the Art in Nuclear Cluster Physics".

- N. Curtis and J. Walshe, REX: A Monte Carlo Simulation of thick gas target resonant scattering reactions, *Nucl. Instrum. Meth. A*, **797**:44–56 (2015).

- J. Walshe *et al.*, Resonant scattering of ^{28}Mg with the Thick Target Inverse Kinematics Technique, submitted to EPJ Web of Conferences. Proceedings of the 21st International Conference on Few-Body Problems in Physics.

- J. Walshe *et al.*, First results from the particle spectroscopy of ^{28}Mg, in preparation.

Contents

List of Figures

List of Tables

Chapter 1

Introduction

Understanding the universe on the nuclear scale presents a rather unique set of challenges. Nuclei lie, in terms of size, between atoms (which have radii of the order of 10^{-10} m) and fundamental particles, which are essentially point-like. In the first case the behaviour of atoms is governed by the electromagnetic force, which is in turn completely described by quantum electrodynamics [2, 3]; the properties of the hydrogen atom can be accurately predicted by calculations [4]. In the latter case the interactions of the 12 elementary quarks and leptons are well described by the Standard Model, with the nature of the strong force given by quantum chromodynamics [5]. In-between these scales, however, lies the nuclear domain (objects with radii of the order of fm where 1 fm = 10^{-15} m), for which no such complete theory exists. There are fewer than 120 known elements but over 3000 known nuclides [6], and any theory of the nucleus must attempt to explain the properties of all of these over the incredibly diverse nuclear landscape: from single- or few-nucleon systems to those with hundreds of nucleons, and from the valley of stability to nuclei with lifetimes of less than 10^{-20} seconds.

1.1 The nucleus

The study of atomic nuclei began with Rutherford's discovery of the nucleus by the scattering of α particles from gold foil [7], followed by the first indications from $(\alpha,{}^3\mathrm{He})$ and (α, p) scattering reactions on nitrogen and oxygen that all nuclei are constructed from

the hydrogen nucleus [8]. The modern picture of the nuclear constituents was completed in 1932 with the discovery of the neutron by Chadwick using (α, n) reactions on a beryllium target [9, 10].

Nuclei, as they are now understood, are compact systems comprised of Z protons (with electric charge $+1e$) and N neutrons (with zero net electric charge) that interact via the *residual strong interaction*, also called the nuclear force. Each having an intrinsic spin quantum number $s = 1/2$, the nucleus is constructed from the $A = Z + N$ nucleons according to the Pauli exclusion principle, with no two protons or neutrons sharing the same quantum numbers, resulting in a wide variety of nuclear properties as a function of Z and N.

The strong interaction is a short-range force that comprises a repulsive and an attractive component, resulting in a minimum of the potential at $r \approx 1.5$ fm, which sets the characteristic length scale for the nucleus. Realistic nucleon-nucleon potentials require tensor as well as radial components, and in systems with $A > 2$ three-body forces are observed. Properties of the nuclear force are described in detail in introductory texts such as Krane [11].

This first approximation of the residual strong interaction leads to the liquid drop model of the nucleus [12], a phenomenological theory which provides a good description of the systematic variation of nuclear properties over the entire mass range. In order to accurately predict the properties of specific nuclei, however, more sophisticated nuclear models are required.

1.2 Clustering at the nuclear scale

Clustering, in nuclear physics, refers to the idea that nucleons are not necessarily distributed homogeneously within a given nucleus, and therefore it may be more effective to model a nucleus as being constructed of a number of smaller nuclei, rather than directly by protons and neutrons. Thorough reviews of the topic can be found in Refs. [13–15],

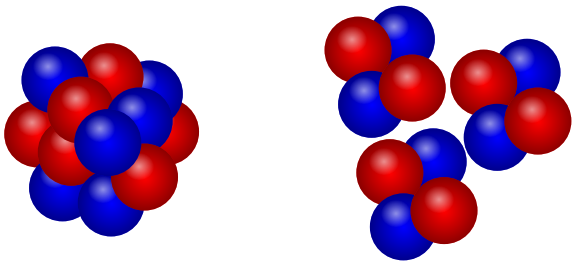

Figure 1.1: Schematic illustration of ^{12}C in (left) non-clustered and (right) clustered states. Protons and neutrons are blue and red circles respectively. Both pictures represent one of many configurations of each kind: the spherical non-clustered nucleus is typically the lowest energy state; the three-centre α-cluster configuration is most famously associated with the Hoyle state (see Ref. [16] and references therein).

but in this section an outline of the evidence supporting such a model is given. Figure 1.1 illustrates the difference between the cluster and single-particle pictures.

1.2.1 The need for a cluster model

The most successful theoretical model of the nucleus to date is the nuclear shell model [17] (a full review of which is given in Ref. [18]), which provides predictions of spins and parities of nuclei by considering the states of individual nucleons under the influence of a *mean-field* potential generated by the sum of the interactions of the other nucleons. The protons and neutrons fill this potential, occupying successively higher energy states as a result of the Pauli exclusion principle, and the properties of a given nucleus are determined by a small number of nucleons at the top of the potential. Excited states of nuclei can then be understood as the movement of nucleons to higher energy levels, and the quantum numbers and degeneracies predicted by the shell model show remarkable agreement with experiments. The shell model is sometimes described as the *independent particle* model, to distinguish it from the cluster picture.

A major triumph of the shell model was the successful prediction of the nuclear *magic numbers*—the particular numbers of protons and neutrons that are observed to form nuclei with particularly high binding. When a large gap between adjacent energy levels appears in the potential, this is said to be a *shell closure* and an unusually large amount

of energy is required to excite nucleons to the next shell. Closed-shell nuclei are more likely to be stable, and those with filled shells in both the neutron and proton potentials are described as *doubly magic*.

This model reproduces experimental results well throughout the entire nuclear mass range and, as such, is widely considered to provide an accurate picture of the structure of the nucleus. Shell-model calculations are, however, most appropriate near closed shells where a single or few valence (or missing) nucleon(s) dominate the nuclear properties; mid-shell nuclei, on the other hand, require coupling of all of the nucleons in the unfilled shell. Even for closed-shell nuclei modifications to the shell-model levels are required. In particular, some excited states of heavy nuclei require a description that considers collective (rather than single-particle) motions, namely vibrations and rotations.

At the other end of the mass scale, the shell model successfully predicts properties of many light nuclei where it may be expected that the mean-field approximation is weaker; even the deuteron can be modelled with some success as a proton and a neutron each in the potential associated with the other nucleon. Figure 1.2 shows a calculation of level energies in ^{12}C using a no-core shell model approach and the CD-Bonn nucleon-nucleon (NN) interaction [19]. The calculated levels are grouped according to the size of the model space in units of $\hbar\Omega = 15$ MeV. While agreement with the experimental levels is good, it is clear that the shell model does not offer a complete description of the behaviour of the ^{12}C nucleus. The 0^+ state at 7.65 MeV—the important Hoyle state, understood to have a 3α cluster structure [16]—is not reproduced at all, suggesting that the mean field approach fails when cluster structure is important.

Recent improvements in computing power have made it possible to model light nuclei by considering all of the $A(A-1)/2$ nucleon-nucleon interactions. The ability to examine wavefunctions of individual nucleons gives new insight into the physical arrangement of nucleons and conditions required for formation of nuclear sub-structures. Some of these methods will be discussed in more detail in Chapter 2.

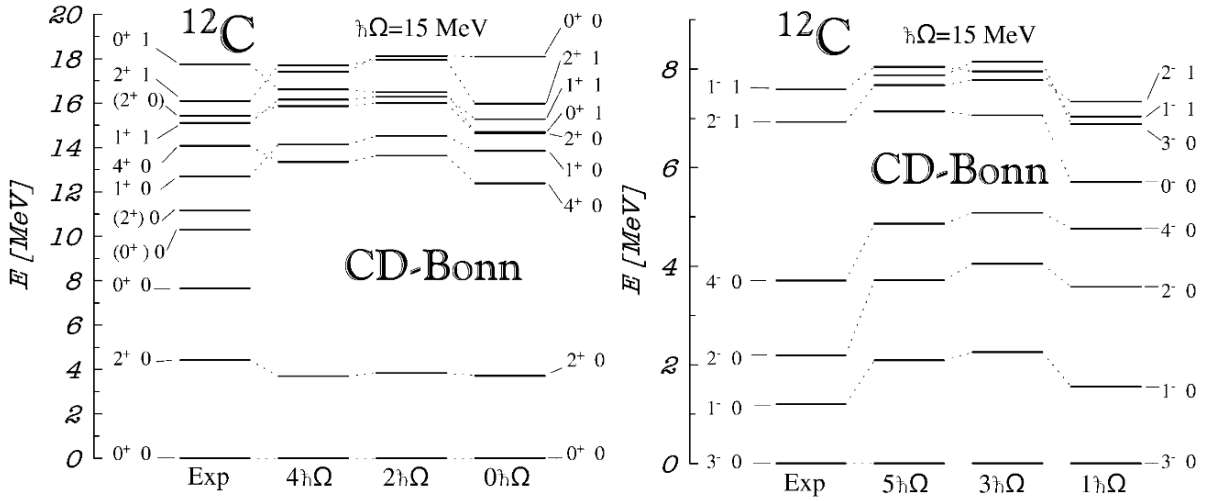

Figure 1.2: Levels in ^{12}C predicted by no-core shell model calculations compared with experimentally measured values, showing (left) positive parity and (right) negative parity states. The levels are grouped by the size of the model space used in the calculation, in units of $\hbar\Omega$. Reproduced from Ref. [20].

1.2.2 Motivation for clustering

One of the most straightforward indications of the presence of clustering is the phenomenon of α decay. An effective model of an α-decaying nucleus is that of an α particle trapped in a potential well, formed by the nuclear force and the Coulomb barrier, where the lifetime of the nucleus is related to the probability of the α particle tunnelling through the barrier. This is a simple cluster model as it contains, implicitly, the assumption that the α particle exists inside the nucleus for some time before the decay occurs.

More generally, nuclei exist because they form energetically favourable states. The mass of a bound nucleus is less than that of its constituents, and so by constructing a nucleus from nucleons energy is released; equivalently, energy must be put in again to take the nucleus apart. By comparing the binding energies of a nucleus and its component nucleons, it can be seen that as energy is added *clusters* of nucleons are formed before the nucleons can be completely separated. Table 1.1 shows a selection of these separation energies, i.e. the energy that must be put into a nucleus in order to separate it into given components. An important feature to note is that the high binding energy of the α particle—in comparison to pairs, triplets or quintets of nucleons—makes it a common

Table 1.1: Selected light nuclei and separation energies for given structures. Because of the binding energy of cluster components, clusters form before the disassociation energy for individual nucleons is reached. From the 2003 Atomic Mass Evaluation [21, 22].

Nuclide	Structure	Separation energy (MeV)
α	$t + p$	19.814
	^{3}He+n	20.578
	$2p + 2n$	28.296
^{12}C	3α	7.275
	$6p + 6n$	89.096
^{16}O	^{12}C+α	7.162
	4α	14.437
^{20}Ne	^{16}O+α	4.730
	^{12}C+2α	11.892
	5α	19.167

cluster component of larger nuclei.

The concept of nuclear cluster structures being linked to excitation energy is most famously illustrated in the Ikeda diagram (Fig. 1.3), which shows the separation energies for various cluster structures in a selection of light even-even $N = Z$ nuclei, described as α-conjugate because they can be thought of as being composed of only α particles. This energetics argument suggests that cluster structures would appear close to the corresponding decay thresholds. Note that the separation energy only takes into account the relative binding of a nucleus and its cluster components, and so for nuclei consisting of three or more clusters there are a number of different possible geometric arrangements which may have different energy requirements.

1.2.3 Tests of clustering

The cluster structures predicted in the Ikeda diagram have a number of properties that can be measured to test the validity of the cluster picture. Departure from a spherical shape changes the moment-of-inertia of the nucleus, which can be deduced from the energy dependence of rotations of a given structure. If the charge distribution is non-spherical, then an electric quadrupole moment will be introduced that can also be measured. It is

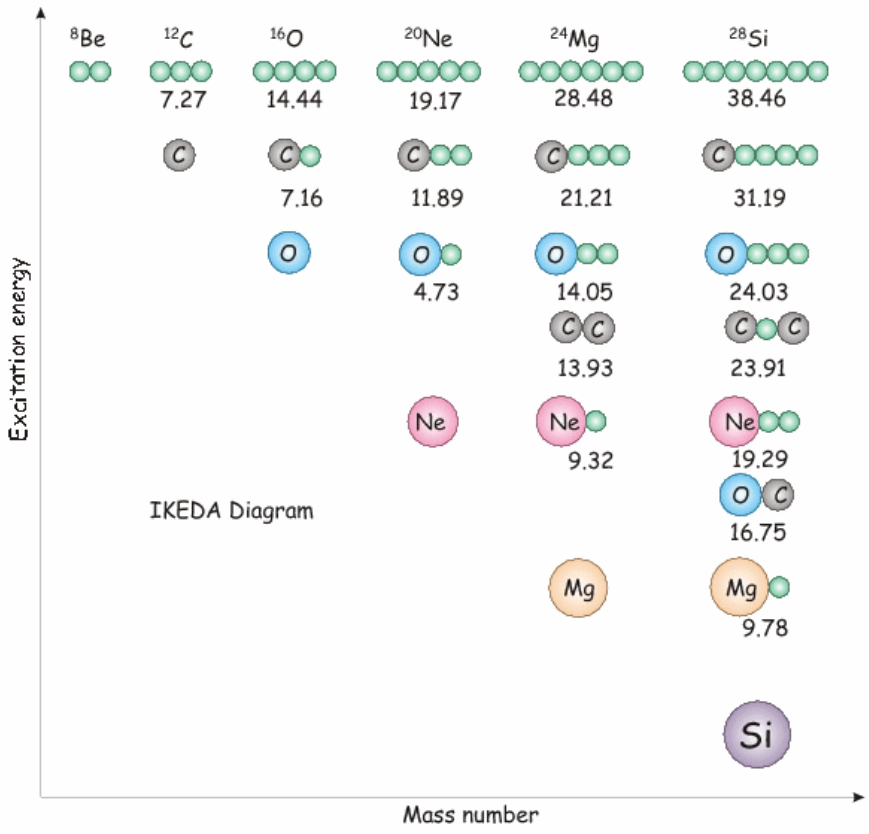

Figure 1.3: The Ikeda diagram, which links cluster structures to excitation energy of the nucleus, for selected α-conjugate light nuclei. Separation energies for each structure are given in MeV; green circles denote α particles. From Ref. [23] and published in Ref. [14], modified from [24].

also reasonable to expect that a clustered nucleus may preferentially decay by emitting a cluster when compared to other decay channels; this can be quantified by both branching ratios and decay widths.

Experimental evidence of clustering will be discussed in more detail in Chapter 2 alongside theoretical models and the predictions that they make.

1.3 This work

This thesis presents the results and analysis of an experiment that was performed with the aim of investigating clustering phenomena in ^{28}Mg. Chapter 2 discusses the motivation for this experiment in the context of current theoretical models of clustering, while Chapter 3.3 describes the experimental technique used. The remainder of the thesis concerns the analysis of the resulting data and presents the results thereof.

Chapter 2

Theory

In this section theoretical models of the nucleus will be discussed quantitatively, including in particular evidence for clustering phenomena in light nuclei, as well as the theoretical framework used to interpret experimental data.

2.1 Early models of clustering

Simple cluster models often start from the assumption that a nucleus is clustered, and then compare the results of this model to experiments in order to determine how good this assumption is. In order to construct a cluster model of this sort, a sensible cluster structure must be chosen. Good cluster candidates are nuclei that are strongly bound and inert, so that when energy is put into the nucleus as much as possible is used to separate the clusters, and not to excite them or break them apart.

Figure 2.1 shows the binding energy of a variety of light nuclei. The right-hand panel plots this against the energy of the first excited state of each nucleus, and it can be seen that not only is the α particle relatively strongly bound, it requires at least 20 MeV to populate an excited state, which is very similar to the single-nucleon separation energy (see table 1.1). In other words, as all excited states are unbound to particle decay, any excitation of the α particle will result in break-up on a very short time scale (10^{-21} s for the first excited state). Therefore in the case of a larger nucleus that is comprised of α

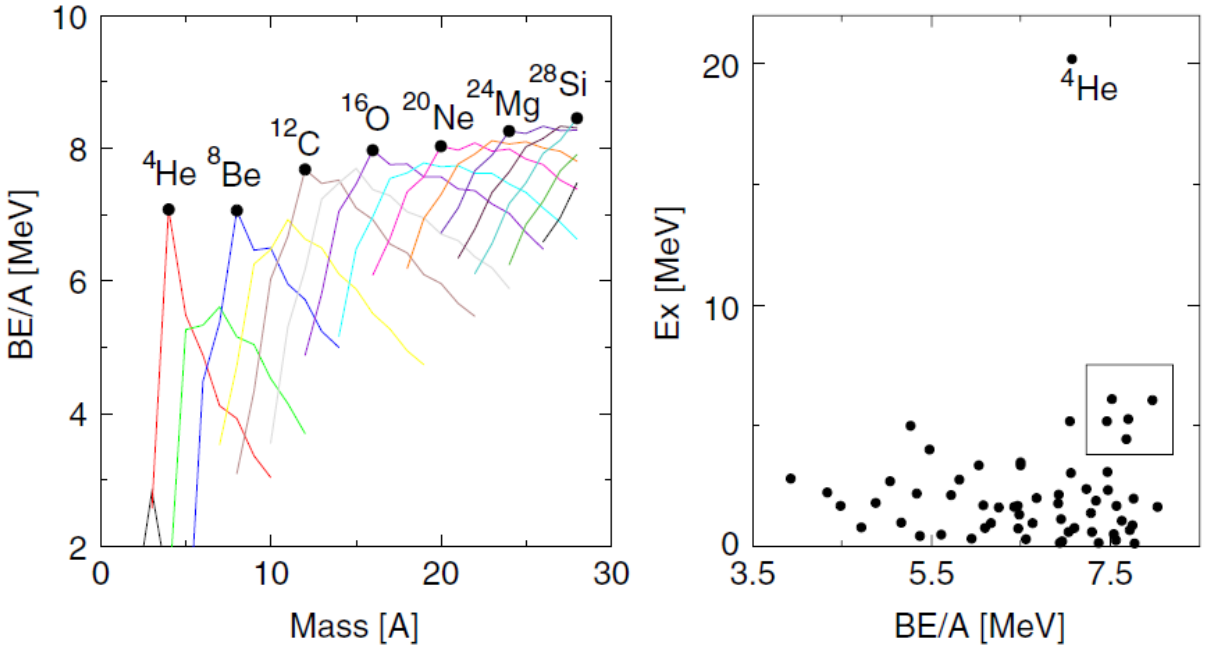

Figure 2.1: (left) Binding energy per nucleon for light nuclear systems up to $A = 28$. Isotopes of the same element are connected by lines, with α-conjugate nuclei marked. (right) Binding energy per nucleon for nuclei up to $A = 20$ plotted against the excitation energy of the first excited state. The nuclei highlighted by the box are ^{12}C, ^{14}O, ^{14}C, ^{15}N and ^{16}O. Reproduced from Ref. [13].

particles, if insufficient energy is available for the α particles to be broken up, the nucleus must undergo some other mode of excitation such as separation into clusters. Alpha particles, therefore, make excellent clusters, and other good cluster candidate nuclei are marked in Fig. 2.1 with a box.

2.1.1 Alpha-conjugate nuclei

The left panel of Fig. 2.1 shows the binding energy of light nuclei as a function of mass number, with lines connecting isotopes. Alpha-conjugate nuclei that can be split into only α particles are marked, and clearly there is some advantage in binding energy for light nuclei of this form: whole α particles provide more binding per nucleon on average than individual or paired nucleons. Figure 2.2a shows how α particles may be arranged within α-conjugate nuclei in order to create the most stable structure, which is done by maximising the number of nearest-neighbour bonds. For example, three α particles can

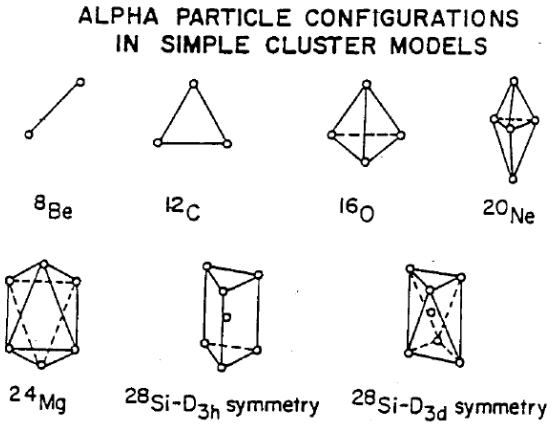

(a) Geometric arrangements of α particles in light α-conjugate nuclei that maximise the number of nearest-neighbour bonds. Reproduced from Ref. [25].

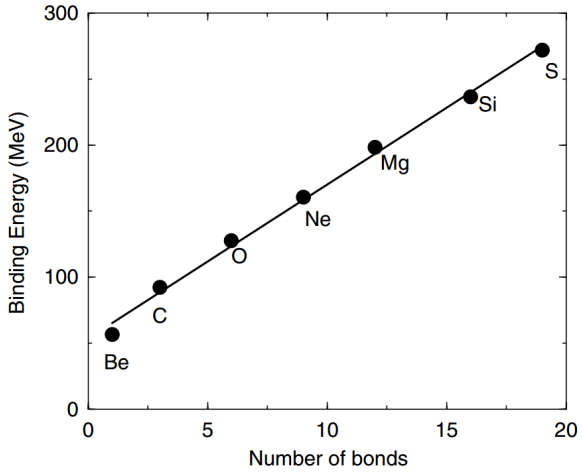

(b) Binding energy of light α-conjugate nuclei as a function of the number of α-α bonds. Reproduced from Ref. [13].

Figure 2.2: Binding energy of α-conjugate nuclei.

be used to construct ^{12}C; if they are arranged in a line then there are two short range nuclear bonds between the centre α particle and each of the other two. In a triangular structure, on the other hand, there are three bonds - the α particles that were at the ends of the linear structure are now close enough to be bound to each other. The triangle, therefore, is expected to be more strongly bound than the chain arrangement.

Figure 2.2b shows that there is a linear relationship between the number of bonds in each of these most stable structures and the measured binding energy of α-conjugate nuclei, and therefore the former is a good predictor of the latter. While other approaches (such as the liquid drop model) can also predict the binding energies of these nuclei, the simplicity with which this is done within the α cluster picture is very appealing. Importantly, if the nucleons act independently and if the nucleon-nucleon interaction extends throughout the nucleus, then the number of nucleon-nucleon interactions is $A(A-1)/2$ and so the binding energy would vary quadratically with A rather than linearly.

2.1.2 Alpha-plus-core model

In Chapter 1, α decay was cited as an early motivator of the cluster picture, and indeed the model of an α particle in a potential generated by the remainder of the nucleus -

called here the core - leads to another simple description of clustering. By considering the interaction between the α particle and the core, the cluster picture is extended to clusters of non-α type. A number of predictions can be made including, importantly, finding the spacing of energy levels by solving the Schrödinger equation for the α particle in the core potential.

Neon-20 is a natural starting point for the α-plus-core model. The stability of the α particle comes from its doubly magic nature, with two protons and two neutrons filling their respective potentials to the first magic number. The second magic number is eight, and so the second doubly magic nucleus is ^{16}O with $Z = N = 8$. Like the α particle, ^{16}O has high binding energy per nucleon (8.0 MeV/A) and a high lying first excited state (6.0 MeV), which make it a very good cluster candidate. A natural place to look for clustering is, therefore, the ^{16}O+α system, ^{20}Ne, and indeed much experimental evidence exists of rotational bands with large reduced widths for α decay [26]. Figure 2.3 shows energy levels in ^{20}Ne calculated using an explicit cluster model in which the Schrödinger equation is solved for an α particle in a central potential. The potential itself is found by the convolution of a nucleon-nucleon potential with the densities of the cluster and core.

The agreement between theory and experiment for such a simple model is excellent, suggesting that the cluster model is a realistic one, and two states not predicted in this energy range (7^- and 9^-, dashed lines in Fig. 2.3) are interpreted as representing the mixing of other structures with the clusters. The same success was found for ^{44}Ti (^{40}Ca+α) [27], and recent experimental evidence has been found for α+^{208}Pb structures in ^{212}Po [28], both of which are also nuclei of the form α particle plus doubly-magic core.

2.1.3 More complex cluster structures

A natural extension of the models described above is to look for multi-centre cluster structures that allow the inclusion of different cluster species, and indeed many such structures are expected in the Ikeda picture. Marsh and Rae [29] investigated the structure of ^{24}Mg with an α-cluster model by allowing the positions of the six α particles to vary freely and

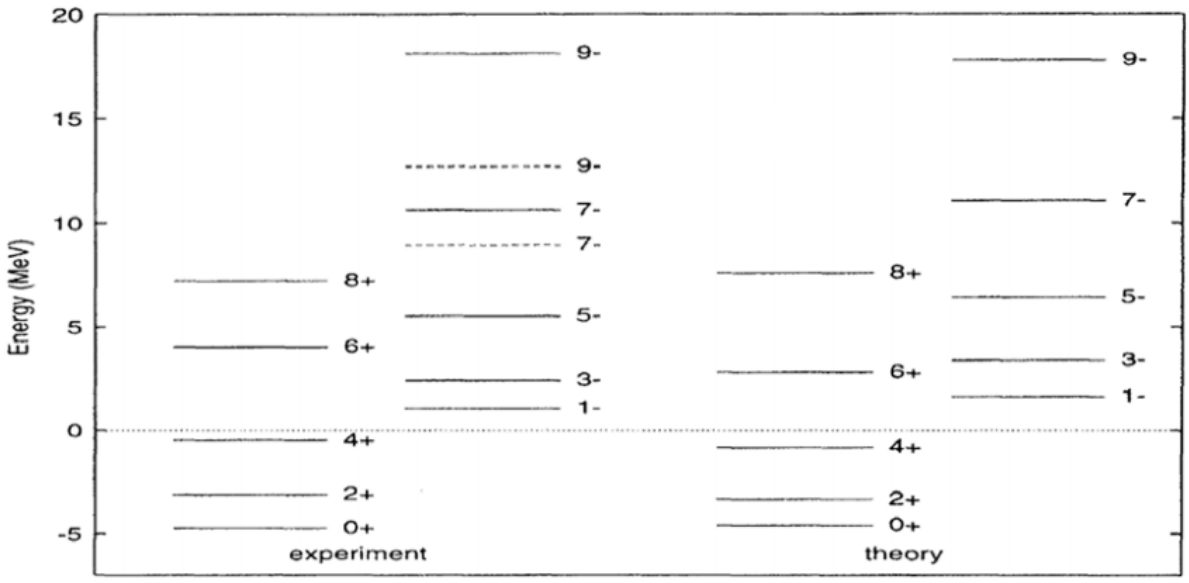

Figure 2.3: Comparison of energy levels in ^{20}Ne (left) experimentally measured and (right) calculated using an α+^{16}O cluster model. Excitation energy is given relative to the threshold for α decay, where $S_\alpha = 4.7$ MeV (dotted line at $E = 0$ MeV). Reproduced from Ref. [27].

calculating the potential energy of each configuration. A number of different structures were found, each associated with a local minimum in the potential energy surface, ranging from a compact spherical shape to an exotic linear 'chain' state. Of particular interest, however, is the intermediate structure consisting of a compact tetrahedron of four α particles, with the remaining two on either side of the core, i.e. α+^{16}O+α. A number of calculated properties of this state, such as α particle decay strength and moment-of-inertia were noted to correspond to the properties of states measured in ^{12}C+^{12}C scattering reactions.

2.2 *Ab initio* methods

The cluster models described so far all start by assuming a cluster structure and calculating the observable properties that such a nucleus would have. The accuracy of the predicted properties does indicate the validity of the clustering assumption, but a true test of the phenomenon is model independence. Nuclear models that describe the nucleus

using only the nucleon-nucleon interaction - without further simplifying assumptions - are described as *ab initio*, that is, from first principles. Such models, and their application to the concepts of clustering, are described in this section.

2.2.1 Anti-symmetrised Molecular Dynamics

As nucleons are fermions, they follow the Pauli exclusion principle: no two nucleons may have the same quantum numbers. This can be achieved mathematically by ensuring that the total system wavefunction is antisymmetric with respect to the exchange of any two nucleons. For a system of two particles a and b, that can be in states α or β, the total wavefunction is

$$\psi(a,b) = \frac{1}{\sqrt{2}}\left[\phi_\alpha(a)\phi_\beta(b) - \phi_\alpha(b)\phi_\beta(a)\right] \tag{2.1}$$

so that if a and b are both in the same state α or β, then $\psi = 0$. In the anti-symmetrised molecular dynamics (AMD) framework, this property is achieved by constructing the general wavefunction for a system of A nucleons, $|\Phi\rangle$, from a Slater determinant of the individual nucleon wavefunctions, φ_i:

$$|\Phi\rangle = \frac{1}{\sqrt{A!}}\mathcal{A}\left(\varphi_1, \varphi_2, \ldots, \varphi_A\right) = \frac{1}{\sqrt{A!}}\begin{vmatrix} \varphi_1(1) & \varphi_2(1) & \ldots & \varphi_A(1) \\ \varphi_1(2) & \varphi_2(2) & \ldots & \varphi_A(2) \\ \vdots & \vdots & \ddots & \vdots \\ \varphi_1(A) & \varphi_2(A) & \ldots & \varphi_A(A) \end{vmatrix}. \tag{2.2}$$

Full reviews of AMD are available in [30, 31], but the important characteristics of this method are presented here. The wavefunctions of individual nucleons are typically represented by a Gaussian shape, with the amplitude at $\vec{r}$ given by

$$\varphi_i(\vec{r}) = e^{-\nu(\vec{r}-Z_i)^2}\chi_i\eta_i, \tag{2.3}$$

where ν is a width parameter that is fixed for all nucleons, η_i is the isospin parameter (proton or neutron), and Z_i is the location of the wave packet. The spin parameter χ_i is

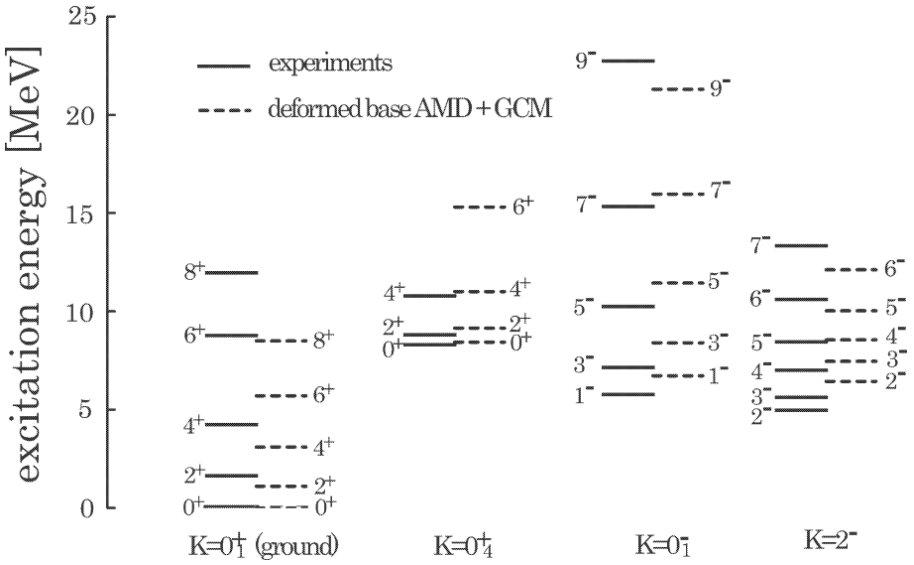

Figure 2.4: Energy levels in ^{20}Ne for both experiment (solid lines) and AMD calculations (dashed lines). The $K = 0$ bands have α+^{16}O structure, while the $K = 2$ band is shell model like. Reproduced from Ref. [31].

written as

$$\chi_i = \left(\frac{1}{2} + \xi_i\right)\chi_\uparrow + \left(\frac{1}{2} - \xi_i\right)\chi_\downarrow \tag{2.4}$$

so that ξ_i selects between spin up and spin down. The total energy of the system is then minimised by varying Z_i and ξ_i for each nucleon under the influence of an appropriate nuclear potential.

The power of the AMD framework is its ability to successfully describe both cluster-like and shell model-like nuclei which is due to the freely varying locations of the nucleons, Z_i. If all of the nucleons share a common location then the problem resembles the harmonic oscillator approach; if they do not, a cluster nucleus is described. The ability to examine individual wavefunctions - and therefore nucleon density distributions - in addition to experimentally observed properties allows structures to be directly associated with measured levels. An excellent test case for AMD calculations is ^{20}Ne, as described in Section 2.1.2. Figure 2.4 shows energy levels in ^{20}Ne calculated using AMD, and the associated density distributions are shown in Fig. 2.5. As expected, prominent α+^{16}O cluster structure is found, although importantly the same calculations also reproduce the shell-model structure of the $K^\pi = 2^-$ band. The appearance of clustering in calculations

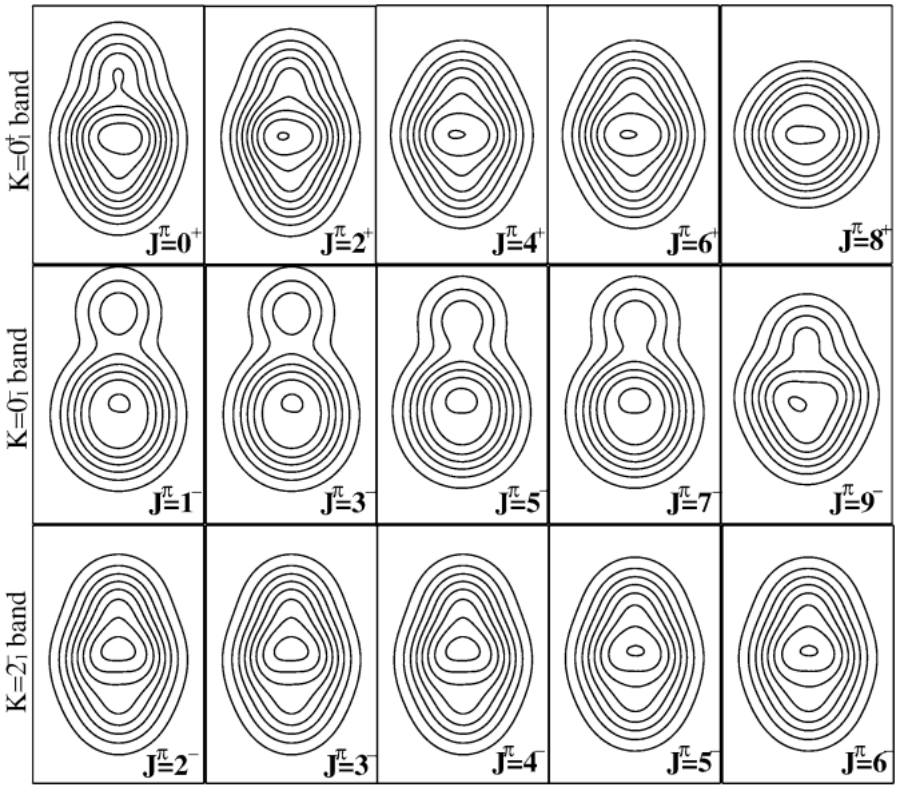

Figure 2.5: Density distributions for levels in ^{20}Ne calculated using AMD. See Fig. 2.4 for level structure. Reproduced from Ref. [31].

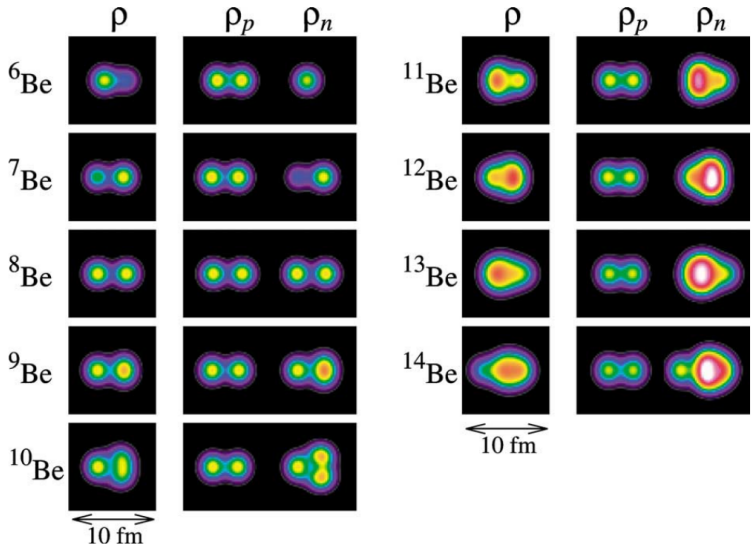

Figure 2.6: Density distributions of the ground states of the Be isotopes calculated using AMD, shown for total (ρ), and protons (ρ_p) and neutrons (ρ_n) separately. Reproduced from Ref. [31].

where no assumption of cluster structure is made is a key result that strongly supports the cluster picture.

2.3 Nuclear molecules

Amongst the generally well-bound α-conjugate nuclei described in Section 2.1.1, ^{8}Be is somewhat of an anomaly. It is the only unstable α-conjugate nucleus lighter than ^{40}Ca, being unbound in its ground state to α decay by 92 keV. Even more curiously, ^{9}Be is stable and ^{10}Be is long lived ($T_{1/2} = 1.4 \times 10^{6}$ years): neutrons, apparently, play some role in binding the α particles to each other. In fact, one must look as far as ^{13}Be to find the point at which adding neutrons results in a nucleus with a shorter half-life than ^{8}Be, and in the other direction ^{7}Be has a half-life of 53 days suggesting that even the addition of a neutron hole provides binding to the $Z = 4$ system.

Figure 2.6 shows density distributions for the ground states of $^{6-14}$Be calculated using AMD. The proton densities show clear cluster structure for all isotopes, and for $A \geq 8$ this is also seen in the neutron densities.

The nuclear shell model finds success by applying the concepts of atomic physics to

the nuclear domain. In atoms, the electron orbitals are the result of light particles moving under the influence of a central potential generated by a heavy core; the energy levels of this potential are then filled according to the Pauli exclusion principle. The successful application of these ideas to the nucleus may fairly be considered as quite surprising as the mean-field assumption of nucleons moving in a central potential does not seem to be as strong as in the atomic case.

In parallel to the atomic analogy of the shell model, the cluster model can be compared to the physics of atoms bound within molecules. In this picture the nuclear system is made up of a multi-centre structure, with each separate core constructed directly of nucleons before the nucleus is constructed from these cores; the heavy cores are then bound together by the action of light valence particles. Most applicable to the nucleus is covalent bonding, where binding is provided by exchange of electrons between atoms. Nuclei modelled in this way are described as *nuclear molecules*; the case of the beryllium isotopes provides some motivation for applying these ideas to the nucleus with α particles taking the role of the heavy cores and neutrons that of the light exchange particles that bind the cores together.

In this *molecular-orbitals* formalism, there are two types of bonds: σ bonds, in which the bond axis is the same as the symmetry axis of the electron orbitals, and π bonds, where the bond axis is perpendicular to the symmetry axis. These orbitals are shown schematically in Fig. 2.7.

Examination of AMD calculations reveals that neutrons occupying σ orbitals are associated with enhanced clustering [31]. Figure 2.8 shows that as the number of neutrons in σ orbitals increases, so does the deformation of the nucleus and thus the α-α core separation. This results partly because the presence of neutron probability density between the cores prevents them from approaching due to the Pauli exclusion principle. Also, the increase in core separation reduces the kinetic energy of the neutrons in the σ orbitals, resulting in a more energetically favourable state.

While the evidence for the role played by valence neutrons in Be isotopes is now quite

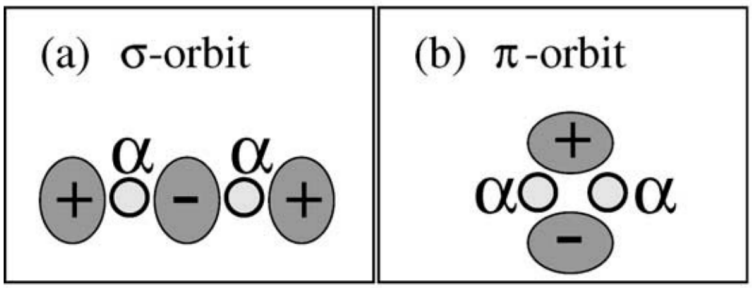

Figure 2.7: Comparison of (a) σ and (b) π orbitals in neutron rich Be isotopes. The locations of the α cores are marked, and the areas where the neutron wavefunctions are positive or negative—i.e. where the probability density is large—are shown schematically. For σ orbitals, the neutron probability density is localised on the axis joining the α cores; for π orbitals the probability density is localised in the plane normal to this axis. Reproduced from Ref. [31].

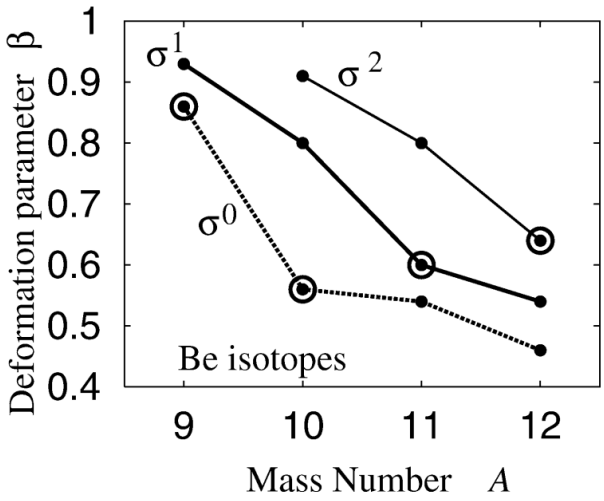

Figure 2.8: AMD calculations of the deformation of Be isotopes as a function of mass number. Lines connect states with the same number of neutrons in σ orbitals: zero (σ^0, dotted line), one (σ^1, thick solid line) and two (σ^2, thin solid line). The ground states of each isotope are indicated by circles. [31]

strong, the open question that remains is how complex these nuclear molecular structures can become. Again the Ne isotopes are of interest because of the pronounced cluster structure that exists in ^{20}Ne, and so the neutron rich isotopes may be examined in order to investigate the effect of valence neutrons on the ^{16}O+α system.

The existing level data for ^{21}Ne was examined by von Oertzen [32] who identified two parity doublet bands with the molecular picture, while the remaining bands were associated with the shell-model-like quadrupole deformed structure. The structure of ^{22}Ne was examined by Rogachev *et al.* [33] by the resonant scattering of ^{18}O on α particles, and a rotational band was observed with the unusual property of having two negative parity states for each J value. This was interpreted as being due to the exchange of the two valence neutrons between the ^{16}O and α cores, resulting in the mixing of the ^{18}O+α and ^{16}O+^{6}He structures. More recent AMD calculations have suggested the existence of both the ^{18}O+α molecular bands and separately the ^{16}O+2n+α molecular orbital bands [34], although the former were associated with the observed states of Ref. [33] and the latter were present at lower excitation energies.

While the picture of molecular orbitals in neutron-rich Ne isotopes is not yet complete, it seems likely that structures such as this are present in some way. For this reason, von Oertzen suggests that the next logical place to look for nuclear molecular structure is in the Mg isotopes, where the symmetric α+$x n$+^{16}O+$x n$+α structure may exist. The study of ^{24}Mg in Ref. [29] (see Section 2.1.3) provides evidence for the $N = Z$ case, i.e. without valence neutrons, and in the neutron-rich isotopes the action of valence neutrons may again give rise to molecular structures. Von Oertzen calls the proposed α+2n+^{16}O+2n+α structure of ^{28}Mg *nuclear water* in analogy to the atomic structure of H_2O. These structures are more complex than any observed so far, so experimental evidence of their existence or absence would be of great interest in the study of nuclear molecules.

The threshold energy for this molecular structure in ^{28}Mg is at 47 MeV. Characterising the nuclear structure at such a high energy will be challenging, but at lower energies the

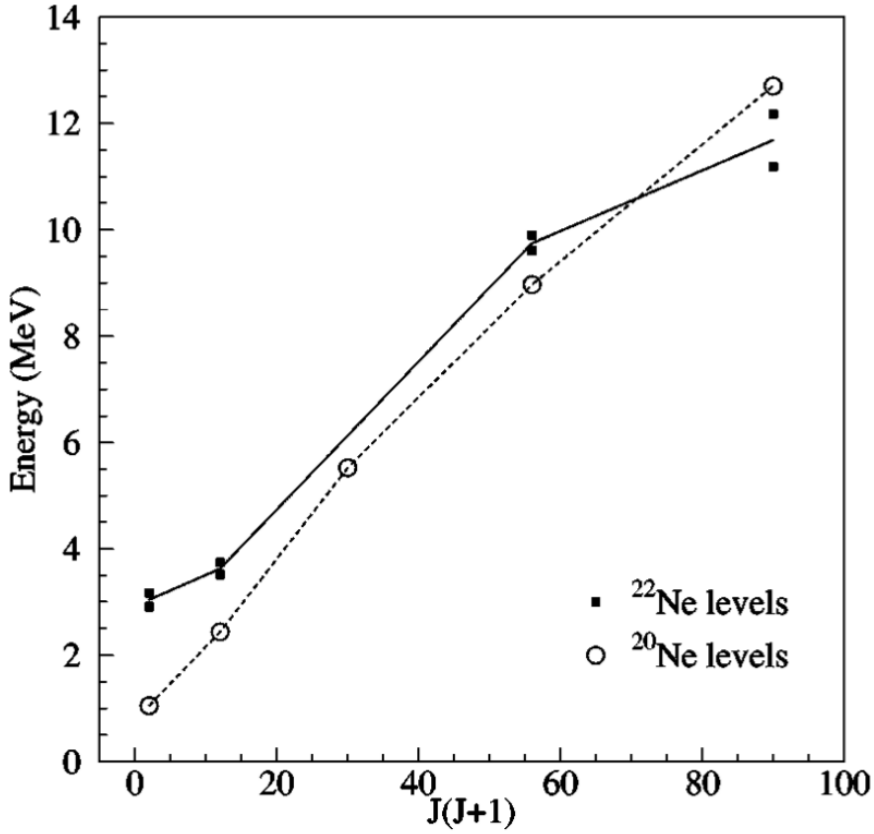

Figure 2.9: Negative parity rotational bands in ^{20}Ne and ^{22}Ne. In the latter case, pairs of levels are observed for each J value, interpreted as due to the exchange of the two valence neutrons between the α and ^{16}O cores. Figure from Ref. [33], data for ^{20}Ne from Ref. [26].

presence of structures such as ^{22}Ne+2n+α or ^{24}Ne+α would be strong indicators that this structure is possible.

2.4 *R*-Matrix Theory

The theoretical models described above all share the same method for comparison to experimental results: the calculation of observable parameters, namely energy levels E_R and their decay widths Γ and spin-parity J^π. These quantities are all secondary observables, in that they must be deduced in some way from the primary observable: the scattering cross section as a function of energy and angle, $\sigma(E, \theta)$. A powerful theoretical framework for the analysis of cross section data is R-matrix theory. First described by Wigner and Eisenbud [35], it was popularised by Lane and Thomas [36], though complete R-matrix analyses have only been made possible in recent years by the increase in accessible computing power and the resulting availability of specialised codes for the calculation of cross sections and fitting of resonance parameters. Recent reviews of the topic, such as that of Thompson and Nunes [37], discuss R-matrix methods in detail with reference to modern computerised analysis methods.

In R-matrix theory reactions are assumed to proceed through the compound nucleus, which is then split into internal and external regions, meeting at a radius $r = R_m$ from the origin. In the internal region, the potential is comprised of both Coulomb and nuclear parts, while in the external region the nuclear component is zero. A solution is found, therefore, by matching the internal and external wavefunctions at R_m. The particle pairs through which the compound nucleus is created or decays are called the reaction channels c.

The R-matrix for scattering from an incoming channel c to an outgoing channel c' is defined as

$$\mathbf{R}_{cc'} = \sum_{p=1}^{N_p} \frac{\gamma_{pc}\gamma_{pc'}}{\epsilon_p - E} \tag{2.5}$$

which has N_p poles at energies $E = \epsilon_p$. The reduced width amplitudes, γ_{pc}, are defined

for each channel c and pole p by

$$\gamma_{pc} = \sqrt{\frac{\hbar^2}{2\mu_c R_m}} u_{pc}(R_m) \tag{2.6}$$

for the channel reduced mass μ_c and the R-matrix basis wavefunctions u_{pc}. The reduced widths, γ_{pc}^2, and the pole energies, ϵ_p, are related to but distinct from the measured decay widths Γ_{pc} and resonance energies E_R. Most notably, the former depend on the value chosen for the matching radius, while the latter should not. In order to calculate the scattering cross section first the penetrability, P, and the shift function, S, are defined as

$$P = \frac{kR_m}{F^2 + G^2} \tag{2.7}$$

and

$$S(E) = kR_m \frac{\dot{F}F + \dot{G}G}{F^2 + G^2} \tag{2.8}$$

for the regular and irregular Coulomb functions $F_L(\eta, kr)$ and $G_L(\eta, kr)$ evaluated at $r = R_m$, and the wave number k. The derivative of F with respect to kr is denoted by $\dot{F}$. The Coulomb functions are defined in detail in Ref. [38]. The penetrability relates the widths by

$$\Gamma_{pc} = 2P\gamma_{pc}^2, \tag{2.9}$$

and the shift function relates the energies as

$$E_R = \epsilon_{pc} - \gamma_{pc}^2(S(E) - R_m\beta) \tag{2.10}$$

where β is a free parameter. The scattering matrix $\mathbf{S}$ is calculated from the R-matrix using

$$\mathbf{S} = \frac{1 - \mathbf{R}(S - iP - R_m\beta)}{1 - \mathbf{R}(S + iP - R_m\beta)} e^{2i\phi} \tag{2.11}$$

where ϕ is the hard-sphere phase shift given by

$$\phi = -\arctan\frac{F}{G}. \tag{2.12}$$

Finally, the differential cross section is calculated from the **S**-matrix. In the most general form this requires proper coupling of the angular momenta and spins in the incoming and outgoing channels as detailed in Ref. [37]. In the spin zero case, however, this simplifies to the absolute value of a sum of all partial waves with angular momentum ℓ and a Coulomb term as

$$\frac{\mathrm{d}\sigma}{\mathrm{d}\Omega} = \left| -\frac{\eta}{2k\sin^2\theta/2}\exp\left[-i\eta\ln\left(\sin^2\theta/2\right)+2i\sigma_0(\eta)\right] + \frac{1}{2ik}\sum_{\ell=0}^{\infty}(2\ell+1)P_\ell(\cos\theta)e^{2i\sigma_\ell(\eta)}(\mathbf{S}-1)\right|^2 \tag{2.13}$$

where P_ℓ denotes the Legendre polynomial of order ℓ, and σ_ℓ is the Coulomb phase shift, given by

$$\sigma_\ell = \arg\Gamma\left(1+\ell+i\eta\right) \tag{2.14}$$

and η is the Sommerfeld parameter defined as

$$\eta = \frac{Z_1 Z_2 e^2 \mu}{\hbar^2 k}. \tag{2.15}$$

The first term in equation 2.13 gives the contribution to the cross section of Rutherford scattering. Despite the inclusion of unphysical parameters such as the matching radius, R_m and the free parameter β, observables such as the resonance energies and widths should be independent of the values chosen. For this reason, Brune [39] developed an alternative parametrisation of R-matrix theory that allows **R** to be calculated directly from the E_R and Γ. In this thesis both the measured and reduced widths will be used; in Ref. [39] a method of converting from one set of parameters to the other is given.

Chapter 3

Experiment

The data for this work were taken in July 2011 at the Grand Accélérateur National d'Ions Lourds (GANIL) cyclotron facility in Caen, France [40]. Magnesium-24 and 28 have been studied using the elastic scattering of α particles. This chapter outlines the experimental conditions.

3.1 Previous work

While the particle spectroscopy of ^{24}Mg is well reported in compilations such as Ref. [41], this is not the case for ^{28}Mg. The latter was first discovered in 1953 by Sheline and Johnson [42, 43] using the ^{30}Si$(\gamma, 2p)$ and ^{26}Mg$(\alpha, 2p)$ reactions. Further works have characterised the bound states up to 8.4 MeV in excitation energy using either ^{26}Mg(t, p) [44–47] or the β-decay of ^{28}Na [48–50]. Prior to this experiment nothing was known about ^{28}Mg above the particle decay threshold which lies at 8.5 MeV for single neutron decay.

3.2 Accelerator facility

The GANIL facility (Fig. 3.1) uses two coupled cyclotrons to accelerate stable beams up to ^{238}U with typical energies of a few to hundreds of MeV per nucleon [51]. The ion source is an Electron Cyclotron Resonance (ECR) source, and a third smaller cyclotron is used

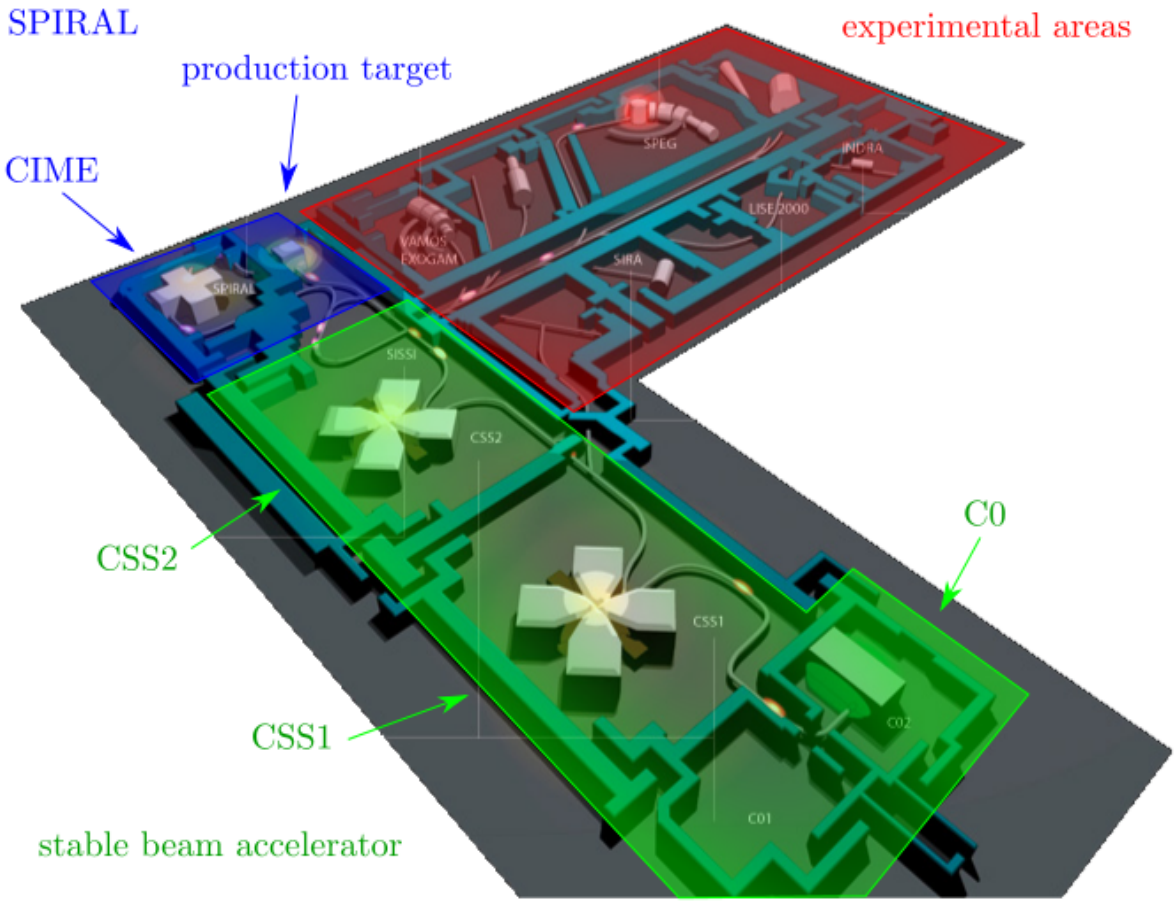

Figure 3.1: The layout of the accelerator facility at GANIL. Modified from Ref. [52]. C0 labels the ion source and injection cyclotron, while the CSS1 and CSS2 provide the bulk of the acceleration for stable beams. SPIRAL is labelled, including the ISOL target, ion source, and cyclotron. See text for details.

to inject the beam into the main part of the accelerator.

3.2.1 Ion source

The ECR ion source at GANIL uses microwaves to ionise the atoms of the source material, which are then electrostatically injected into the first cyclotron. Firstly, the material that will form the beam is vaporised, if required, before entering the ion source. A series of coils are used to create a magnetic trap that contains the gas, and microwaves are injected into the gas with the resonant frequency of the electrons, ω_e, given by

$$\omega_e = \frac{e}{m_e} B \tag{3.1}$$

where e and m_e are the charge and mass of an electron, and B is the magnetic field strength of the trap. This resonant heating creates a plasma where the free electrons are directly heated by the microwaves, and the remaining atoms are ionised by collisions with the electrons.

When the plasma is sufficiently ionised positive ions can be extracted from the trap electrostatically, and injected into the first part of the accelerator.

3.2.2 Cyclotrons

Cyclotrons accelerate ion beams using a constant magnetic field and an oscillating electric field. If a particle with charge q, mass m, and velocity v is placed in a magnetic field with strength B, it will experience a force, F, perpendicular to its velocity given by

$$\vec{F} = q\left(\vec{v} \times \vec{B}\right), \tag{3.2}$$

resulting in circular motion. The radius of the circle, r, is related to the force and the velocity by

$$F = \frac{mv^2}{r}, \tag{3.3}$$

and by equating these expressions it can be shown that the angular frequency of the motion is given by

$$\omega = \frac{q}{m}B \tag{3.4}$$

which is independent of the energy of the particle. In a cyclotron, ions are injected into the centre and as they gain energy the radius of the path that they follow increases, resulting in a spiral; the constant frequency of the motion means that the acceleration can be performed at the same point on each revolution. As the acceleration occurs twice per revolution, the ions are released into the cyclotron in bunches so that they are in phase with the accelerating voltage.

The acceleration is provided by an oscillating electric field that has the same frequency

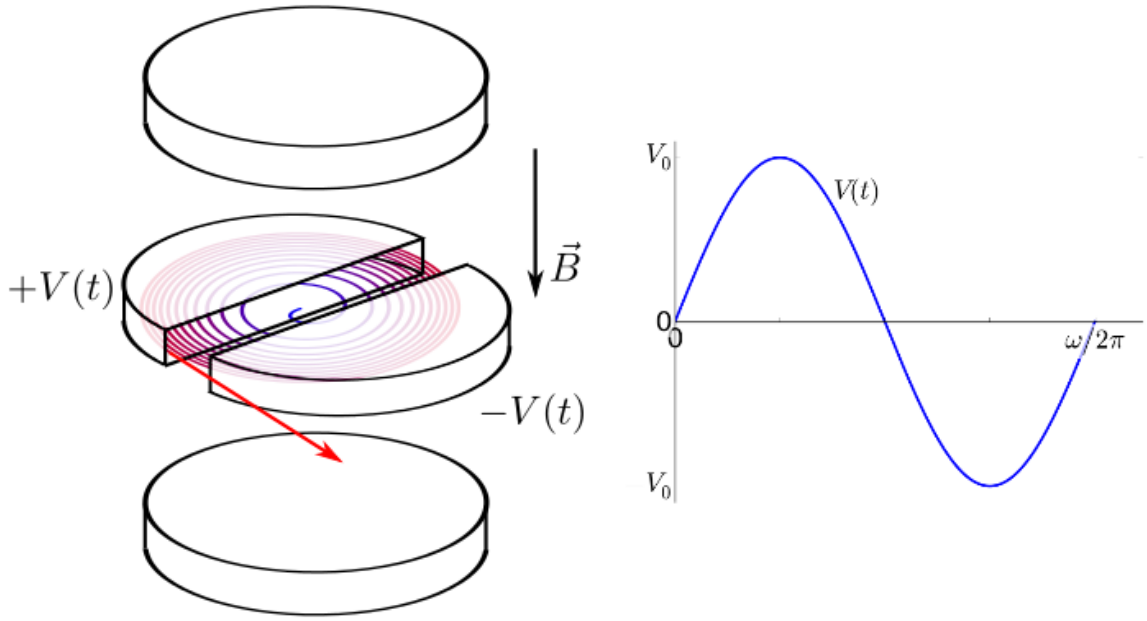

Figure 3.2: Exploded view of the operation of a cyclotron. The D-shaped enclosures have opposite alternating voltages which provide the acceleration, and the magnets above and below the cavity generate a magnetic field that causes the beam to follow a spiral path as it accelerates. See text for details.

as the motion of the particles in the magnetic field. Opposite polarity voltages are applied to D-shaped metal enclosures (shown in Fig. 3.2) through which the beam travels. When the beam emerges from one D it is accelerated by the electric field towards the other D; while inside the D there is no net electric field and so the beam follows a circular path under the influence of the magnetic field as the voltages on each D change. When the beam travels back to the first D the voltages have reversed and thus the electric field is in the opposite direction, causing the beam to accelerate again. All bunches of particles pass between the Ds at the same time and so are all accelerated in phase. When the beam reaches the edge of the cyclotron it is extracted.

The energy of the extracted beam, E, depends on the radius of extraction, R, and the magnetic field as

$$E = \frac{q^2 B^2 R^2}{2m} \tag{3.5}$$

which importantly does not depend on the accelerating voltage. The beam energy is limited by the field strength (which is in turn limited by the current flowing through

the coils) and the size of the cyclotron. In order to reach higher energies in a more cost effective way, the GANIL facility uses a series of three coupled cyclotrons. Between each acceleration stage the beam is stripped of electrons, and as the number of electrons removed by a stripper foil increases with energy, the charge state of the beam can be increased after each cyclotron, and therefore the next accelerator can provide a higher energy.

For a nucleus with charge $q = Ze$, where e is the electric charge, and mass $m = Am_n$, where m_n is the mass of a nucleon, the accelerating power of a cyclotron is characterised by the K number, given by

$$K = \frac{AE}{Z^2} = \frac{e^2 B^2 R^2}{2m_n}. \tag{3.6}$$

By convention K is quoted in units of MeV; the two main cyclotrons at GANIL have $K = 400$, and the injector cyclotron has $K = 25$.

3.2.3 Radioactive beams

Radioactive beams are produced at GANIL using the Système de Production d'Ions Radioactifs en Ligne (On-Line Radioactive Ion Production System, SPIRAL [53]) which employs the technique of Isotopic Separation On-Line (ISOL). A carefully chosen primary beam (in this case ^{26}Mg at 82 MeV/A) is produced using the stable beam acceleration system outlined above, and made incident upon a thick carbon target in which the beam is entirely stopped. The target, shown in Fig. 3.3, has a geometry designed to allow the radionuclides that are produced by fragmentation of the beam to travel to the surface. The primary beam heats the production target to approximately 2000°C, which encourages the diffusion of radionuclides. When they escape the target, these nuclei travel a short distance to a second ECR source and are injected into a fourth cyclotron (the Cyclotron for Ions of Medium Energies, CIME, with $K = 265$) where they are accelerated and directed to the experimental chamber.

A wide range of radionuclides are produced by nuclear reactions when the primary

Figure 3.3: Photograph of the SPIRAL carbon target for the production of radioactive nuclei. [52]

beam strikes the production target, and so the nuclei of interest must be carefully selected to provide a pure beam. The properties of the transfer tube between the production target and the ion source allow only gaseous elements to pass through, and the post acceleration allows fine selection of the produced radionuclides by m/q ratio. In addition, as acceleration of the radioactive beam is performed in the same way as for the primary beam, the beam quality is generally very good compared to other methods of radioactive beam production (such as in-flight fragmentation).

The beam of ^{24}Ne produced for this work had an energy of 3.8 MeV/A (90.7 MeV) and an intensity of 2.9×10^5 pps. The ^{20}Ne beam was provided at 3.49 MeV/A (69.7 MeV) and 2.0×10^8 pps.

3.3 Experimental technique

This work used the Thick Target Inverse Kinematics (TTIK) technique [54], which has a number of advantages over traditional thin target experiments. In a thin target experiment a foil of target nuclei, typically a few μm in thickness, is placed in the path of the beam. Using such a thin target means that the energy loss of the beam nuclei is small, and so the interaction energy is well known; elastic and inelastic scattering events can then be easily identified kinematically. With this technique, however, measurements of the reaction cross section at 0° or 180° are challenging because any detectors placed at these angles would be destroyed by the high intensity beam. Furthermore, a given beam energy only provides a measurement of the elastic scattering cross section for one centre-of-mass (c.m.) energy. In order to generate a full excitation spectrum a different beam energy must be used for each data point, which requires retuning the accelerator hundreds of times. For some facilities this is possible - such as tandem Van de Graaff accelerators - but in many other cases it is prohibitive. In particular, beam tuning at the GANIL-SPIRAL facility takes normally eight hours or more, and so an alternative experimental technique must be used.

The target in this work was helium gas, which is described as thick because the beam is fully stopped within the gas volume. The gas fills the experimental chamber, which is separated from the beamline by a 5 μm Havar foil through which the beam may pass. After the beam enters the chamber it travels through the gas, losing energy due to collisions with the gas molecules, before being stopped after a known distance. At any point before it is stopped, the beam nuclei may interact with the target nuclei resulting in nuclear reactions over a continuous range of energies from zero to the energy at which the beam enters the chamber. In this way, scattering reactions over a wide (many MeV) part of an excitation function can be measured simultaneously.

As the experiment is designed so that the beam nuclei are stopped in the gas and do not reach the detectors, the heavy reaction products are also not detected. Light reaction products, however, such as α particles, lose energy less quickly in the gas and so can be

detected. Although the energy lost by both the beam and the detected nuclei in the target must be taken into account (in addition to the reaction kinematics), full reconstruction of the reaction is still possible based on the type of particle that is detected and the energy that it has upon reaching the detectors.

Most commonly, experiments are performed for practical purposes with light beam nuclei and heavy target nuclei, and this is referred to as *normal* kinematics. In a thick target experiment there are a number of advantages to using an *inverse* kinematics approach. In particular, using a heavy beam and detecting light particles is what allows the pressure to be tuned such that the high intensity beam does not reach the detectors but the low flux of scattered nuclei do. In addition, a detector placed at zero degrees in the laboratory frame corresponds to 180° in the reaction c.m. frame, where the Rutherford cross section is minimum and the resonant scattering cross section is maximum.

In a thin target experiment the excitation energy in the compound nucleus can be determined by either the measured energy of the detected particle, or more commonly the energy of the beam from the accelerator. For tandem Van de Graaff accelerators in particular the beam energy is both well defined and well known, and so high resolution can be achieved. In a thick target experiment, the measured energy must be used and so one limiting factor for the resolution of the measurement is the resolution of the detector system used. An interesting feature of the inverse kinematics approach is that, due to the high c.m. velocity, the resolution of the measurement in the c.m. frame is often many times better than in the laboratory frame - in this work, by as much as a factor of two.

The TTIK approach also provides an improvement to the efficiency of detectors placed at forward angles in the laboratory. Using the notation of Krane [11] for a general scattering reaction of the form

$$a + X \rightarrow Y + b \tag{3.7}$$

where the beam particles are labelled a, the target X, the recoil Y and the detected particles b, the relationship between the c.m. scattering angle of b, θ'_b, and the laboratory

scattering angle, θ_b, is

$$\tan\theta_b = \frac{\sin\theta_b'}{\cos\theta_b' + \gamma} \tag{3.8}$$

with

$$\gamma = \left[\frac{m_a m_b}{m_X m_Y}\frac{T_a}{T_a + Q\,(1 + m_a/m_X)}\right]^{\frac{1}{2}}. \tag{3.9}$$

For elastic scattering the Q-value, Q, is zero, and so γ no longer depends on the kinetic energy of the beam T_a. Further, in the case of inverse kinematics, $m_a = m_Y$ and $m_b = m_X$ so that $\gamma = 1$. This gives

$$\tan\theta_b = \frac{\sin\theta_b'}{\cos\theta_b' + 1} \tag{3.10}$$

or equivalently

$$\theta_b = \frac{\theta_b'}{2}, \tag{3.11}$$

so that the laboratory scattering angle is always half of the c.m. scattering angle. Thus all of the scattered α particles are effectively focused into forward angles, meaning that the efficiency of detectors placed appropriately is doubled.

3.3.1 Inelastic scattering

One challenge of the TTIK approach is the identification of inelastic scattering processes. In a thin target experiment, the beam energy and the detected particle kinetic energy are both known, so any missing energy can be measured - and indeed this is a method of measuring excited states in the target nuclei. In a thick target experiment, the reaction c.m. energy is determined by measuring the energy of the detected particle and to do this elastic scattering must be assumed, *i.e.* after the compound nucleus decays, both of the daughter nuclei are in their ground states. This is normally the case for α particles, for which the first excited state is at 20 MeV, but in ^{24}Ne the first excited state is at 1.6 MeV and so can reasonably be populated.

If the compound nucleus decays via an excited state of neon, then the resulting α particles will have less kinetic energy than expected, and so they will be misinterpreted

as coming from a different part of the excitation spectrum of magnesium. These events will result in duplicate peaks in the measured excitation function, separated from each other by the energies of the states in neon. The areas of each peak will depend on the cross section for the decay to each state, which is invariably much smaller for inelastic scattering than for elastic scattering.

In order to identify these events, it is noted that the very highest energy α particles must result from elastic scattering. Given the energy of the beam as it enters the chamber, the maximum excitation energy in ^{28}Mg that can be populated is E_x^{max}. If the energy required to excite ^{24}Ne to its first excited state is E_{Ne}^1, then α particles that result from excitation energies in ^{28}Mg with $E_x > E_x^{max} - E_{Ne}^1$ must have proceeded through elastic processes only - there is not enough energy to both excite the neon nucleus and for the α particle to arrive at the detector with a kinetic energy corresponding to this region. The high energy part of the spectrum is thus free of inelastic events, and this is true for any beam energy. By changing the beam energy, the clean region can be swept across the excitation function of ^{28}Mg, and a completely clean spectrum can be constructed.

In this work, four Havar degraders were available immediately before the window, with thicknesses of 2, 4, 6 and 8 μm. Each additional 2 μm of Havar reduces the beam energy by approximately 8 MeV and correspondingly the highest available reaction c.m. energy by approximately 1.15 MeV—less than the energy of the first excited state in ^{24}Ne.

3.3.2 Detectors

The detectors used in this work were silicon semiconductor detectors, which are commonly used for charged particle spectroscopy. A semiconductor is a material characterised by having a small energy gap between electrons bound to atoms in the lattice (the valence band) and those that are free to move through the crystal (the conduction band). When a charged particle enters the detector, it loses energy to the crystal by exciting electrons from the valence to the conduction band leaving behind an electron *hole*. The effect of the charged particle as it moves through the crystal is to create many such *electron-hole pairs*,

with the number created being proportional to the energy lost by the incident particle.

With no further outside influence, the electrons now in the conduction band would rapidly de-excite and recombine with the holes. In order to collect the energy information, a bias voltage is placed across the crystal which causes the electrons and holes to flow towards opposite sides of the detector where a charge is built up. The charge collected on each electrode is proportional to the energy deposited by the incident particle, and this signal can be amplified and recorded as described in section 3.4.

In practice, high purity silicon crystals are difficult to manufacture, and the electrical properties are dominated by even a small concentration of impurities. Instead, detectors are manufactured from silicon that has been deliberately doped with a small (but dominant) concentration of a specially chosen impurity. The dopant either provides an excess (n-type) or a deficiency (p-type) of electrons compared to the pure silicon crystal. A p-n junction is the interface between p-type and n-type regions within a single silicon crystal, and at this interface the electrons from the n side flow towards the holes in the p side leaving a *depleted* region where there are no free charge carriers. The depletion region extends until the electric field introduced by the displaced charge carriers opposes any further such motion. Now by applying a voltage to the crystal the depletion region can be made to extend to the full thickness of the detector. Electrons and holes created within the depletion region by a charged particle will flow towards the electrodes under the influence of the applied voltage, and thus can be measured by the charge collected.

In this work an array of silicon strip detectors was used, a perspective drawing of which is shown in Fig. 3.4 with a top-down view of the experimental chamber shown in Fig. 3.5, while the detectors themselves are shown in Fig. 3.6. Strip detectors split the aluminium electrode on one or both faces into smaller parts in order to improve the position resolution available as well as increase the acceptable hit rate. At zero degrees a 50 mm $\times$ 50 mm double sided strip detector was used (Micron Semiconductor W1 design [55]), 1024 μm thick, with orthogonal sets of 16 strips on each face, giving a 32 channel detector with 256 pseudo-pixels. The strip width and pitch were 3.0 mm and 3.1

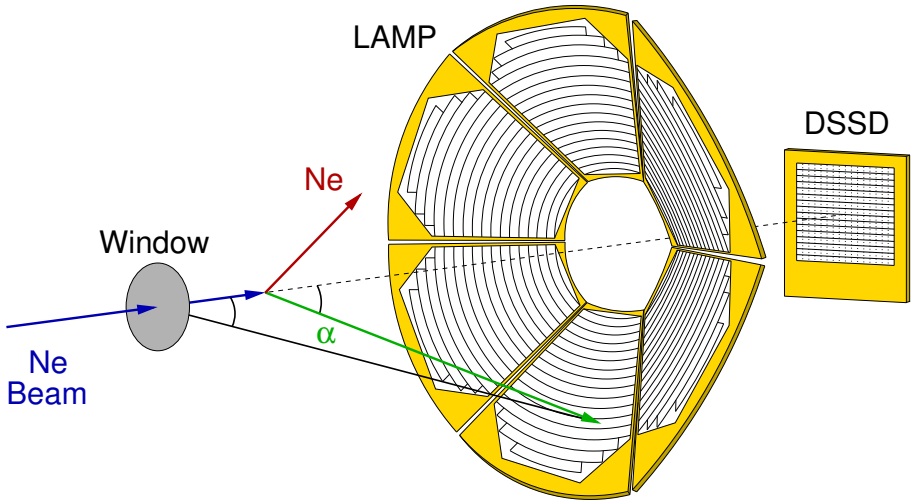

Figure 3.4: Perspective drawing of the detector array used in this experiment. The path of the beam is shown in blue, the recoiling neon in red and the scattered α particle in green. The zero-degree detector is labelled DSSD (double-sided silicon detector). Modified from Ref. [56].

mm respectively. Placed 36 cm from the entrance window, the angular acceptance of this detector was 0–5.5° in the laboratory frame measured relative to the window.

Away from zero degrees an array of six single sided wedge shaped detectors was used (Micron Semiconductor YY1 design [57]), 500 μm thick, each with 16 curved strips, arranged in a 'lampshade' configuration where each detector is angled at 45° to the beam axis. With the beam incident along the z axis and the co-ordinate origin placed at the window, the array provided complete azimuthal coverage and 7–22° coverage in polar angle in the laboratory frame, corresponding to at least 44° in the c.m. frame. The strips were curved so as to represent an approximately constant θ.

3.4 Data acquisition

The data acquisition system consisted of modular electronics components that provided, amongst other things, analogue signal processing, simple event selection and rejection, and analogue-to-digital conversion. The set-up of the electronics is shown in Fig. 3.7. In total for six single-sided detectors and one double-sided detector with 16 channels per face, a 128 channel acquisition system was required.

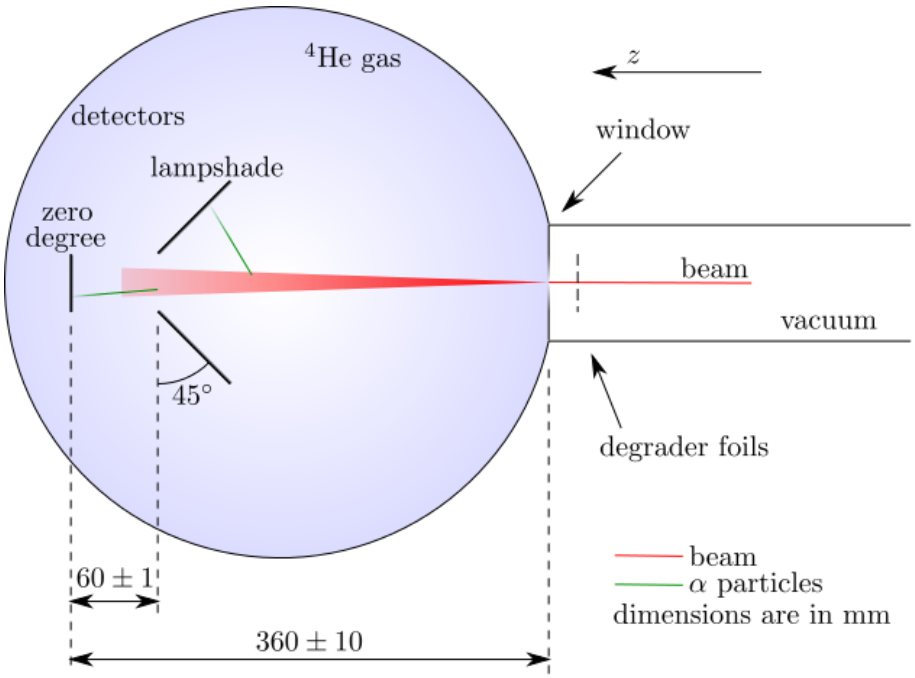

Figure 3.5: Schematic of the experimental set-up. The path of the neon beam is shown in red, while examples of scattered α particles are shown in green. The extent of the helium gas is indicated by blue shading.

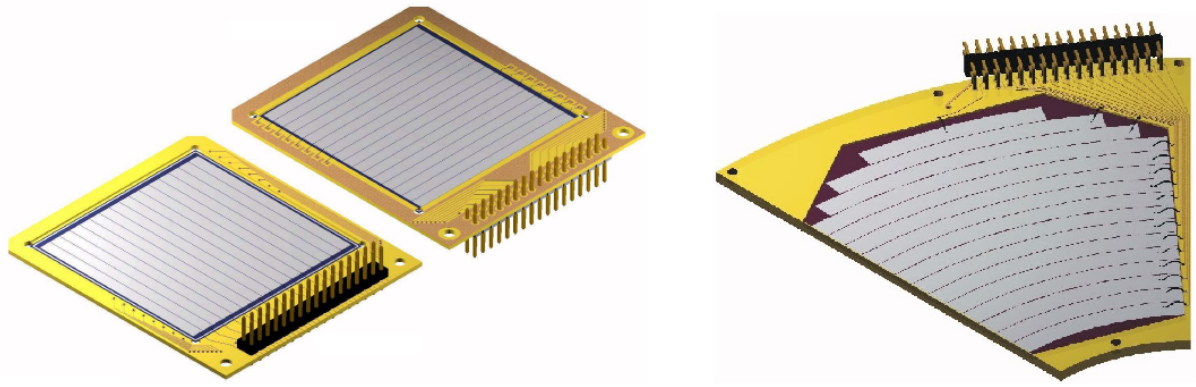

Figure 3.6: The silicon detectors using in this experiment: (left) the W1 double-sided detector, with both sides shown; (right) one of six wedge shaped single-sided YY1 detectors. Both are manufactured by Micron Semiconductor.

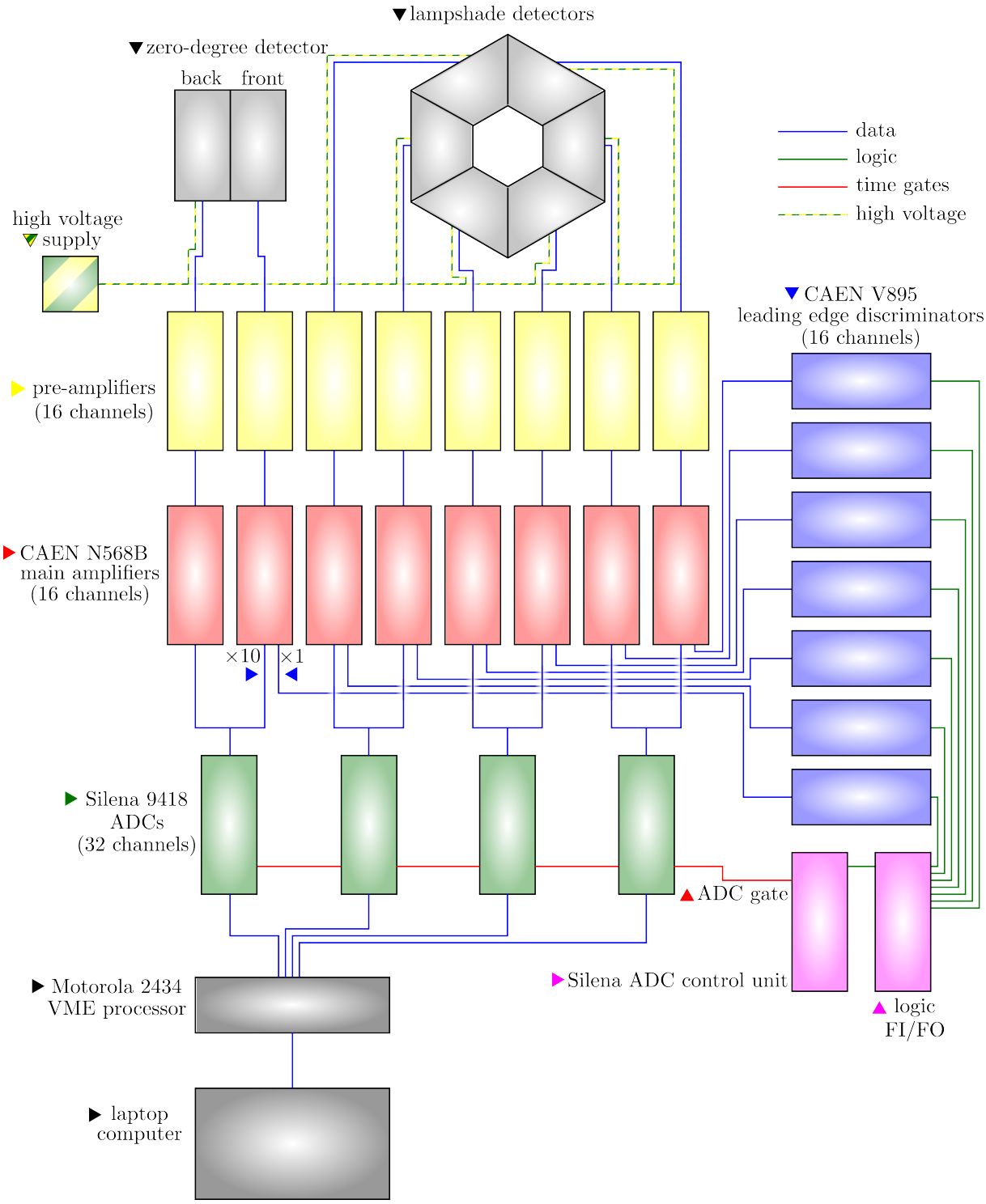

Figure 3.7: Block diagram of the data acquisition system. See text for details.

A reverse bias of 100 V was applied to the back face of the zero degree detector and 70 V to each of the wedge detectors. The charge collected on each electrode was integrated by eight 16-channel pre-amplifiers built within the Charissa collaboration at the University of Paisley, and pulse shaping was performed by eight CAEN N568B 16-channel amplifiers. The times-ten outputs were connected to four 32-channel Silena model 9418 analogue-to-digital convertors (ADCs), and the times-one output to the discriminators to create the trigger.

The data acquisition was set to require a signal in at least one strip in the array. For this purpose, seven of the amplifiers were connected to CAEN V895 leading edge discriminators: the first six for each of the wedge detectors, and the seventh for the front face of the zero degree detector. These units had been modified to provide a positive polarity output pulse as required for the subsequent units. In order to make a singles trigger, the OR output from each discriminator was connected to a logic fan-in/fan-out (FI/FO) unit where they were again combined with OR logic to produce a single signal. The output from the FI/FO was connected to a Silena S941 ADC control (SAC) unit that provided a trigger signal to the ADCs themselves. This signal included an acquisition gate with a width of 5 μs upon the receipt of which the ADCs began converting the signals in all 128 channels. These signals were buffered while waiting to be converted, during which time (≈ 50 μs) the SAC ignored any further signals from the discriminators.

A Motorola 2434 processor was used to interface with a laptop computer where the data were stored, passing on the digital signals from the ADCs and allowing the ADC settings to be controlled from the laptop. The MIDAS software [58] was used to write the data to disk as well as to control the set-up of the main amplifiers and the discriminators.

3.5 Calibration

Calibration was performed using a triple-α source containing ^{239}Pu, ^{241}Am and ^{244}Cm for which the α decay lines are at 5.14, 5.46 and 5.80 MeV (the weighted averages of all of

the possible α decays). In this work, the energies of the detected α particles were up to 30 MeV, so the accuracy of the calibration when extrapolated to these energies depends on the linearity of the detector and electronics.

For the zero degree detector, a fourth calibration point at approximately 70 MeV was obtained by taking data with no gas in the chamber so that the ^{20}Ne beam could reach the detector—at a reduced intensity to avoid radiation damage. With the Havar window still present, the beam was scattered into all pixels of the zero degree detector. This provided a calibration that required interpolation, rather than extrapolation, from the calibration points to the measured energy of the α particles; however using a different nucleus for calibration compared to the experiment (^{20}Ne rather than α) will reduce the accuracy. This is because all charged particles lose some energy before reaching the active region of the detector due to the presence of the electrical contact (in this case 0.3 μm of Al) and the *dead layer* of Si where charge collection is incomplete, the thickness of which is unknown. When performing a calibration with the same nuclei as will be detected, the unknown energy loss is corrected for (to first order); this is not the case when using Ne to calibrate for He.

In order to determine whether a more accurate calibration is obtained with or without the high energy data point from Ne, the calibrated spectra were compared to existing data (see Section 4). This showed that a better calibration was obtained using only the triple-α source, excluding the data point obtained from ^{20}Ne.

3.6 Preliminaries

Before scattering measurements were performed, data were recorded to provide some characterisation of the set-up. With no gas in the chamber, and the ^{20}Ne beam at low intensity to avoid radiation damage, the beam energy was recorded by the zero degree detector after passing through a selection of the Havar degraders and window. When losing energy through the foil, the beam also undergoes energy and angular straggling:

Table 3.1: Thicknesses of Havar degraders as given by comparison of the measured and calculated energy loss of the ^{20}Ne beam through each foil.

Havar foil thickness (μm)	
Nominal	Measured
2	2.0(2)
4	3.9(4)
5	4.9(5)

there is some statistical variation in the magnitude of the energy loss and the beam direction. Figure 3.8 shows 2D histograms of the position of events in the zero degree detector with 0, 2, 4 and 5 μm of Havar in place, the latter being the window which was used for all runs with gas in the chamber. With no Havar in place, the beam spot size was measured by fitting a Gaussian peak to the x and y projections of the histogram, giving a width of 6.6 mm in x and 1.6 mm in y. The beam offset relative to the centre of the detector was given by the centroid in each profile: 1.6 mm in x and 10.9 mm in y.

With the Havar in place, Fig. 3.8 shows the straggling of the beam, *i.e.* the enlargement of the beam spot due to the scattering of the beam in the foil. Figure 3.9 shows the energy spectra obtained with four different thicknesses of Havar (including zero) from which the energy of the beam can be measured. The Havar foils were supplied by Goodfellow [59] with a manufacturing tolerance on the stated thickness of $\pm$25%, and so the energy measurement of the beam after passing through a given Havar foil provides a measurement of the foil thickness, based on the calculated energy loss. Table 3.1 shows the stated and measured thicknesses of the three Havar foils measured in this way. The energy loss codes used are discussed in more detail in section 4.2.1; the variation in the calculations of the different codes has been used to quantify the uncertainty on these calculations and thus the uncertainty on the measured foil thickness. It is found to be approximately $\pm$10%.

The energy straggling of the beam can also be seen in Fig. 3.9 as an increase in peak width. Energy straggling through a medium is proportional to the energy of the beam before the medium (which is the same for all the data series in Fig. 3.9) and the energy loss through it. The energy straggling should, therefore, be largest for the thickest degraders;

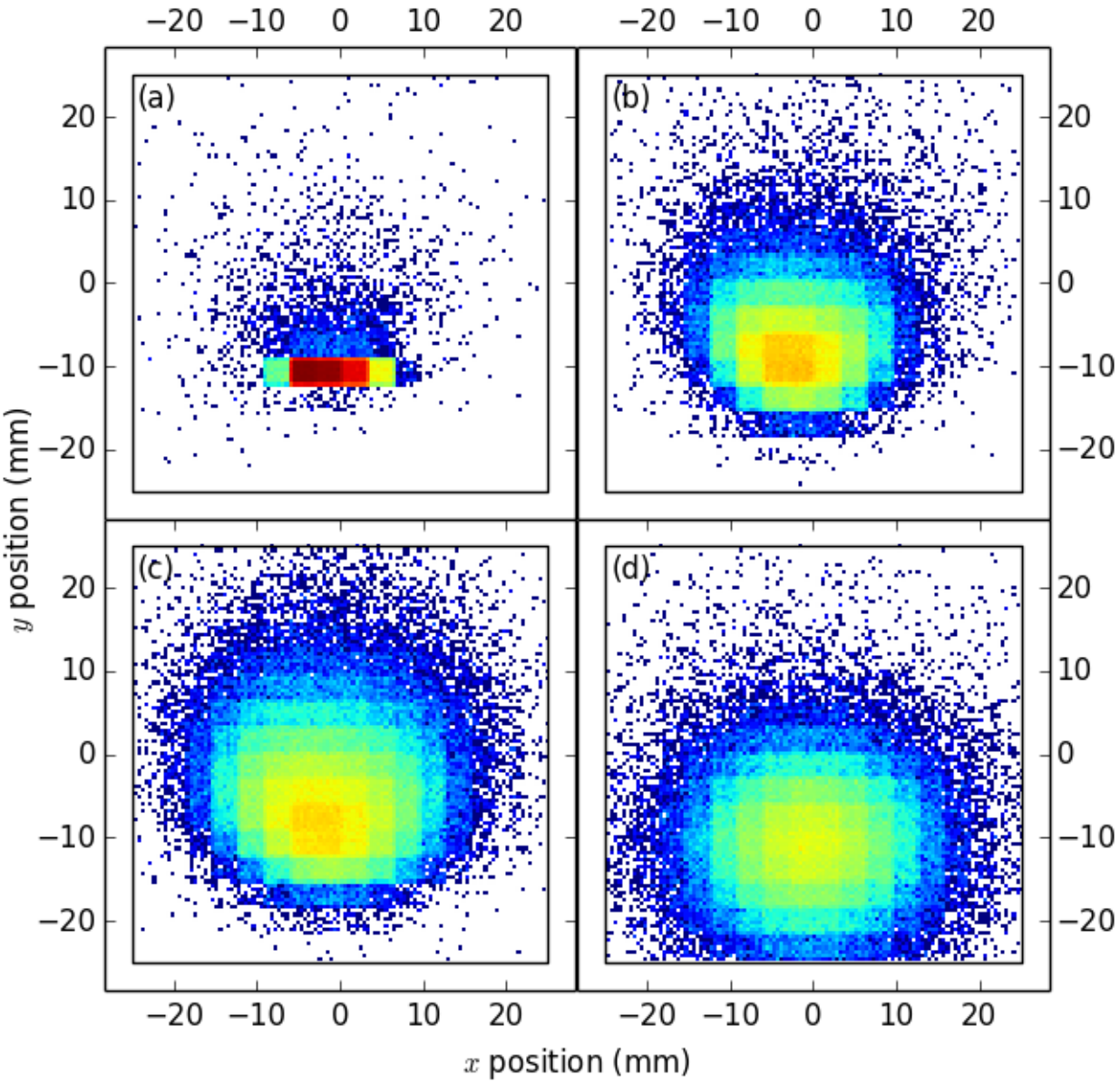

Figure 3.8: Histograms of the position of events in the detector for (a) the beam directly into the detector, (b) through 2 μm of Havar, (c) through 4 μm of Havar and (d) through the 5 μm Havar window. The origin is at the centre of the detector, and the box marks the edge of the detector face.

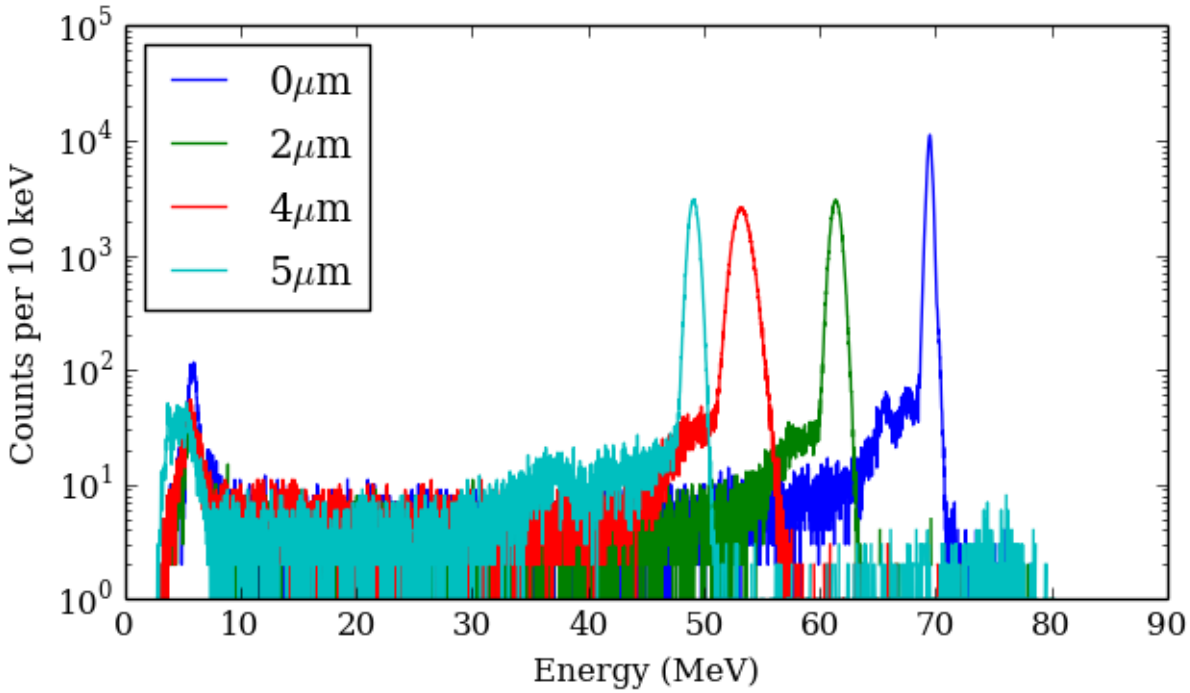

Figure 3.9: Energy spectrum for the ^{20}Ne beam into the zero degree detector through various thicknesses of Havar.

however it can be seen that the straggling is largest for the 4 μm and 2 μm foils. The reason for this is not known, but it should be noted that these degraders are mounted separately from the 5 μm window, and so the cause of the unusually large spread may be related to this.

3.6.1 Multiplicity

Although the electronics trigger required single events, more than one event could be recorded in the same 5 μs time gate due to pile-up, charge sharing, or true coincidences. Only true coincidences contain useful data, the other cases must be identified and discarded. For the single-sided detectors in the lampshade array this is difficult, but for the double-sided detector at zero degrees there are a number of ways of identifying these events by comparing the signals from each face. The data appearing within a single time gate are referred to as an event and the number of acquisition channels containing a use-

ful signal (above a threshold of 1–2 MeV) is referred to as the event *multiplicity*; as time information is not recorded all signals within the same gate are assumed to be exactly coincident.

Pile-up occurs when two or more particles strike the same strip at the same time on either the front or back face of the detector. When this happens, a single pulse is recorded with the sum of the energies of the individual particles, and the information about how this energy was shared between the particles is lost. Charge sharing occurs when a single particle strikes the detector between two strips on one face, resulting in a splitting of the signal between these strips. In this case only part of the energy information is recorded in each strip, resulting in two spurious signals.

In most cases of pile-up and charge sharing there will be a different number of events in each face, allowing the events to be identified. Figure 3.10 shows the distribution of event multiplicities in the zero degree detector for the Ne+α scattering data. Good events can be identified as those that lie on the line $y = x$ as each hit should give a single signal in each face of the detector. As the wedge detectors are only single sided, charge sharing and pile-up events can not be identified in the same way.

If two or more particles strike the detector within the same time gate, and charge sharing or pile-up do not occur, an event with multiplicity greater than one is recorded that is referred to as a true coincidence. In this case, no information is lost and correct interpretation of the event requires only matching the corresponding signals in the front and back faces of the detector.

An effective way to ensure that an event has been correctly interpreted is to check that the energy measured in each face of the detector is the same within the intrinsic detector resolution. Figure 3.11 shows the energy of each event in the front face of the zero degree detector plotted against the energy of the event in the back face with which it has been matched, for ^{20}Ne+α. A variety of conditions are then imposed on the data: in the first case, the only requirement is that for each event in the front face there is a corresponding event in the back face with which to match it. In the second case, the

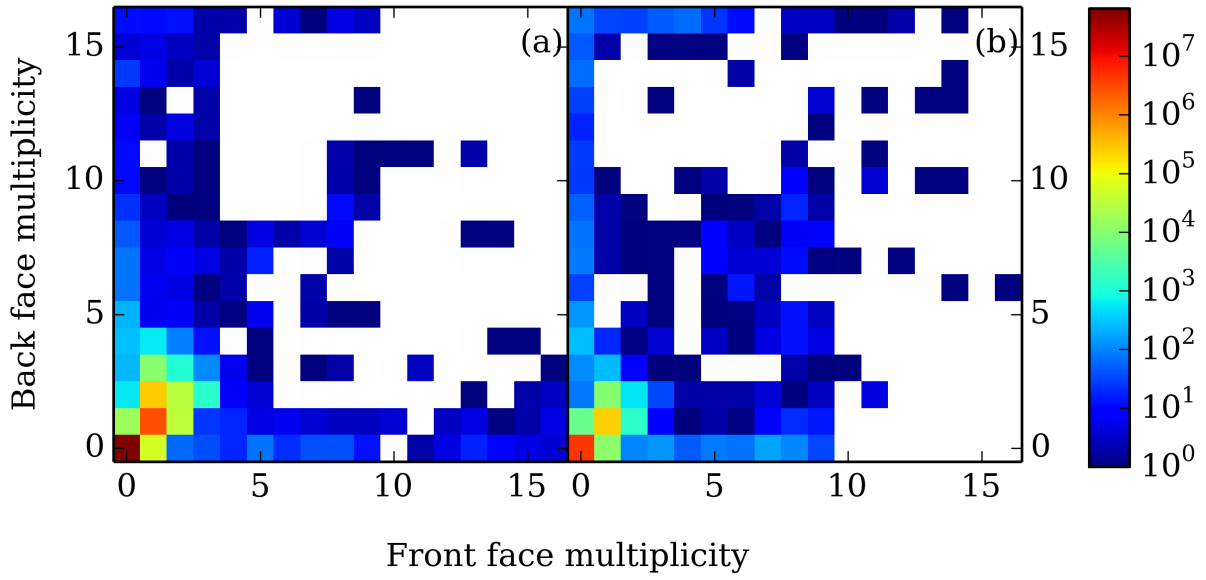

Figure 3.10: Distribution of event multiplicities in each face of the zero degree detector for (a) ^{20}Ne+α and (b) ^{24}Ne+α. Events with multiplicity zero in both faces are possible as there may be events in the lampshade array that triggered data acquisition.

events have been ordered by energy to increase the likelihood of correctly matching the front and back signals when there are more than one. In the third case, the number of signals in each face is required to be the same in order to discard cases of charge sharing or pile-up. Finally, the fourth plot is created with the condition that there is exactly one signal in each face.

Good detector hits will have the same energy measured on each face of the detector (within the detector resolution), and so will lie on the line $y = x$ in Fig. 3.11. The conditions described above exclude events that are not on this line, such as charge sharing or pile-up events. The final condition, requiring that there is exactly one event in each detector face, will also exclude true coincidences. However, as the number of events with multiplicity greater than one is small (1% for ^{20}Ne+α and 0.4% for ^{24}Ne+α), it is assumed that the number of true coincidences rejected in this way is not significant.

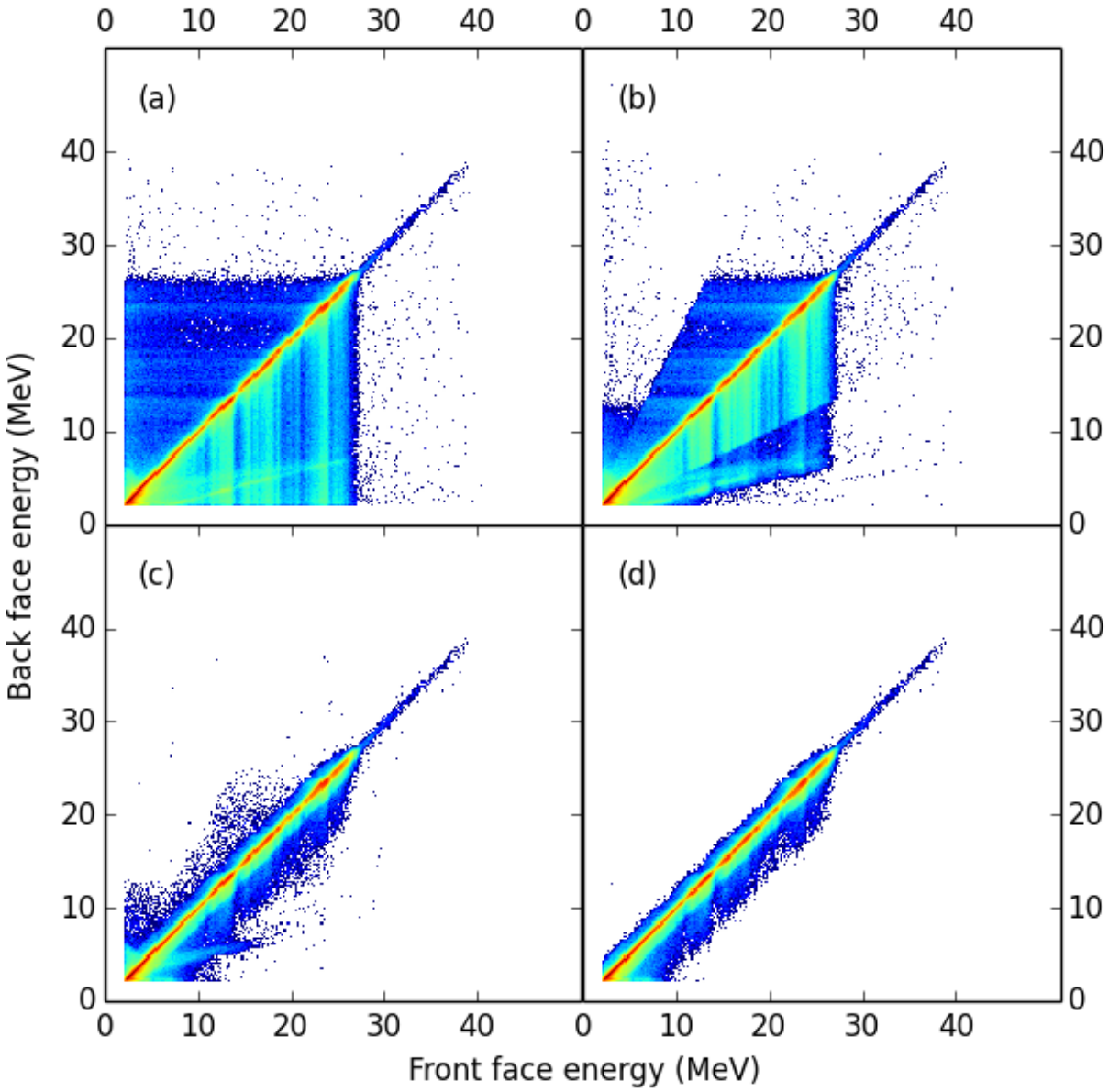

Figure 3.11: Energy of events in each face of the zero degree detector for ^{20}Ne+α showing (a) all recorded signals, (b) after energy ordering, (c) after requiring the number of signals in each face to be the same and (d) after requiring the number of signals in each face to be exactly one.

3.6.2 Dead strips

Of the 128 detector channels in the experiment, four did not function. These were all in the lampshade array, and so a correction must be applied in order to give the correct angular distributions. For each missing strip, the data from the corresponding strip in another detector were duplicated, effectively scaling the number of counts by a factor of 6/5, so that the angular distributions were self consistent. The only effect of the missing strips was then an increase in statistical uncertainties by a factor of $\sqrt{6/5} \approx 1.1$, which is tolerably small.

3.6.3 Resolution

The *intrinsic* energy resolution of the detectors refers to the uncertainty in the measured energy of each individual event. This depends on both the detectors themselves and the associated electronics. The resolution of the experiment as a whole may be different, and this will be discussed in more detail in Section 4.2, but it depends in part on the intrinsic resolution.

Since the triple-α source used for calibration emits α particles from states with natural widths that are essentially zero ($\ll 1$ eV), the measured peak widths for these α particles are due entirely to the detector resolution. Figure 3.12 shows the energy spectrum of the triple alpha source for the sum of all the strips in the zero degree detector and the lampshade array, with three Gaussian peaks fitted to the data on top of a quadratic background term in each case. The widths of each peak in the zero degree detector were 94.6, 93.8 and 94.3 keV, with a fitting uncertainty of 0.2 keV on each, and the mean is thus 94.2 ± 0.1 keV FWHM. The widths measured in the lampshade array were 116.7, 113.8 and 116.2 keV, giving a mean of 115.6 ± 0.1 keV.

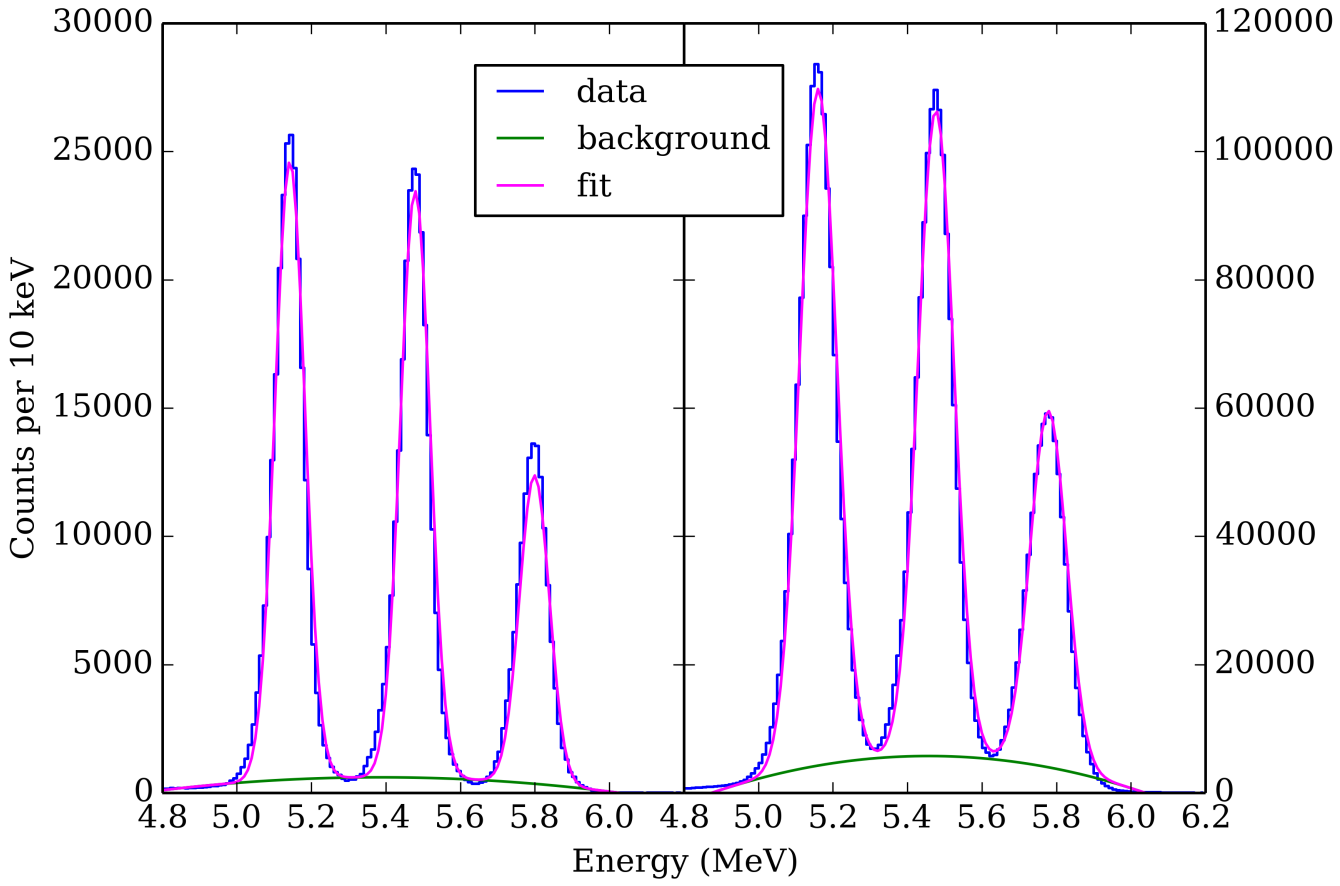

Figure 3.12: Energy spectrum for the triple-α source, with data from (left) the zero degree detector, and (right) the lampshade array. For each, a fit using three Gaussian peaks on top of a quadratic background is shown.

3.6.4 Particle identification

No provision was made in the experimental set-up for particle identification; however, this has not been problematic in the analysis. In the case of ^{24}Mg sufficient previous data are available for comparison in order to identify any parts of the spectrum that are contributed by other channels. These comparisons are discussed in more detail in section 4.

For ^{28}Mg no previous data are available and so such comparisons cannot be made. The energy range measured in this work covers three open channels: α (by definition), neutron, and proton. Neutrons cannot be detected with this experiment and so cannot contaminate the spectrum. The threshold for proton decay in ^{28}Mg is 16.8 MeV, and so can be expected to be strongly suppressed by the Coulomb barrier for the entire measured energy range. The assumption that α particles have been detected is therefore expected to be good.

Chapter 4

Magnesium-24

4.1 Data

The data taken for this work are summarised in Tab. 4.1, showing the combinations of beams, degrader thicknesses and gas pressures used, with the data collection time shown for each. The thickness of Havar stated is the nominal (rather than measured) thickness including the 5 μm window and any degraders used. The energy after the Havar is the energy with which the beam enters the gas, and so is the highest energy at which reactions can occur. Also shown is the corresponding excitation energy in the relevant compound nucleus, which defines the region in which the excitation function has been measured. For each beam, the majority of the analysis is performed using the highest beam energy, and the others are used to identify any inelastic contaminants.

4.2 Common analysis

The analyses of the data for ^{24}Mg and ^{28}Mg share many common steps, and so these are described here with reference to the data for ^{24}Mg. The same methods described in this section have also been used in the analysis of the data for ^{28}Mg.

As described in Section 3.3, in order to reconstruct the excitation energy spectra the kinematics of the reaction and the energy loss of both the beam and the detected α parti-

Table 4.1: Details of the data taken for this work, showing the beam species, degrader and gas pressure used, and the running time for each configuration. The energy of the beam as it enters the target is E_{Ne}, and the excitation energy in the compound nucleus for reactions occurring at this point is E_x^{Mg}.

Beam	Energy	Thickness of	Energy (MeV)		Gas pressure	Run time
	(MeV/A)	Havar (μm)	E_{Ne} max	E_x^{Mg} max	(mbar)	(hours)
^{20}Ne	3.49	5	48.831	17.446	720	7
		7	39.446	15.890	720	2
^{24}Ne	3.78	7	62.587	20.431	985	34
		9	53.545	19.139	985	7.5
		11	43.951	17.769	665	16
		13	33.671	16.300	665	12

cles in the helium gas must be taken into account. As each reaction energy corresponds to a particular depth in the gas, the energy loss of both the beam and recoil will depend on excitation energy. There remains, however, a one-to-one correspondence between the excitation energy of the reaction and the energy of the detected α particle if elastic scattering is assumed, and so by calculating the energies for a reaction at a given excitation energy in the forwards direction, each detected energy can be matched to the corresponding excitation energy, as shown in Fig. 4.1. In practice, this conversion is performed by fitting a polynomial function to the results of the energy-loss calculations; this polynomial can then be quickly evaluated by the analysis code in order to find the reaction c.m. energy given the detected energy.

It can be seen from Fig. 4.1 why the energy resolution is better in the c.m. frame than in the laboratory frame. The excitation energy is matched to the detected energy with a gradient of less than one, and so the excitation spectrum is effectively spread in energy by the frame conversion, increasing the resolving power of the detectors.

4.2.1 Energy-loss code

A number of important parameters depend upon the position in the chamber of each interaction, such as the detector efficiency and the energy loss of the α particles between

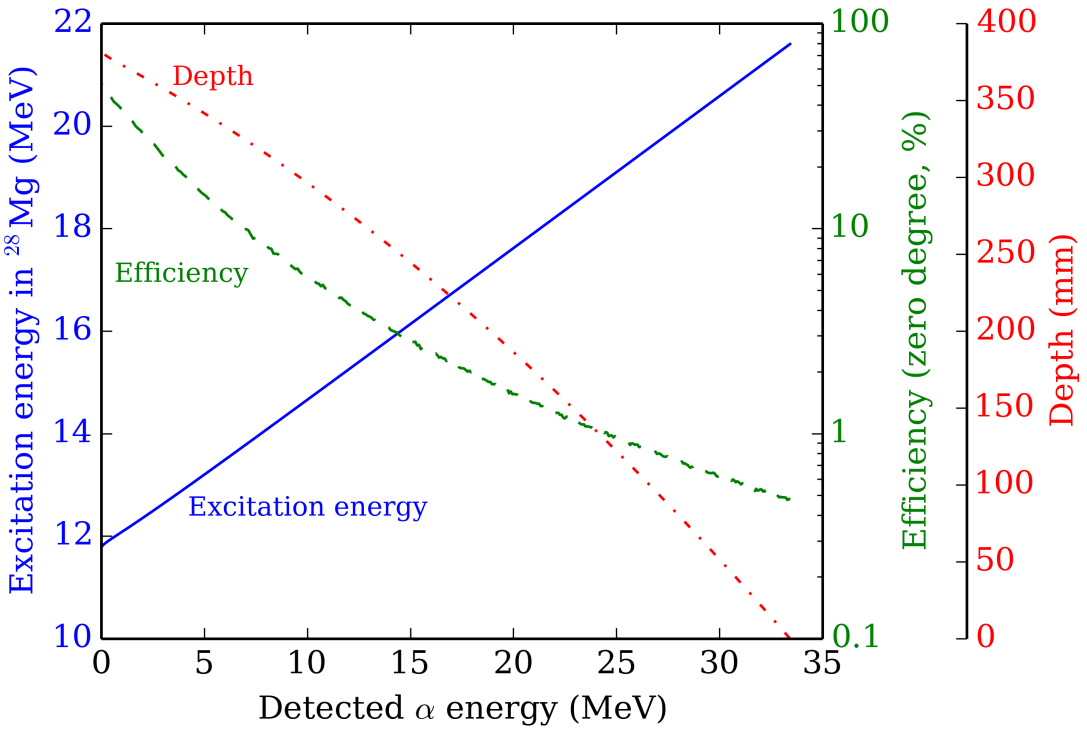

Figure 4.1: Properties of the interaction as a function of the energy of the detected α particle for ^{24}Ne+α through 7 μm of Havar, showing excitation energy (blue solid line), depth into the gas from the window (red dot-dashed line), and efficiency for detection of events at this depth by the zero-degree detector (green dashed line). Elastic scattering is assumed.

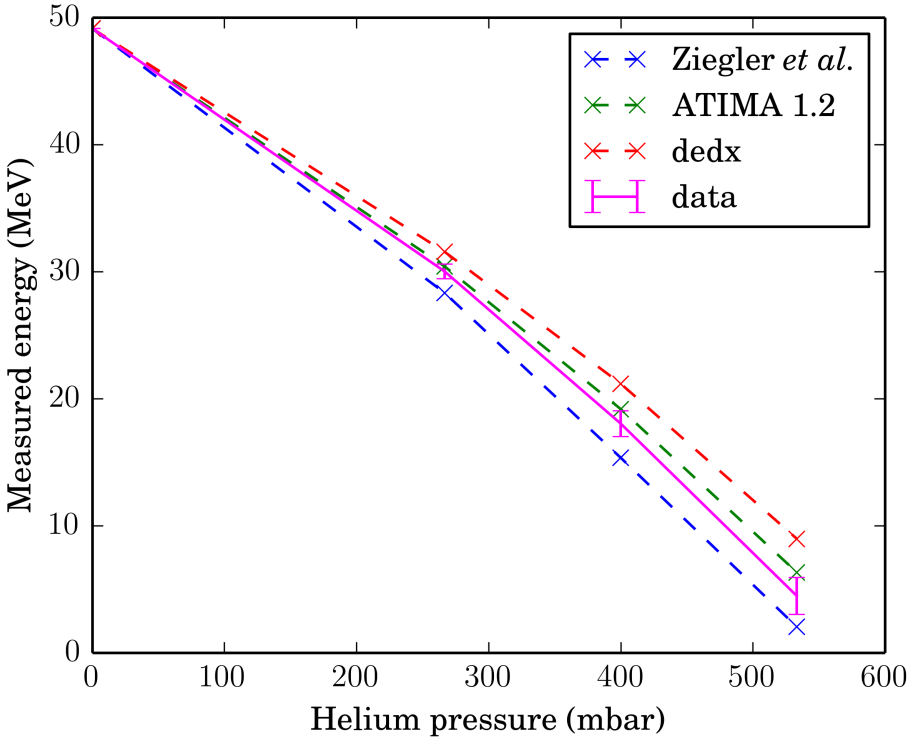

Figure 4.2: Comparison of energy loss codes of Ziegler *et al.* [61] (blue dashed line), ATIMA 1.2 [60] (green dashed line) (both of which are included in the software LISE++ [62] and dedx [63] (red dashed line) to data (magenta solid line) taken for the energy loss of the beam between the entrance window and the zero-degree detector, as a function of gas pressure. The uncertainty on the data points comes from the uncertainty on the window detector distance, which is 36 ± 1 cm. The ATIMA code best reproduces the data, and is used in this analysis to calculate the energy loss of Ne through He gas.

the interaction and the detector. The position in the chamber of events of a given energy depends upon the energy loss of the beam through the gas, and as such the choice of energy-loss code is important. In order to benchmark the available codes, the energy of the ^{20}Ne beam was measured by the zero-degree detector after passing through He gas at various pressures and this was then compared to the predictions of various codes, as shown in Fig. 4.2. The data is best reproduced by the ATIMA code [60], and so this is used to calculate energy loss throughout this analysis.

4.2.2 Monte-Carlo code

An in-house Monte-Carlo code, Resonant EXcitation function simulation (REX, written by Neil Curtis and described in detail in Ref. [56] with reference to the data for ^{24}Mg of the current work), was used to characterise the performance of the experimental technique and reconstruction. The code generates events according to a given excitation function and angular distribution, preserving the correct relative probabilities of a scattering event occurring at a given energy and angle. The energy dependence can either be constant, follow the Rutherford cross section, or be a sum of Gaussian peaks with independent strengths and widths. The angular distribution can either be constant, follow a Legendre polynomial of a given order, or have the $\sin^{-4}(\theta/2)$ dependence of the Rutherford cross section; in the case of multiple states it can be defined independently for each. The simulation takes into account all of the experimental effects such as energy loss, energy and angular straggling, and kinematics, and records the energy of any particles that reach one of the defined set of detectors. The output of the code is a list of detected particles, recording the energy of each as well as the detector and strip at which each was detected.

The REX output can be analysed in a manner identical to the experimental data, and by comparing the events generated by the code to those detected the quality of the analysis method can be determined. By allowing the user to include or exclude individual effects simulated by the code (such as straggling of the beam or the intrinsic detector resolution) the effect of each on the measurement can be determined independently.

This code was used to investigate the efficiency and resolution of the experimental set-up. In the first case, by simulating an excitation function that is completely uniform, i.e. the probability of a scattering event does not depend on energy or angle, then the number of events detected as a function of energy and angle gives an efficiency profile for the detector array. This profile is shown in Fig. 4.3 (a) and (b) for ^{24}Mg and ^{28}Mg respectively. The narrow block of events on the left hand side of these plots is the zero-degree detector, which has an acceptance of 0 to 5.5° as measured in the laboratory frame relative to the entrance window. It can be seen that the efficiency is highest for

low energy α particles, as these are the result of scattering close to the detector. The efficiency increases linearly with laboratory angle until the angle representing the largest circle that fits on the face of the square detector is reached, after which it decreases again as the hits become confined to the corners of the detector. For the lampshade array, efficiency is highest for low energies and low scattering angles. The final three strips of the wedge detectors subtend a smaller azimuthal angle than the first 13, and so a step change in efficiency can be seen at the largest angles. Panels (c) and (d) show simulations of discrete states: six states in ^{24}Mg and eight states in ^{28}Mg respectively. States are placed 1 MeV apart in excitation energy, with widths of 1 keV, so that the measured width gives the experimental resolution as a function of energy and angle. In addition, while in the c.m. frame the dependence of the energy of the scattered α particle with angle is straightforward to calculate, the conversion into the laboratory frame and projection onto the detector geometry is not trivial. The simulations allow the kinematic lines for each state to be found easily.

Efficiency and resolution are discussed in more detail in the following sections.

4.2.3 Resolution

The resolution measured from the widths of states in Fig. 4.3 (c) and (d) is shown in Fig. 4.4 for both ^{24}Mg and ^{28}Mg for the sum of all pixels in the zero-degree detector and four of the 16 strips of the lampshade array. The trend of better resolution at smaller scattering angles is clear. In Ref. [56] the contribution of each experimental effect to the resolution is investigated in detail, and it is found that the angular straggling of the beam in the entrance window is the dominant effect. This is shown in Fig. 4.5, taken from Ref. [56], which plots measurements of resolution for ^{24}Mg with the same method as above, but with different experimental effects active. Also shown is a calculation of what the resolution would be if the Havar window was replaced by a Mylar or Kevlar window of the same thickness. Because these materials are not as strong as Havar, in the simulation the gas pressure has been halved and the distance between the detectors and

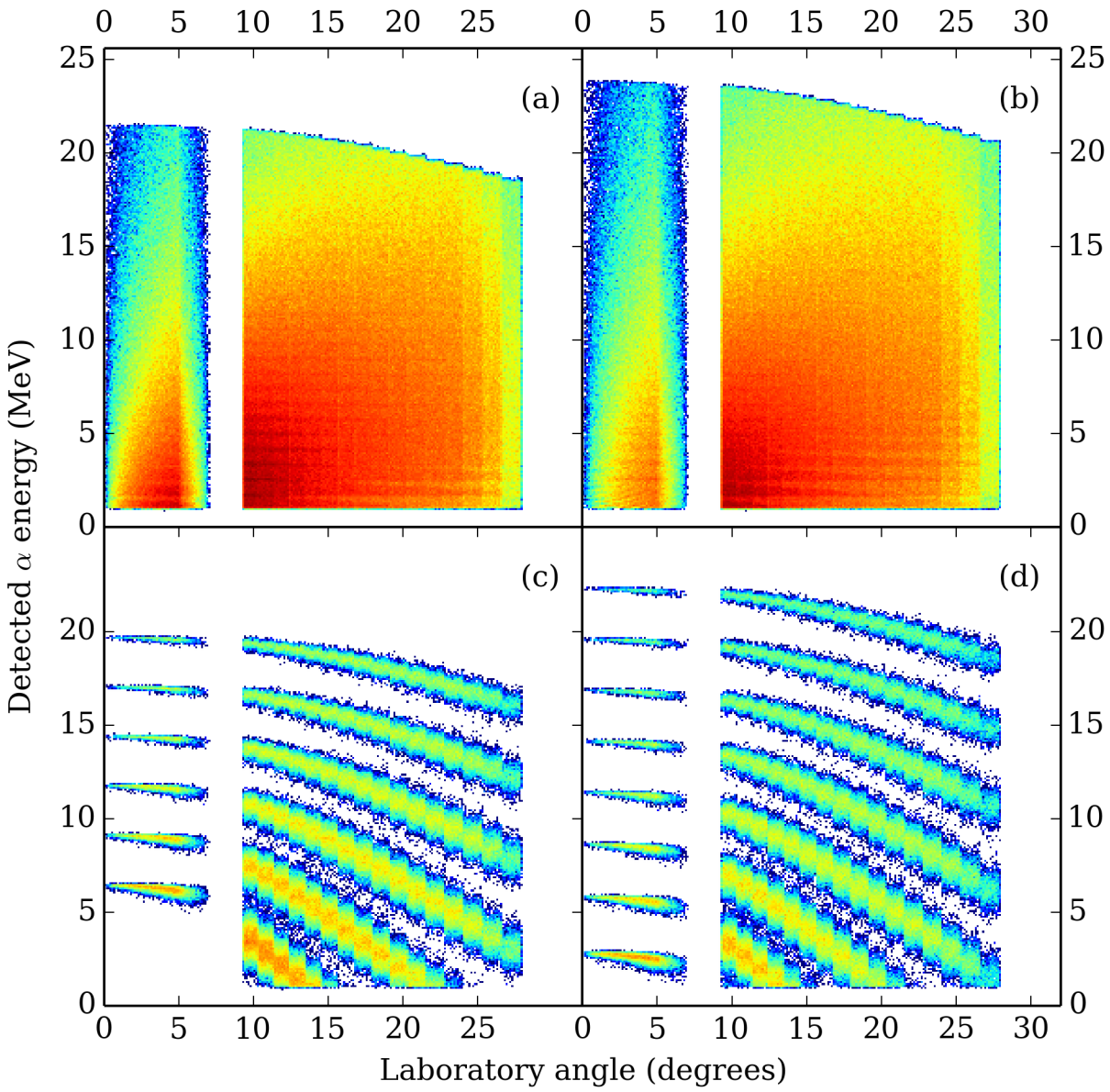

Figure 4.3: Two-dimensional histograms of data simulated using REX, plotted as a function of measured energy and angle, where the angle is that of the detector relative to the chamber entrance window in the laboratory frame. The top row shows simulations of an excitation function that is uniform in energy and angle, and the bottom row shows discrete states with uniform angular distributions. These simulations have been performed separately for ^{24}Mg (left column) and ^{28}Mg (right column). The colour scale is a standard logarithmic heat map. See text for details.

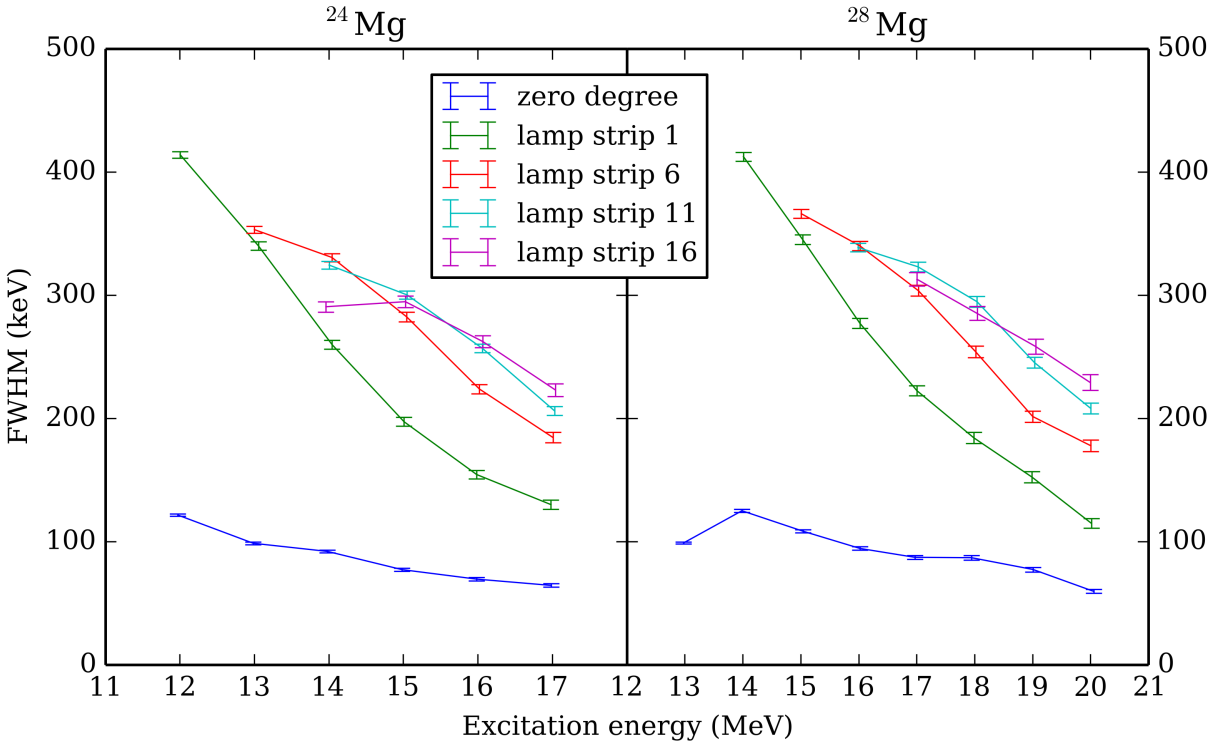

Figure 4.4: FWHM in the c.m. frame as a function of excitation energy for the zero-degree detector and four strips of the lampshade array, showing (left) ^{24}Mg and (right) ^{28}Mg. Strip 1 represents the smallest scattering angle and strip 16 the largest. Uncertainties shown come from statistical fitting errors.

the window has been doubled. See Ref. [56] for details.

As the resolution in the lampshade array is much poorer than in the zero-degree detector, the excitation functions shown in this thesis use data from only the zero-degree detector. The data from the lampshade array are then used to provide angular distributions for states measured at zero degrees.

4.2.4 Efficiency correction

As the distance between the interactions and the detectors changes as a function of the interaction energy, so does the geometric acceptance of the detectors—high energy events are far from the detectors, and low energy events are close to them—so a correction must be applied to provide a relative normalisation of the cross section. There are two ways of applying this correction: the Monte-Carlo method, and the event rejection method.

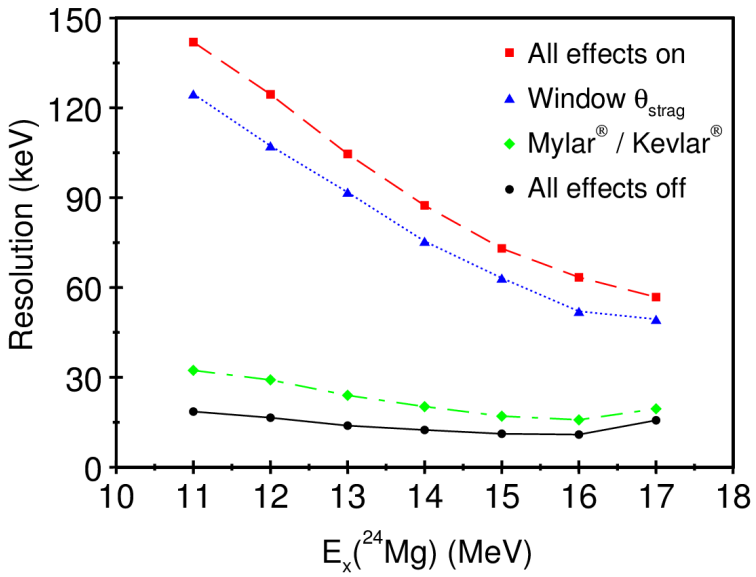

Figure 4.5: Contributions to the total FWHM in the zero-degree detector as a function of excitation energy, as predicted by REX simulations [56], showing results with all smearing effects turned off (black circles and solid line) and with all effects on (red squares and dashed line). Angular straggling of the beam in the entrance window (blue triangles and dotted line) is the dominant contribution to the resolution. Also shown is the simulated resolution achieved by replacing the Havar window with Mylar or Kevlar (green diamonds and dot-dashed line) of the same thickness (facilitated by halving the gas pressured and doubling the window-detector distance), and with the beam energy tuned so that the energy immediately after the window remains the same.

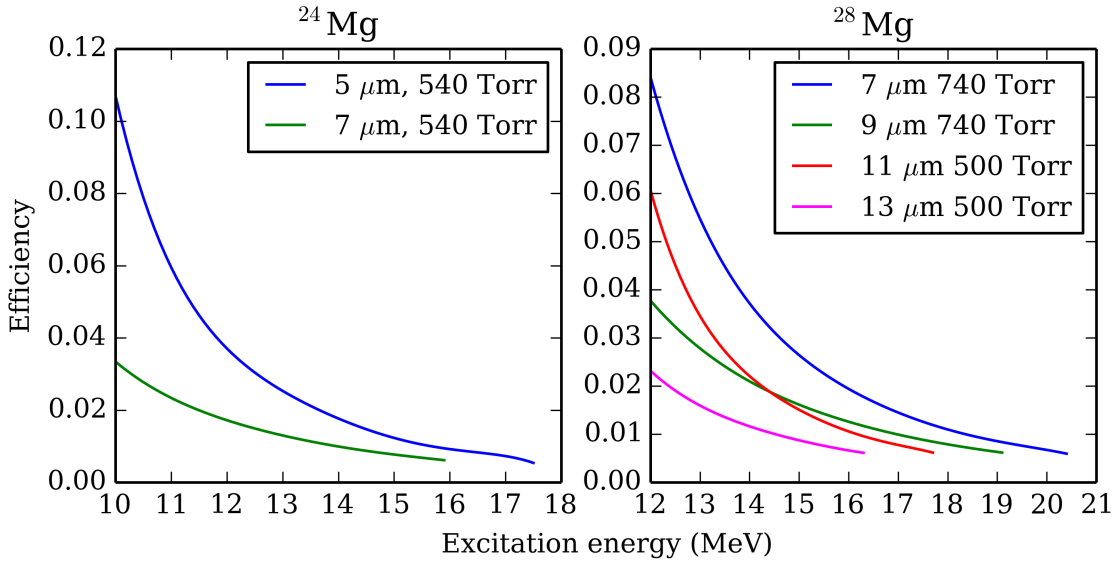

Figure 4.6: Efficiency profiles calculated using a Monte-Carlo simulation for (left) ^{24}Mg and (right) ^{28}Mg, showing each combination of degrader thickness (including the 5 μm window) and gas pressure.

In the first case, a Monte-Carlo simulation is used to find the geometric efficiency of the zero-degree detector as a function of energy. The data are then divided by the efficiency, and the result is a spectrum with the correct relative cross-section measurement. The efficiency as a function of excitation energy in the compound nucleus calculated this way is shown in Fig. 4.6.

The second method is used to correct for the asymmetric peak shape that results from using a detector of finite size on the beam axis. Kinematically, the highest energy α particles are those scattered at 180°in the c.m. frame (zero degrees in the laboratory frame); those scattered at small angles relative to the beam axis are lower in energy but are still accepted by the detector, resulting in peaks with more events on the low energy side in the spectrum. This effect is greater for lower energies, as the zero-degree detector has a larger angular acceptance for these events.

To limit this effect, the maximum accepted scattering angle can be forced to be constant for all events, as shown in Fig. 4.7. The position of each event in the chamber as a function of energy can be calculated, and this along with the position of the event in the detector gives the scattering angle. The maximum scattering angle is chosen to be the

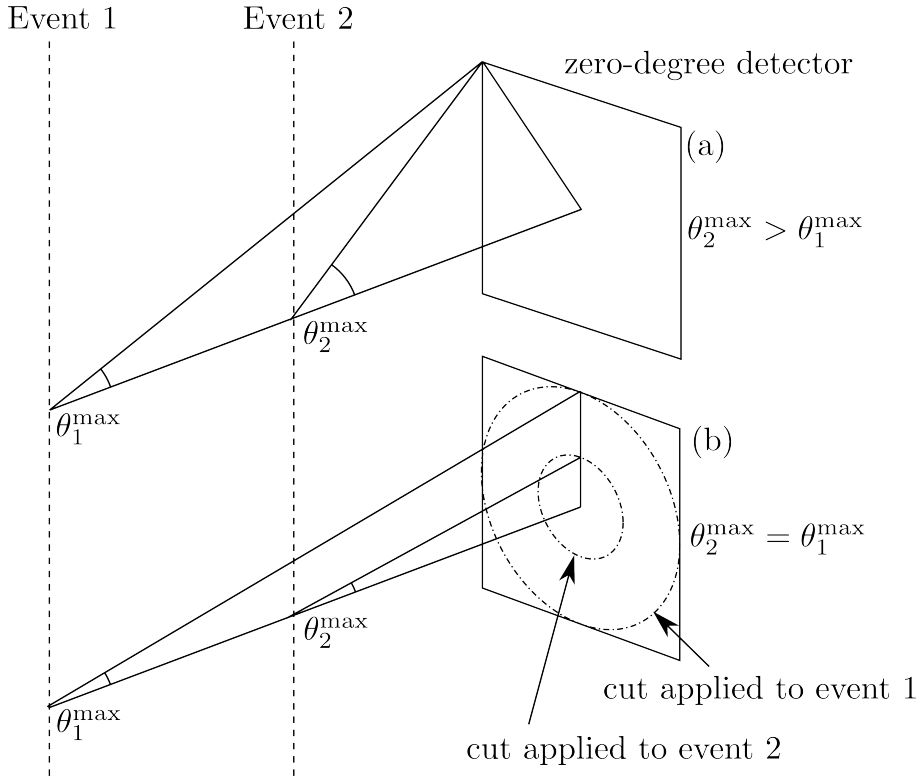

Figure 4.7: Comparison of efficiency correction methods for a thick gas target experiment: (a) all events are accepted and the cross section is normalised using a Monte Carlo simulation, and (b) events are rejected based on scattering angle. In (b), the count rate is reduced and the same angular range is measured for all energies.

same as for the highest energy events that interact at the entrance window, and events that scatter at larger angles are rejected.

The detected position of each event is only know as well as the pixel size, and so for pixels that are partially accepted the position of each event is randomised within the pixel before the cut is applied. In this way these pixels are partially rejected, and the number of events rejected overall is a continuous function of energy.

As the Monte Carlo method does not reject any events, the statistical uncertainties are not affected. The event rejection method improves the shape of the measured excitation function at the expense of statistics. The effect of the choice of efficiency correction method on resolution was found by applying both corrections to the data simulated by REX shown in Fig. 4.3, and these data are shown in Fig. 4.8. Clearly by rejecting events in the low energy tail of each peak the resolution is improved.

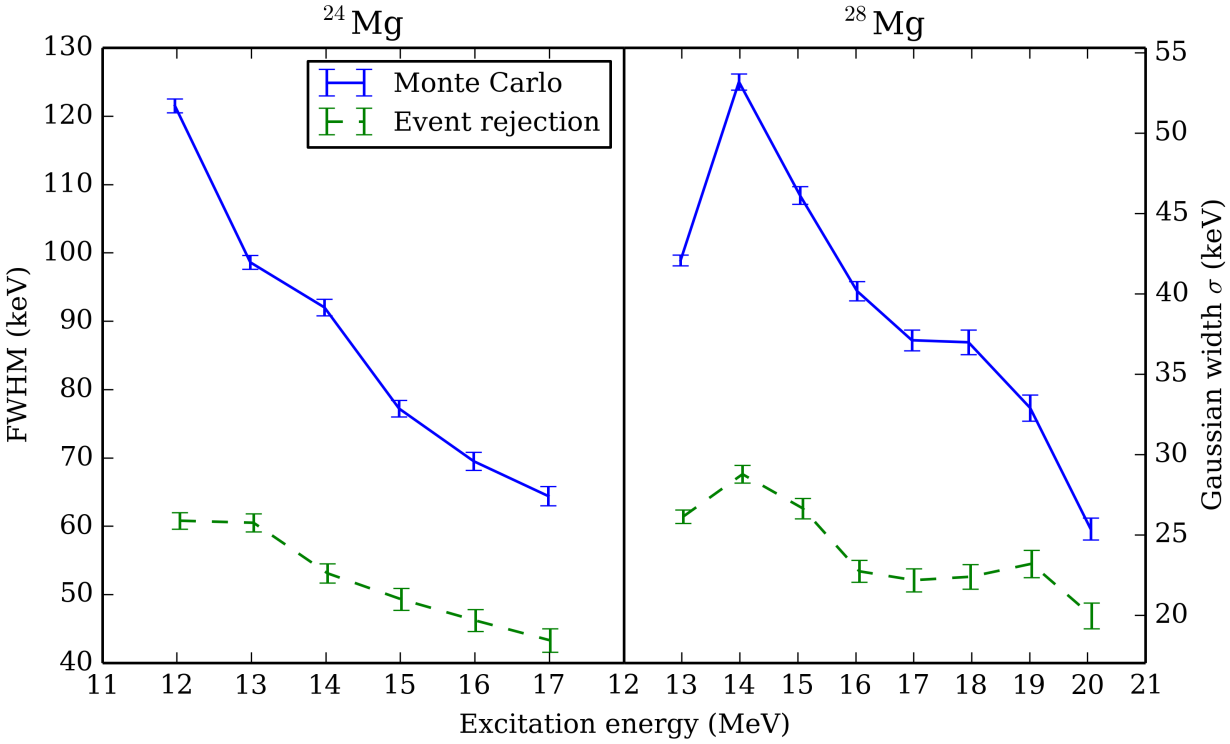

Figure 4.8: FWHM as a function of energy as predicted by REX for (left) ^{28}Mg and (right) ^{24}Mg. Error bars represent fitting uncertainties. The FWHM is obtained for both types of efficiency correction: Monte Carlo (blue solid line) and event rejection (green dashed line).

4.2.5 Normalisation

After the efficiency correction the spectra obtained are corrected for the energy dependent change in count rate, so that the number of counts in each histogram bin is now proportional to the cross section. In order to provide a measurement of the absolute cross section, a further overall normalisation is required to correct for target thickness, beam intensity, and dead time. This is performed using a calculation of the Rutherford scattering cross section, $\mathrm{d}\sigma_c/\mathrm{d}\Omega$, which is given by

$$\frac{\mathrm{d}\sigma_c}{\mathrm{d}\Omega} = \frac{\eta^2}{4k^2 \sin^4(\theta/2)} \tag{4.1}$$

for the wave number k, and the Sommerfeld parameter η; this cross section can then be compared to the Rutherford scattering that is present in the low energy part of the measured energy spectra. The choice of scattering angle for the calculation depends on the efficiency correction method used.

If the event rejection method has been used for efficiency correction, then the available scattering angles are the same for all energies, and the weighted mean of all the available angles is used for the calculation. If the Monte-Carlo method is used for efficiency correction, then the range of scattering angles that are available changes as a function of energy. In this case, the weighted mean scattering angle is calculated as a function of depth in the chamber, and thus as a function of energy. Then this energy dependent scattering angle is used in the calculation, modifying the normal $1/E^2$ shape of the Rutherford cross section to better match the measured shape.

4.3 Results

The excitation function of ^{24}Mg is shown in Fig. 4.9, where both of the efficiency correction methods outlined in Section 4.2.4 are compared. The spectrum corrected using the event rejection method has been normalised to the Rutherford cross section calculated

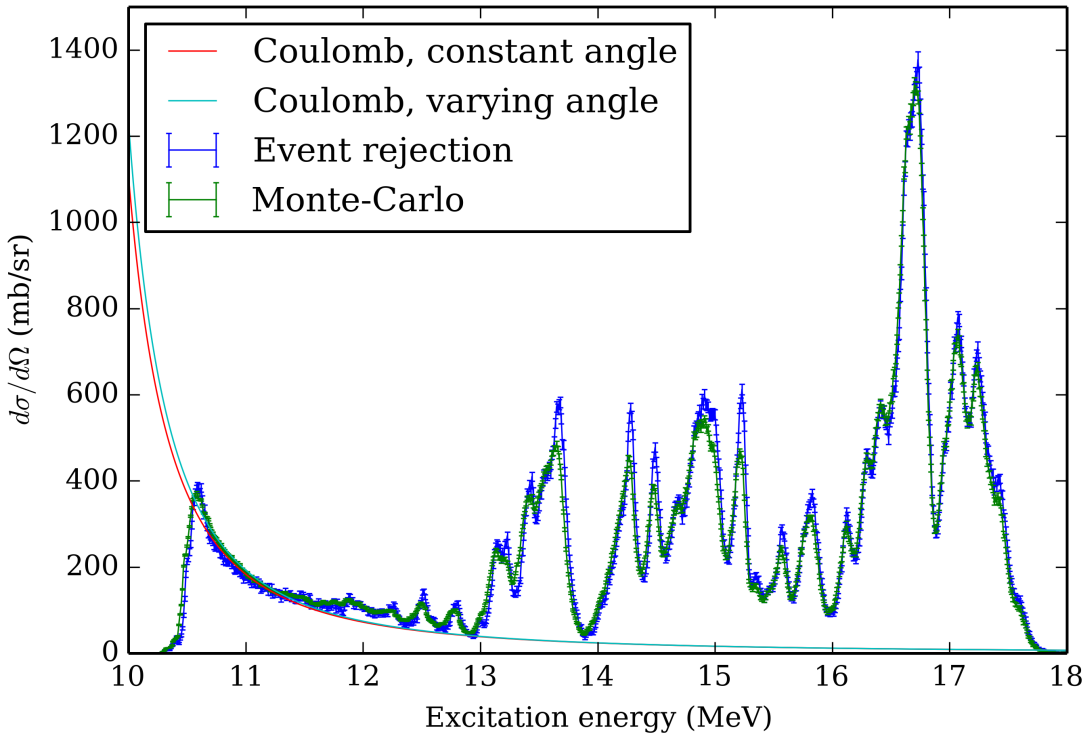

Figure 4.9: Comparison of efficiency correction methods for the excitation function of ^{24}Mg, both normalised to the calculated Rutherford cross section. The event rejection method provides an improvement in resolution due to the reduction of kinematic broadening of the peaks, with only a small increase in statistical uncertainties. Each data set has been normalised to the Rutherford cross section calculated with either a constant angle (for the event rejection method) or a varying angle (for the Monte-Carlo method). See text for details.

at a constant angle, and the data corrected using the Monte-Carlo method have been normalised using a Rutherford cross section with an energy dependent scattering angle, as described in Section 4.2.4. It can be seen that the event rejection method provides an improvement in resolution, as the kinematic broadening of peaks is limited (especially at low energies), at the cost of a small increase in statistical uncertainties. Unless otherwise stated the excitation function corrected using the event rejection approach is used in the rest of this thesis for the ^{24}Mg data.

Data were recorded for ^{24}Mg with two beam energies, and the two resulting spectra are compared in Fig. 4.10 with the highest available excitation energy marked in each case. They have been normalised to each other using the Rutherford cross section between 11.0

and 11.5 MeV. The first excited state of ^{20}Ne is at 1.6 MeV, and so inelastic contributions could be identified above 14.3 MeV. Also shown is the difference between the two spectra, from which it can be seen that the largest differences are observed on the low energy side of each peak. This occurs because when the beam energy is changed, the position of events corresponding to a given state is moved within the chamber and so the angular size of the zero-degree detector changes. States populated close to the detector are measured with an asymmetric peak shape that has a low energy tail caused by kinematic fall-off of α-particle energies from the centre to the edge of the detector; for states that are populated further from the detectors the kinematic broadening of the peaks is reduced and so the measured peak is closer to the symmetric Gaussian shape. In Fig. 4.10 the data taken with the lower beam energy result in peaks that are populated further from the detectors and therefore have more symmetric shapes. Aside from this effect the agreement is generally good, though possible inelastic contaminants can be seen at 14.7 and 15.4 MeV.

4.3.1 Previous data

The excitation function of ^{24}Mg is compared in Fig. 4.11 to the data of Abegg and Davis [64] who measured the elastic scattering of α particles from a thin ^{20}Ne gas target in normal kinematics. The data were obtained from Ref. [64] by digitising the spectrum presented in the paper using the Engauge Digitizer software [65]. The resolution for the thin target data is better than for the current work, because it depends only on the energy loss of the beam in the target and the energy spread of the beam from the accelerator, which are both small. For this reason, the data are also shown after convolution with a resolution of $\sigma = 30$ keV to show that the shapes of the excitation functions match well. Finally, in the normal kinematics experiment, the cross section cannot be measured at $\theta_{\mathrm{c.m.}} = 180°$, so the data used for comparison are from the closest available angle, which is $\theta_{\mathrm{c.m.}} = 168°$. The angular dependence of the cross section of these states is interpreted as the reason for the difference in magnitude between the two data sets. This difference increases with excitation energy as states with higher spins (and thus more

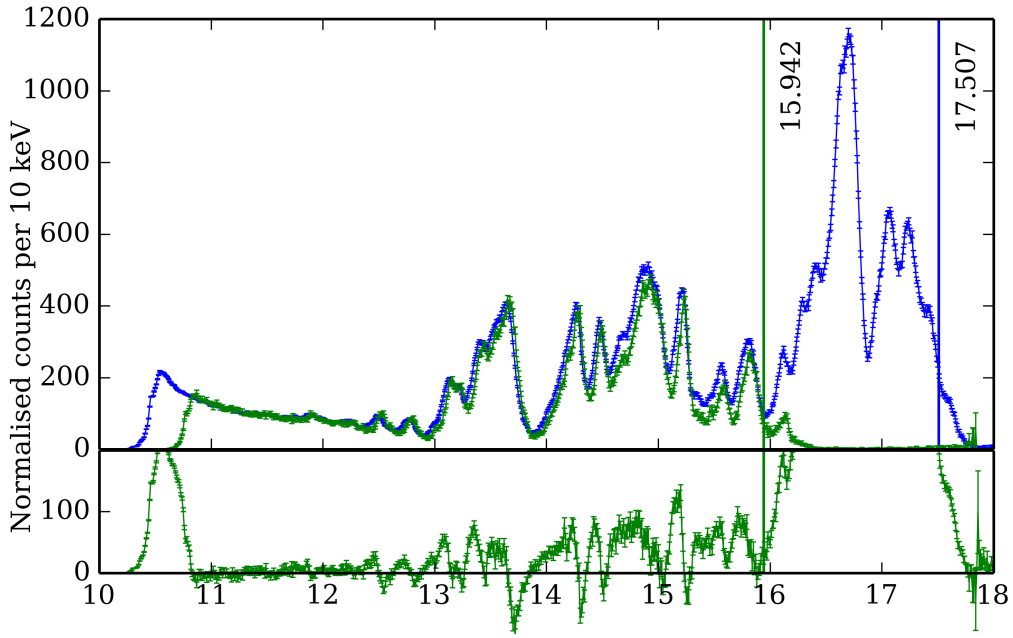

Figure 4.10: Comparison of excitation functions of ^{24}Mg measured with different beam energies. The maximum available excitation energy for each data set is indicated. The data have been normalised to each other using the Rutherford cross section between 11.0 and 11.5 MeV. The top panel shows both spectra together, and the bottom panel shows the difference between the two.

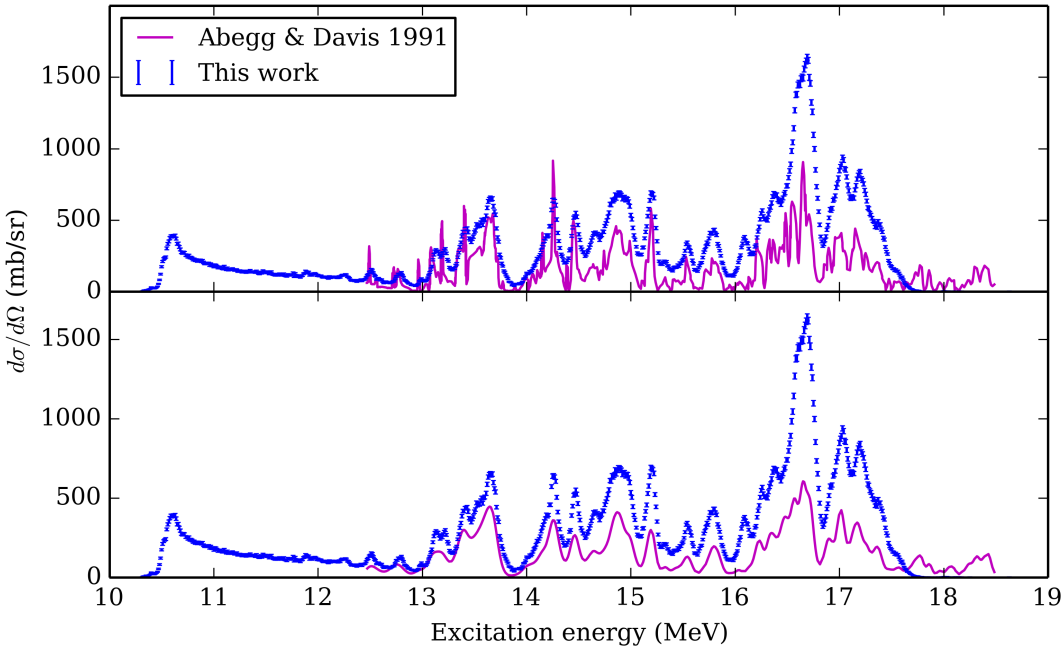

Figure 4.11: Measured excitation function of ^{24}Mg (top) compared to the thin target data of Abegg and Davis [64], measured at $\theta_{\text{c.m.}} = 168°$, and (bottom) the same comparison after the thin target data have been convoluted by a constant resolution of $\sigma = 30$ keV

rapidly changing angular distributions) are populated.

The two spectra are constructed entirely independently, including energy calibration and overall normalisation, and so the agreement provides a strong indication of the reliability of the data and analysis of the current work. Despite the different angles measured, the agreement between the data sets also shows that in the current work there are no strong contaminants from decay channels other than elastic scattering, including inelastically scattered α particles or proton or ^{8}Be decay products from ^{24}Mg, which are energetically allowed. A full list of particle decay thresholds within the measured excitation energy range for ^{24}Mg is given in Tab. 4.2.

4.3.2 *R*-matrix fit

Because excitation functions measured at the same angle in Ref. [64] and the current work are not available, an improved comparison between these data can be made using an R-matrix fit. A fit was performed to a portion of the data of Abegg and Davis at

Table 4.2: Decay thresholds within the measured excitation energy region for ^{24}Mg [41].

Decay channel	Threshold (MeV)
α	9.317
p	11.693
^{12}C	13.934
^{8}Be	14.138
n	16.532

168° between 12.5 and 13.9 MeV in excitation energy using the code AZURE2 [66]. This fit is shown in Fig. 4.12. Due to the computational time required for the R-matrix fitting process, this has been done for only part of the spectrum. The resulting parameters are shown in Tab. 4.3. Since both the α and proton channels are open at these energies, it is possible for the states to have significant proton widths Γ_p. As no data were available for the proton channel, however, these widths were fixed to zero if a good fit could be obtained using $\Gamma_{\text{tot.}} = \Gamma_\alpha$. If this was not the case, then the proton width was allowed to vary in the fit. There are only two open channels in the fitted region and so $\Gamma_{\text{tot.}} = \Gamma_\alpha + \Gamma_p$, and this should give realistic results for the partial widths.

Fitting uncertainties given in Tab. 4.3 were found by varying the channel radius r_0. Since the observables should be independent of model parameters, the variation as a function of r_0 gives an indicator of the quality of the fit. The fit was performed separately with r_0 = 1.0, 1.2 and 1.4 fm, and the mean and standard deviation of the parameters from the three fits gave the values and uncertainties shown in Tab. 4.3. If the uncertainty was found to be smaller than the precision with which the parameter is stated then it is not shown. States are described as narrow if the fitted widths are smaller than the bin size in the data; for those widths that are larger than the bin size but which have an uncertainty larger than the fitted value (due to a wide variation in the result over the three fits) an upper limit is given. In the case of the partial α width, $\Gamma_\alpha/\Gamma_{\text{tot.}}$, if the uncertainty was greater than 1 then the value is not stated.

The advantage of the R-matrix fitting process is that determination of the R-matrix poles ϵ_p and reduced width amplitudes γ_{pc} allows the cross section to be calculated for

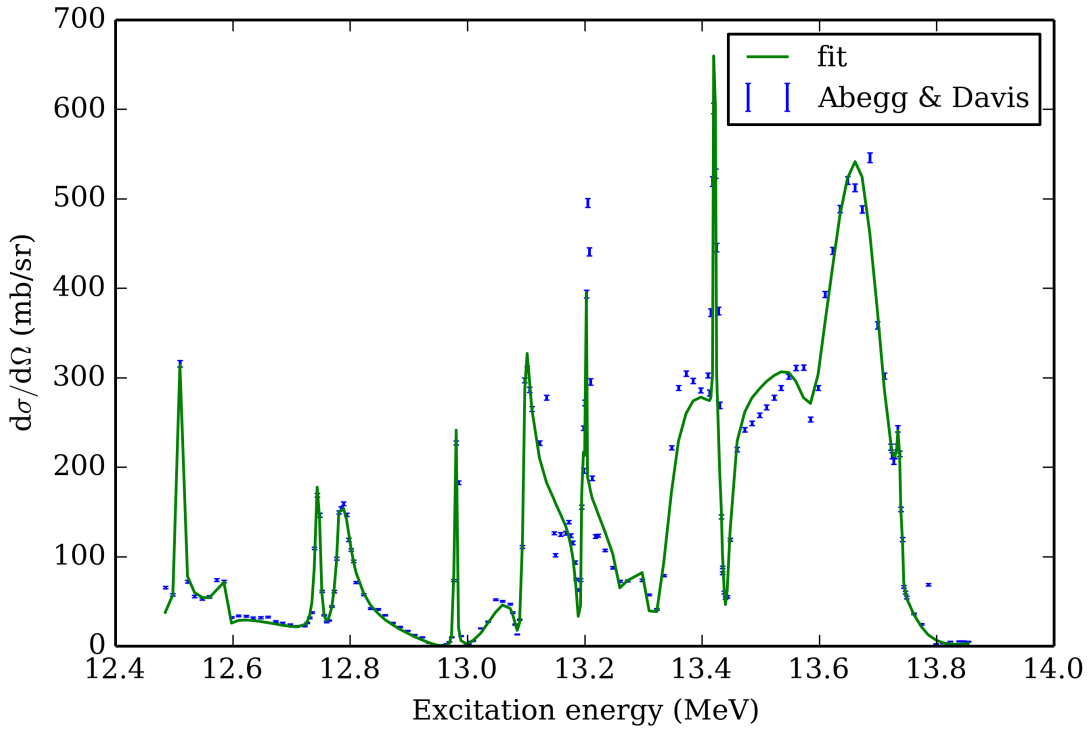

Figure 4.12: R-matrix fit (green line) to the data of Ref. [64] (blue points) using the code `AZURE2` [66]. The code was free to vary the widths for both the ^{20}Ne+α and ^{23}Na+p channels if required, although only the data shown were used in the fit.

Table 4.3: Level parameters for states in ^{24}Mg from an R-matrix fit to the data of Ref. [64] between $E_x = 12.5$ to 13.8 MeV. The fit is shown in Fig. 4.12. The proton width Γ_p was fixed to be zero unless a good fit was not possible, in which case it was allowed to freely vary.

E (MeV)	J^π	Γ_α (keV)	Γ_p (keV)	$\Gamma_\alpha/\Gamma_{\text{tot.}}$
12.507(1)	4^+	2.7(8)		1
12.583(1)	2^+	4.0(7)	0.3(2)	0.9(8)
12.745	2^+	6.6(1)	2.4(2)	0.73(5)
12.780(2)	1^-	28.6(7)	1.9(6)	0.9(3)
12.781	0^+	< 2	< 4	< 0.9
12.980	4^+	1.9		1
13.066(4)	1^-	110(60)		1
13.096	2^+	10.7(2)	3.0	0.78(2)
13.194	2^+	7.4		1
13.203	4^+	narrow	narrow	< 0.8
13.25(2)	0^+	190(160)		1
13.275	1^-	7.8(4)		1
13.348(1)	1^-	78(1)	3.3(1)	0.96(3)
13.421	4^+	1.4(1)	< 1	
13.448	1^-	32(2)	4.0(2)	0.89(7)
13.589(1)	2^+	14(4)	43(10)	0.25(9)
13.691(5)	3^-	90(60)		1
13.739	2^+	4.6(7)	< 5	
13.739	4^+	1.3(8)	narrow	

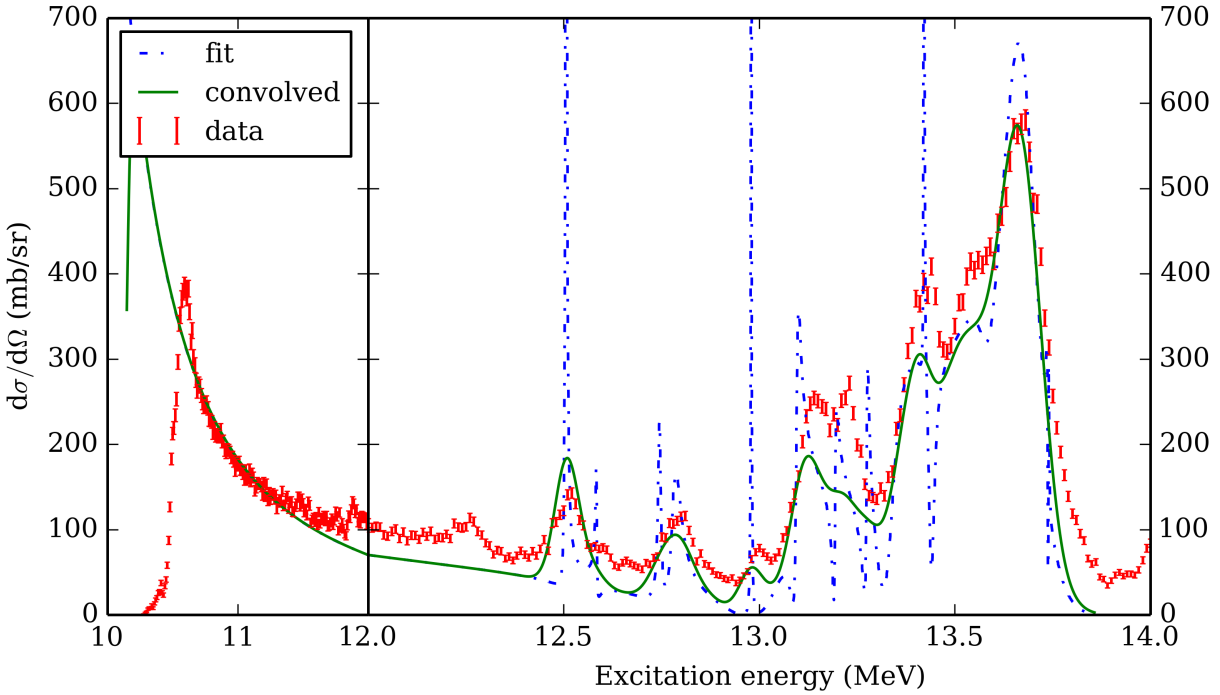

Figure 4.13: R-matrix fit to the data of Abegg and Davis [64] (shown in Fig. 4.12) extrapolated to $\theta_{\text{c.m.}} = 180°$ (blue dot-dashed line) and convolved with a resolution of $\sigma = 30$ keV (green line). The fit is compared to the data of the current work (red data points).

any energy and angle, providing that the fitted parameters are correct and complete. The fit of Fig. 4.12 was extrapolated to $\theta_{\text{c.m.}} = 180°$ in order to compare with the data of the current work, and this comparison is shown in Fig. 4.13. The agreement is generally good, although in some cases the peak heights are not reproduced. In the case of the states at 12.5 and 13.0 MeV, the number of data points in the data of Abegg and Davis for each state is very small (one and three respectively). As a result, small changes in the peak positions can result in large changes of the heights when the fit is interpolated between data points. This could also be the case for the narrow state at 13.4 MeV, although it is better defined by the data.

The fit also consistently under-reproduces the cross section between 13.1 and 13.7 MeV. This could be attributed to inelastic contaminants or other reaction channels in the data of the current work, as these could not be separated at these energies.

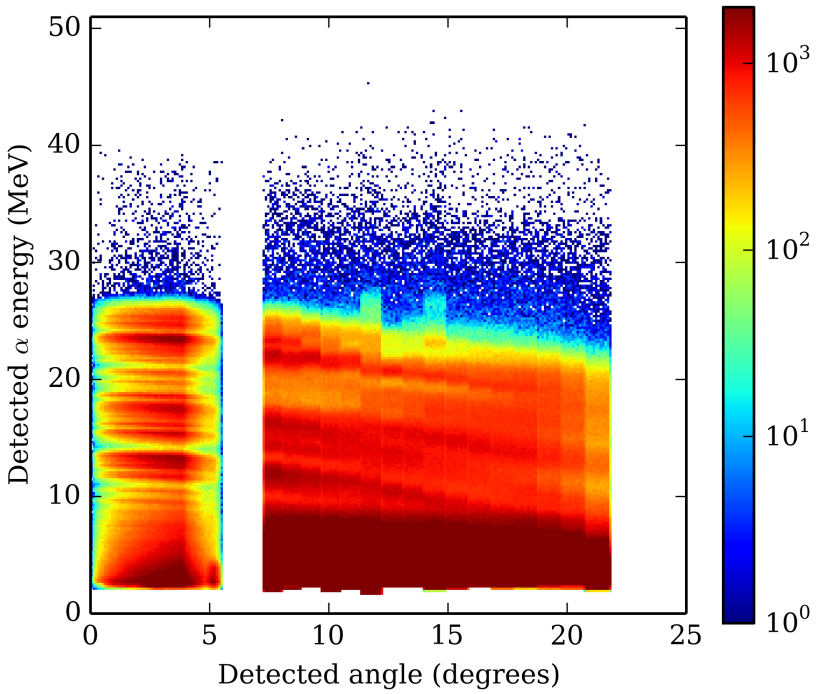

Figure 4.14: Two-dimensional energy-angle histogram for ^{24}Mg, showing data from both the zero-degree detector and the lampshade array. Angle is given in the laboratory frame as measured from the entrance window.

4.3.3 Angular distributions

The data from the lampshade array are shown in Fig. 4.14 alongside the data from the zero-degree detector now plotted also as a function of angle. The angle given is measured in the laboratory frame with the coordinate origin placed at the entrance window. The change in resolution as a function of angle can be seen, and so the matching of states with angular distributions cannot be done on a state-by-state basis. Instead, an analysis was used to find the strength of each partial wave $\ell = 0$–7 as a function of excitation energy in order to provide an indication of the number of states in each part of the excitation function that have each spin.

In order to simplify the analysis of the angular distributions, is was assumed that when the distributions of different states overlap in energy they interfere constructively. In the c.m. frame, the angular distribution for a state with a given spin depends on the Legendre polynomial $P_\ell(\cos\theta_{\text{c.m.}})$; in the laboratory frame the count rate as a function

of angle $f_\ell(\theta_{\rm lab})$ also depends on the geometry of the detectors and the c.m. velocity. In general the $f_\ell(\theta_{\rm lab})$ can be determined using a simulation as described in section 4.2.2. The measured distribution, $F(\theta_{\rm lab})$, at a given energy is then a weighted sum of the possible distributions for each spin, i.e.

$$F(\theta_{\rm lab}) = A\sum_{\ell=0}^{7} c_\ell f_\ell(\theta_{\rm lab}) \tag{4.2}$$

where the weights, c_ℓ, depend on the number and strength of states of spin ℓ in this energy region and the amplitude A is varied to give an overall normalisation. The c_ℓ were allowed to vary from 0 to 10 in integer steps, and the best fit was determined using a standard χ^2 test after a complete search of the parameter space. The results of this fitting process are shown in Fig. 4.15, where the fractional contribution for each spin is defined as

$$C_\ell = \frac{c_\ell}{\sum_{\ell=0}^{7} c_\ell}. \tag{4.3}$$

This optimisation was repeated throughout the excitation energy range measured, using gates that were hand drawn with widths of approximately 400 keV. While the kinematic dependence of the angular distribution of each state is a curve that also depends on energy, as shown in the simulations of Fig. 4.3, the gates used for this analysis were drawn using a linear approximation to this. The grey region in Fig. 4.15 indicates the Gamow energy range for ^{12}C+^{12}C burning which is of interest in astrophysics [67]. The uncertainty on the results of this analysis can be characterised by the variation in the data points and is approximately 10%. The validity of the method can also be evaluated by comparison to the spin assignments made by Abegg and Davis, which are summarised in Fig. 4.16 where all of the spin assignments made are shown as a function of energy, with firm and tentative assignments shown separately. In order to illustrate the distribution of states for which no assignment could be made, these states are shown as a function of energy in the top panel, where now states marked as tentative are those where the existence of the state is not definite.

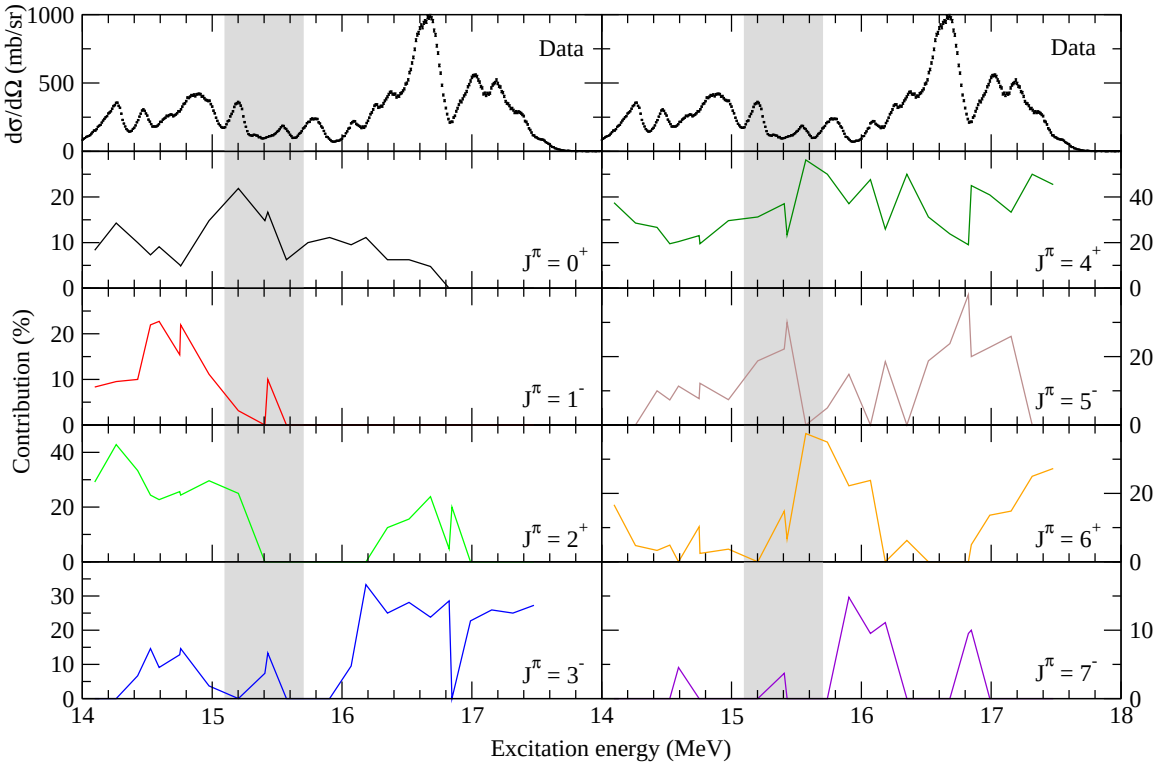

Figure 4.15: Contribution of each partial wave as a function of excitation energy in ^{24}Mg, as determined by the spin fitting procedure detailed in the text. The uncertainty on each data point is approximately ±10%. The grey background indicates the Gamow region for ^{12}C+^{12}C burning.

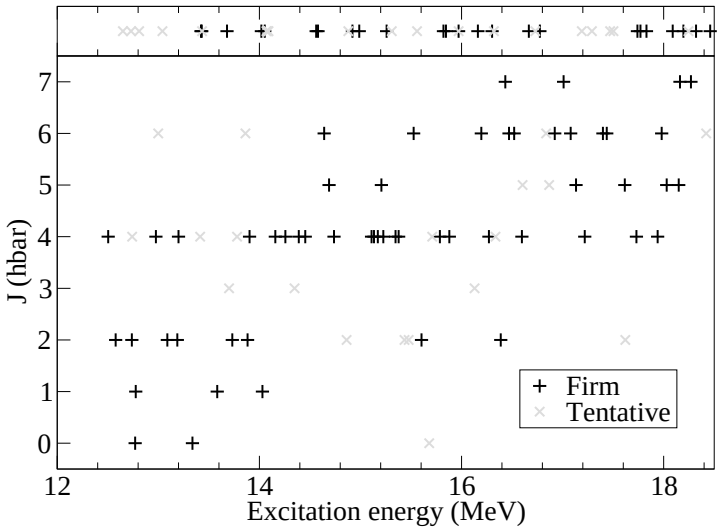

Figure 4.16: Spins of states in ^{24}Mg as a function of energy as reported in Ref. [64] showing states with both firm (black plusses) and tentative (grey crosses) assignments. States with no spin assignment are included in the top panel; here firm and tentative refer to the confidence the authors had in the identification of a state at these energies.

A comparison of the results using the fitting process outlined above and those of Abegg and Davis shows that there may be some agreement. The trend of increasing spin with increasing energy is shown in both analyses, as well as the clear dominance of 4^+ states throughout the measured region. However it is still not possible to make spin assignments with a better precision than the energy resolution allows, and it would be desirable to reduce the uncertainties in the stated contribution. In order to do this, better results could be obtained with gates that follow the real kinematic dependence of the angular distributions.

Chapter 5

Magnesium-28

The first steps of the analysis of the data for ^{28}Mg, including transforming the data into the c.m. frame and normalisation of the measured cross section, was performed in a manner identical to that for ^{24}Mg as described in Chapter 4. The results for ^{28}Mg are discussed below.

5.1 Results

A comparison of efficiency correction methods for ^{28}Mg is shown in Fig. 5.1, and it can be seen that the Monte-Carlo method is preferred due to the lower statistical uncertainties, and the absence of any improvement of the spectrum using the event rejection method. Unless otherwise stated the Monte-Carlo corrected excitation function is used in the rest of this thesis for the ^{28}Mg data. Also shown in Fig. 5.1 are the calculated Rutherford cross sections relevant to each spectrum. Normalisation to Rutherford has been performed between 15.0 and 15.5 MeV.

For ^{28}Mg, measurements were performed at four different beam energies (as detailed in Tab. 4.1), and the spectra obtained are shown in Fig. 5.2 where the lower panel of the figure shows the differences between each spectrum and the data taken with the highest beam energy. Due to the much shorter run time for the lower beam energies compared to the highest energy data, the statistical uncertainties are larger, and so the data are

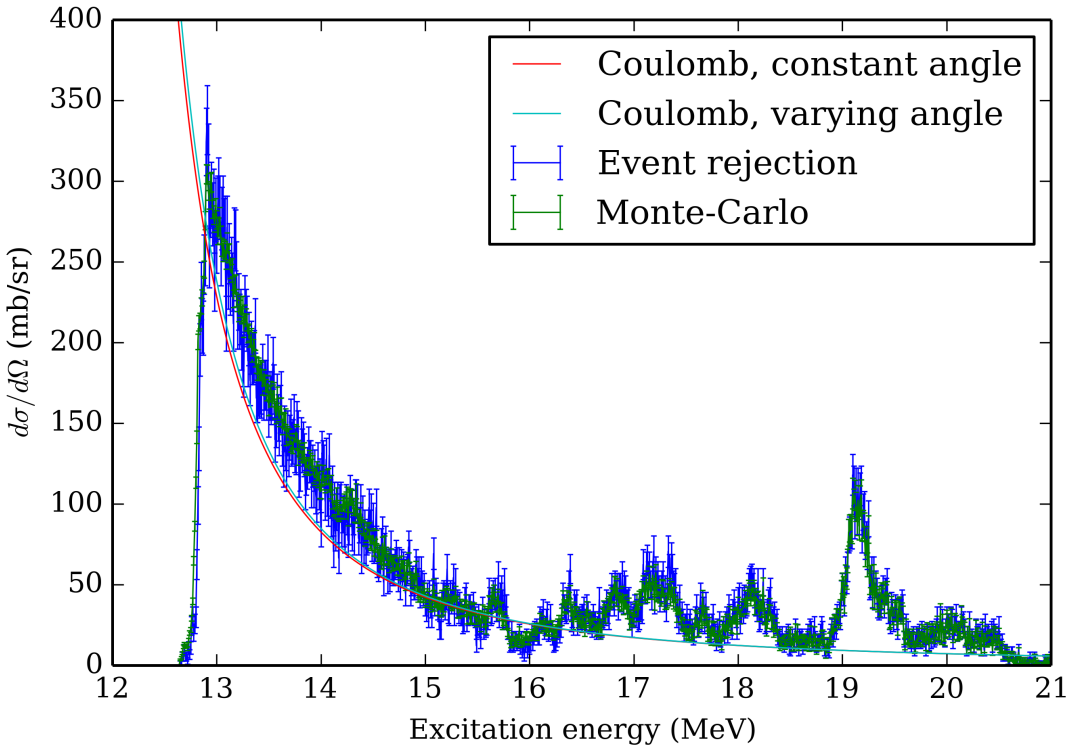

Figure 5.1: Comparison of efficiency correction methods for the excitation function of ^{28}Mg, both normalised to the Rutherford cross section calculated with a constant angle (for the event rejection method) or a varying angle (for the Monte-Carlo method). No improvement in peak shape is seen for the event rejection method, while the Monte-Carlo correction provides much better uncertainties for this low-statistics measurement.

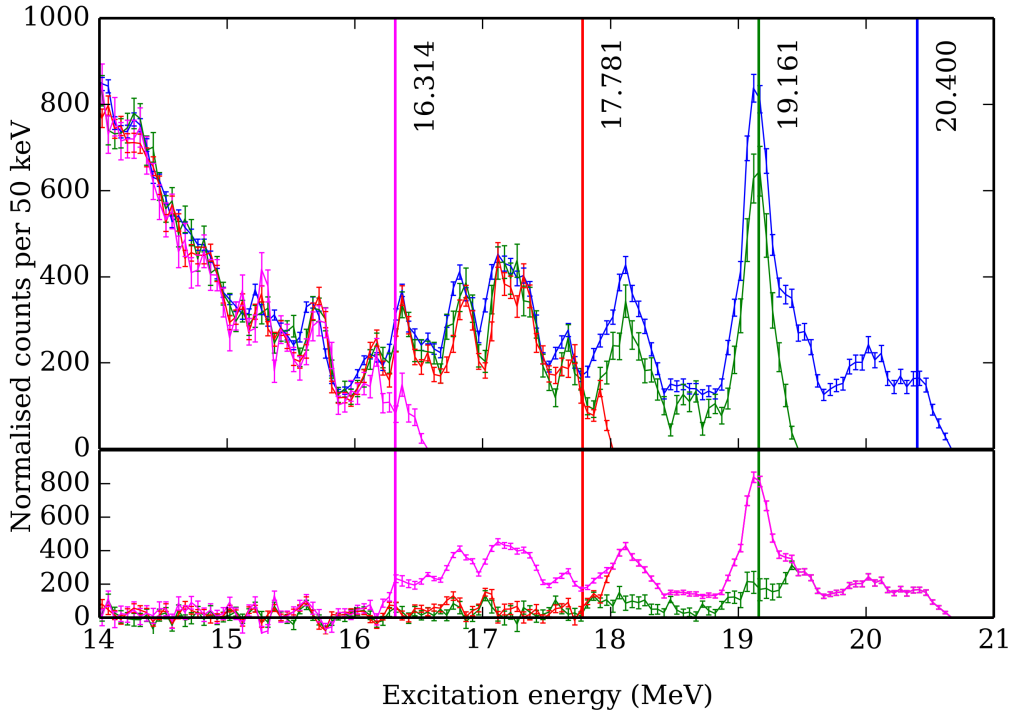

Figure 5.2: Comparison of excitation functions for ^{28}Mg with different beam energies. For each data set, the maximum available excitation energy is marked. The upper panel shows the four spectra where the data are normalised to each other using the Rutherford cross section between 13.1 and 14.0 MeV. The lower panel shows the differences between each of the lower beam energy spectra (green, red, magenta) and the spectrum with the highest beam energy (blue).

shown with 50 keV bins. Relative normalisation of these data was performed using the Rutherford cross section between 13.1 and 14.0 MeV. The maximum excitation energies allowed with each beam energy are marked in Fig. 5.2, and as the first excited state of ^{24}Ne is at 2.0 MeV, it can be seen that there are no significant contributions from inelastic contaminants above 14.5 MeV, which includes all of the features of interest in the measured spectrum.

Small differences between the spectra can be seen, particularly on the low energy side of the peaks, due to the change in position in the chamber of each state with beam energy, as described for ^{24}Mg in section 4.3.

A direct comparison of the magnitude of the measured cross sections for ^{24}Mg and ^{28}Mg is shown in Fig. 5.3, where the excitation functions for each nucleus are plotted as

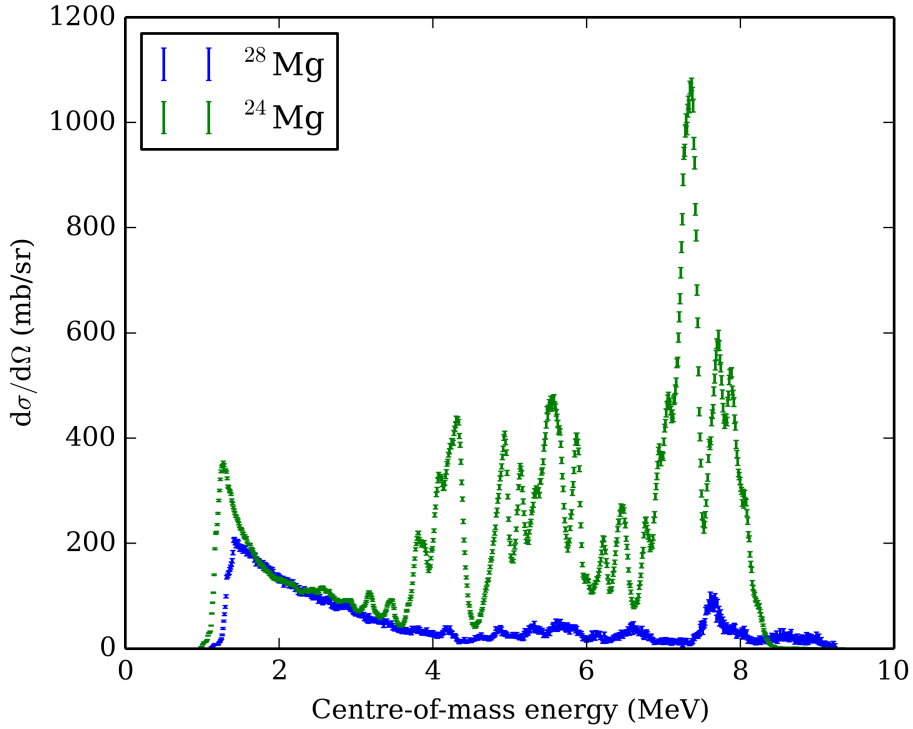

Figure 5.3: Comparison of excitation functions for ^{24}Mg and ^{28}Mg, normalised using the Rutherford cross section.

a function of the c.m. energy, and normalised to each other using the Rutherford cross section. The elastic scattering cross section is much smaller for ^{28}Mg compared to ^{24}Mg, which indicates in the first approximation that the α particle structure is weaker.

A more detailed view of the measured excitation function for ^{28}Mg is shown in Fig. 5.4 for the entire measured excitation energy region, with the calculated Rutherford cross section that was used for normalisation shown for comparison. A large amount of structure is clearly seen between $E_x = 15$ and $E_x = 21$ MeV, a region that has not been studied before. Preliminary characterisation of these states was performed using a series of fitted Gaussian peak shapes, sitting on top of the Rutherford background. This fit is also shown in Fig. 5.4; between $E_x = 16.24$ and 20.56 MeV the χ^2/d.o.f. was 2.3.

The fit shown in Fig. 5.4 was performed using a spectrum normalised to the Rutherford cross section between 15.0 and 15.5 MeV. This normalisation could, however, have been performed in other regions and the fitted parameters depend strongly on the background level. In order to quantify this dependence, the spectrum was also normalised to the least

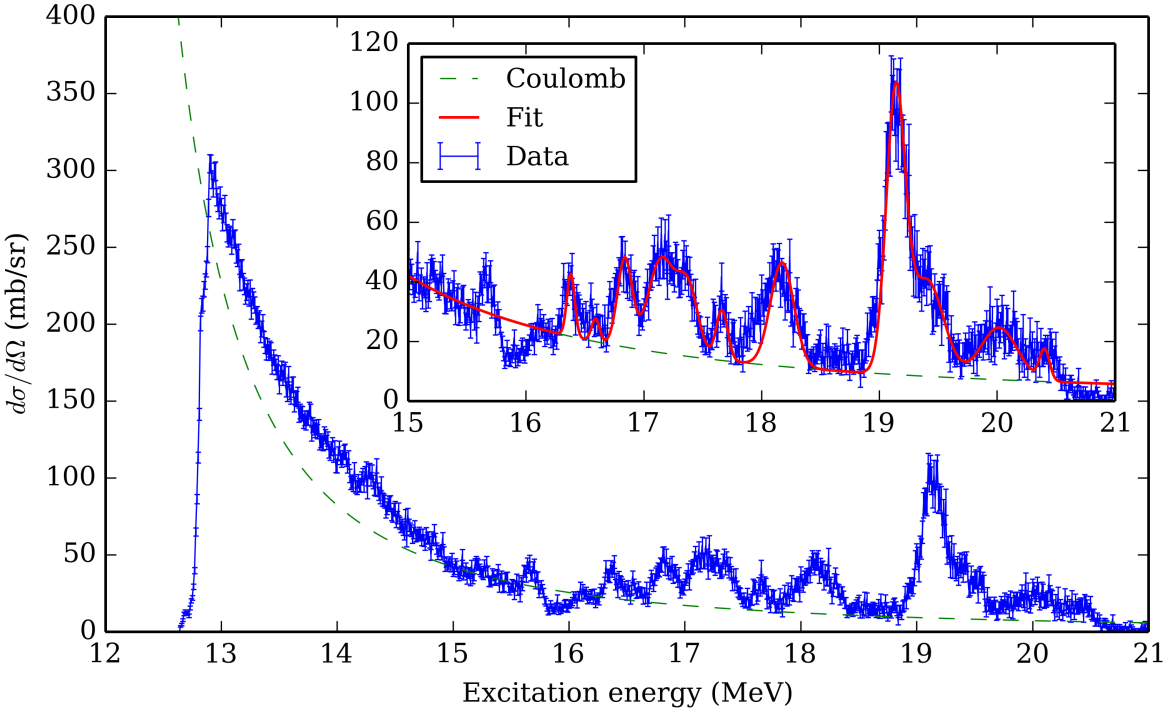

Figure 5.4: Measured excitation function for ^{28}Mg after correcting for efficiency. The calculated Rutherford cross section at $\theta_{\text{c.m.}} = 180°$ used for overall normalisation is shown. The inset shows detail of the resonances and a fit made using a sum of Gaussian peaks on top of the Rutherford background.

Table 5.1: Fitted parameters for states in ^{28}Mg using Gaussian peak shapes with a Rutherford background. Relative strength gives the area of each state as a fraction of the 19.14 MeV state.

Energy (MeV)	FWHM (keV)	Area (mb/sr)	Relative strength
15.664(5)	70(60)	—	< 0.2
16.136	100	—	< 0.1
16.377(7)	120(80)	—	< 0.3
16.55(5)	120(40)	150(130)	0.06(5)
16.836(5)	190(50)	790(590)	0.30(23)
17.13(2)	220(40)	870(280)	0.33(11)
17.35(3)	230(30)	910(660)	0.35(25)
17.656(8)	130(30)	330(230)	0.12(9)
18.14(3)	340(100)	1500(1000)	0.59(40)
19.144(4)	230(60)	2600(1400)	1.00(52)
19.43(4)	280(70)	1070(380)	0.41(15)
20.04(2)	350(40)	920(520)	0.35(20)
20.414(8)	90(10)	170(110)	0.07(4)

intense part of the spectrum between 15.8 and 16.0 MeV (resulting in the highest cross sections) and the high intensity region of the Coulomb curve between 13.5 and 15.0 MeV (resulting in the lowest cross sections). The fit was repeated with each of these background levels, and the peak parameters given in Tab. 5.1 are the mean values from the three fits. The uncertainties are quantified using the standard deviation of the parameters between the fits. Some states could not be fit in all three cases if the background level was higher than the peak, and so in these cases parameters are not given.

5.2 Analysis and discussion of selected states

A description of the structure present in ^{28}Mg in the measured energy region requires identification of the spin and parity of each state. Figure 5.5 shows the data collected away from zero degrees using the lampshade array from which the angular distributions can be found. Due to the difference in resolution between the zero-degree detector and the lampshade array, the angular distributions in most cases cannot be assigned on a state-by-state basis. The only exceptions are for isolated states: in the case of the state at 19.1 MeV, the angular distribution is relatively clear because the number of other states within a few hundred keV is small, and any states that are present are much weaker. The state at 18.1 MeV is also somewhat isolated, though it is weaker relative to the other states in the spectrum and so the angular distribution may not be as clear as for the 19.1 MeV state. In order to identify the spins of these isolated states, the angular distributions were compared to simulations. Figure 5.6 shows the count rate as a function of energy and angle from REX simulations where the scattering probability was uniform in energy and the angular dependence was given by a Legendre polynomial. While in the c.m. frame the distribution depends only on the angular momentum, ℓ, it can be seen that in the laboratory frame the locations of the maxima and minima depend also on energy due to the changing position in the chamber of the scattering.

Figure 5.7 illustrates the method used to select angular distributions from the data

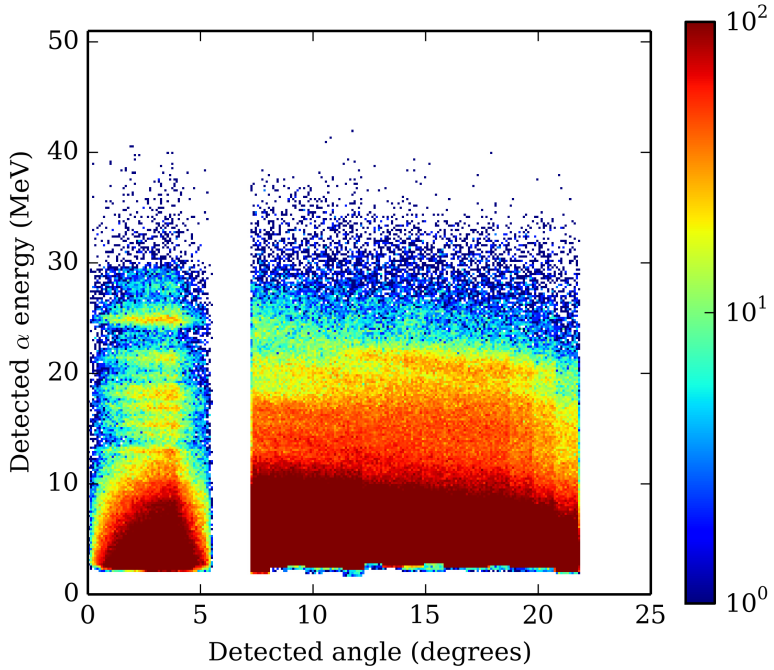

Figure 5.5: Two-dimensional energy-angle histogram for ^{28}Mg, showing data from both the zero-degree detector and the lampshade array. Angle is given in the laboratory frame as measured from the entrance window.

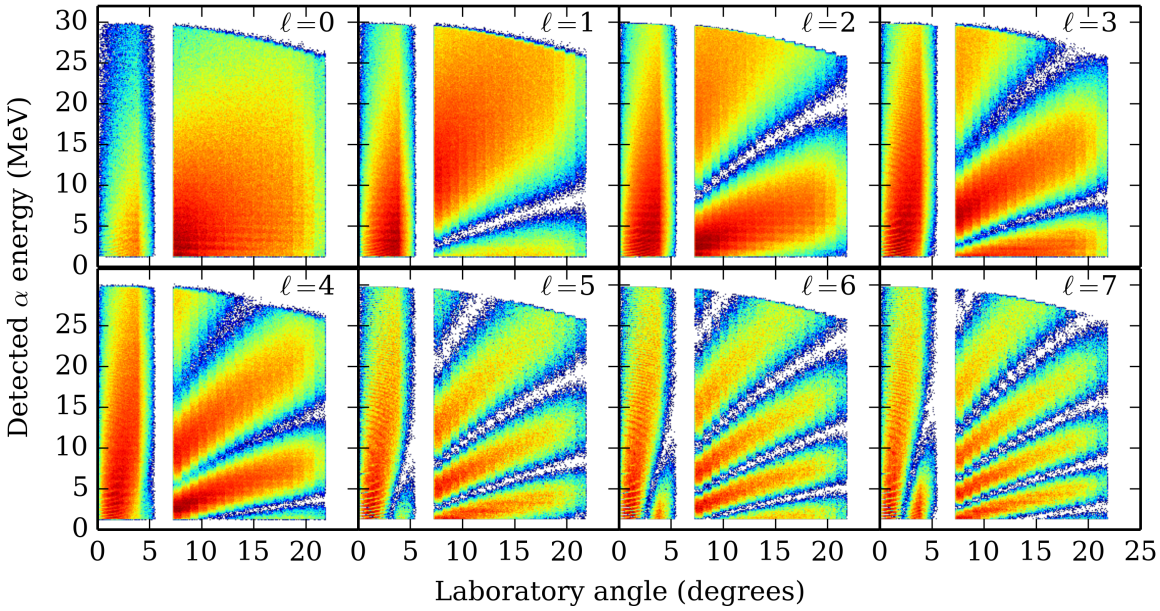

Figure 5.6: REX simulations of angular distributions for spins 0–7. In each case the energy dependence is uniform, and the angular dependence follows a Legendre polynomial of order ℓ.

of Figs. 5.5 and 5.6. The gates were generated using a REX simulation of a state in ^{28}Mg at the excitation energy of the state of interest, with a width of 1 keV, and that had a uniform angular distribution. The width was chosen to be much smaller than the experimental resolution, so that the extent of the gate depended just on the resolution. These simulations for the states at 19.1 and 18.1 MeV are shown in the left panel of Fig. 5.7. The width of the gate was tuned by applying a threshold to the simulated data: the middle panel of Fig. 5.7 shows the areas selected by applying a threshold of 10 or 150 counts per bin to the simulations in the left hand panel. The right hand panel of Fig. 5.7 shows these gates on top of the scattering data for ^{28}Mg. The same gates were applied to both the simulated and experimental data, so that all of the factors that affect the count rate are taken into account, such as the varying efficiency as a function of angle and the movement of the maxima and minima of the distributions as a function of energy. The simulations were run for sufficient events such that the statistical uncertainties were much smaller than those from the experimental data; the simulated distributions were then scaled by the total number of counts for comparison with the data. Finally, a moving average was used to remove any statistical fluctuations in the simulations, as the angular distributions are known to be smooth functions of angle.

5.2.1 19.1 MeV state

The angular distribution for the state at 19.1 MeV is shown in Fig. 5.8 where it is compared to the relevant simulations of Fig. 5.6, and there is strong agreement with the $\ell = 4$ case. There is no clear minimum in the data that can be matched with the simulations, but this is likely due to the influence of weaker nearby states. As shown in Fig. 3.6, the outermost three strips of the wedge detectors provide incomplete azimuthal coverage, and it can be seen that the count rate decreases for angles greater than 19°—though this effect is included in the REX simulations. Matching with either $\ell = 3$ or $\ell = 5$ would require a clear maximum at a smaller angle that is not present. Lower spins than those shown would require a much flatter distribution than is observed, and higher spins produce more closely

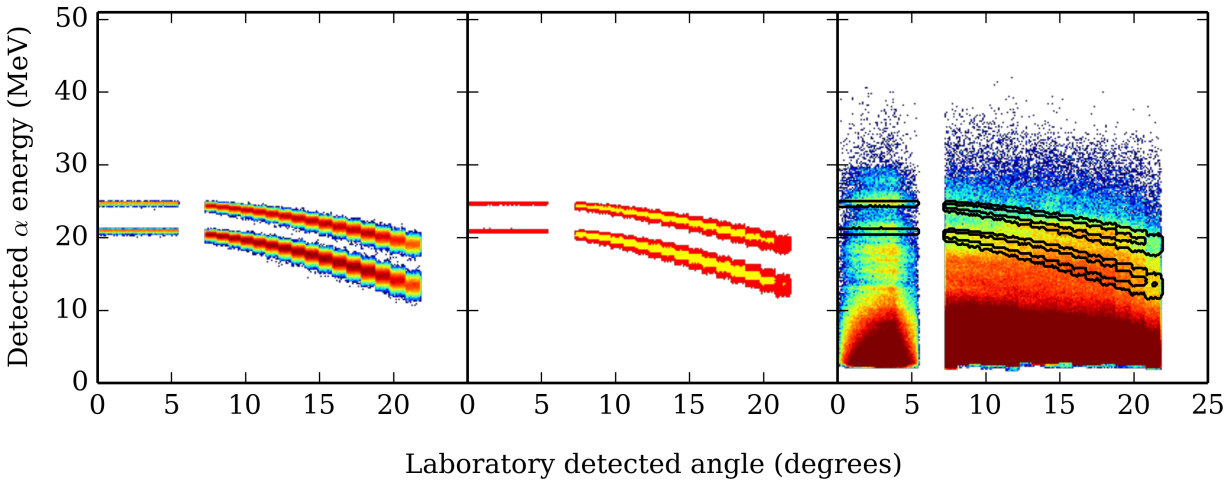

Figure 5.7: Methodology of selecting data for angular distributions using simulations. Two-dimensional histograms of energy vs. angle for (left) simulated states at $E_x = 19.1$ and 18.1 MeV and $\Gamma = 1$ keV, and (middle) the areas selected by applying thresholds of 10 counts per bin (red) and 150 counts per bin (yellow) to the simulations. The resulting gates are shown over the experimental data (right) indicating the data selected in each case.

spaced maxima, that are also not observed. The 19.1 MeV state is therefore assigned a spin-parity of $J^\pi = 4^+$.

The measured width can be an indicator of the structure of a state, but more information is needed. The nuclear elastic scattering cross section for α particles due to an isolated state, $\mathrm{d}\sigma_n/\mathrm{d}\Omega$, depends on the α decay width Γ_α, and the orbital angular momentum ℓ:

$$\frac{\mathrm{d}\sigma_n}{\mathrm{d}\Omega} \propto (2\ell+1)\frac{\Gamma_\alpha^2}{(E-E_R)^2+\Gamma_{\mathrm{tot.}}^2/4} \tag{5.1}$$

where E_R is the energy of the resonance and $\Gamma_{\mathrm{tot.}}$ is the total decay width of the state, i.e. $\Gamma_{\mathrm{tot.}} = \sum_i \Gamma_i$ for each decay channel i. For the state at 19.1 MeV the excitation function gives a measurement of the cross section and the total width, and the angular distribution gives the total angular momentum. Table 5.2 shows the decay thresholds from ^{28}Mg for all channels that are open in the measured energy range. At 19.1 MeV the open channels are neutron, proton, and α decay, although the proton decay will be strongly suppressed by the Coulomb barrier (the R-Matrix penetrability from this state is $P = 10^{-3}$, compared to $P = 2.5$ for the α channel). By assuming that $\Gamma_{\mathrm{tot.}} = \Gamma_\alpha + \Gamma_n$,

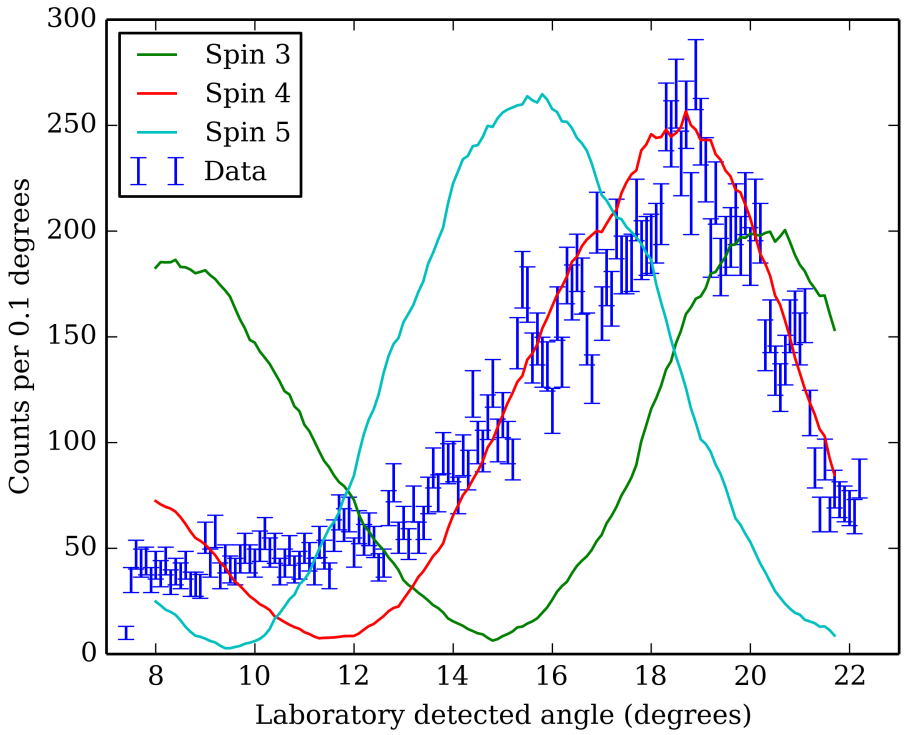

Figure 5.8: Measured angular distribution for the state at 19.14 MeV (data points) compared to simulated angular distributions of a state at this energy with $\ell = 3$–5 (lines). These data were selected using a gate threshold of 50 counts per bin (see text for details). The uncertainty in angle is determined by the strip pitch, and is approximately 1°.

Table 5.2: Decay thresholds for ^{28}Mg up to $E_x = 25$ MeV.

Decay channel	Threshold energy (MeV)
n	8.505
α	11.492
$2n$	14.947
p	16.790
$\alpha + n$	20.361
t	20.611
^{14}C	21.058
d	21.294
^{8}Be	23.758
^{6}He	24.589
$\alpha + 2n$	25.562

then the branching ratio $\Gamma_\alpha/\Gamma_{\text{tot.}}$ can be deduced from the cross section measured in the α channel.

The branching ratio was calculated using an R-matrix fit to the state at 19.1 MeV using the code `AZURE2` [66]. The input parameters defined a state at this energy with $J^\pi = 4^+$, and the fit was performed by varying Γ_α and Γ_n only. In order to remove the effect of interference with the Coulomb scattering in the calculation, the elastic scattering channel was replaced by two separate incoming and outgoing α channels, distinguished by a vanishingly small Q-value. In the experiment, the elastic scattering cross section, σ_{el}, is given by

$$\sigma_{el} \propto \frac{\Gamma_\alpha^2}{(E - E_R)^2 + \Gamma_{\text{tot.,el}}^2/4} \tag{5.2}$$

where $\Gamma_{\text{tot.,el}} = \Gamma_\alpha + \Gamma_n$, and in the calculation the inelastic scattering cross section, σ_{in}, is

$$\sigma_{in} \propto \frac{\Gamma_{\alpha 1}\Gamma_{\alpha 2}}{(E - E_R)^2 + \Gamma_{\text{tot.,in}}^2/4} \tag{5.3}$$

where now $\Gamma_{\text{tot.,in}} = \Gamma_{\alpha 1} + \Gamma_{\alpha 2} + \Gamma_n$ for the widths for the separated α channels $\Gamma_{\alpha i}$. By constraining the widths so that $\Gamma_{\alpha 1} = \Gamma_{\alpha 2} = \Gamma_\alpha/2$ then $\Gamma_{\text{tot.,el}} = \Gamma_{\text{tot.,in}}$ and it follows that

$$\sigma_{in} = \frac{\Gamma_\alpha^2/4}{(E - E_R)^2 + \Gamma_{\text{tot.}}^2/4} = \frac{\sigma_{el}}{4}. \tag{5.4}$$

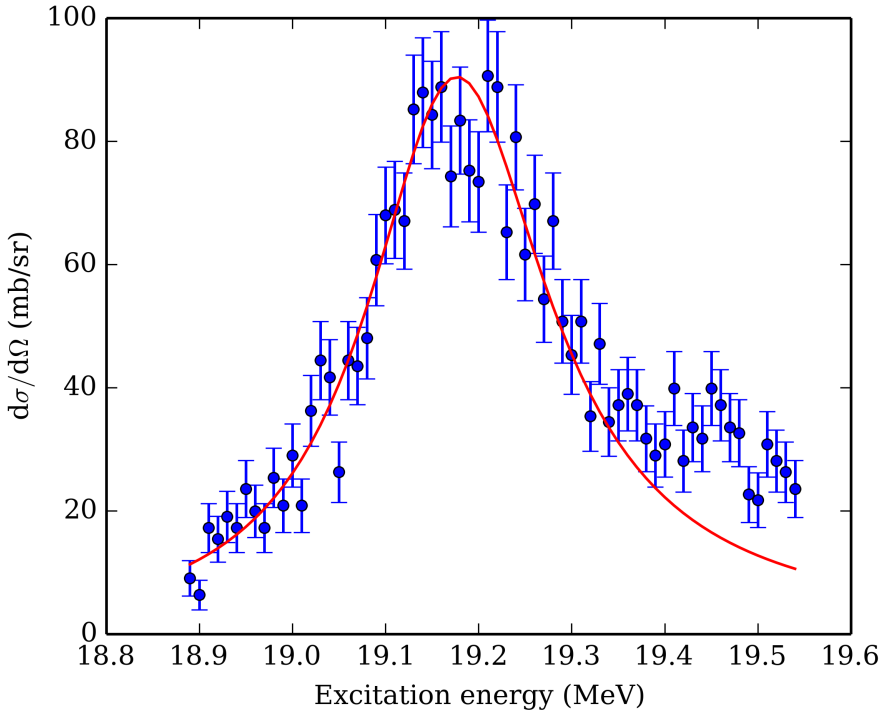

Figure 5.9: R-matrix fit to the state at 19.1 MeV using the code `AZURE2` [66]. Performed using two separate α channels separated by a Q-value of 1 keV, as well as the neutron channel. See text for details.

Therefore by scaling the measured cross section by a factor of four and fitting the spectrum with two separate α channels that are constrained to have equal widths, then the equivalent width for α elastic scattering can be found by summing the two fitted α widths.

The R-matrix fit to the state at 19.1 MeV using this method is shown in Fig. 5.9. The fit was performed between $E_x = 18.9$ and 19.4 MeV, so that the shoulder on the high energy side of the peak was ignored, and the χ^2/d.o.f. in the fitting region was 1.22. The resulting parameters were $\Gamma_\alpha = 90 \pm 10$ keV and $\Gamma_n = 150pm20$ keV, giving $\Gamma_\alpha/\Gamma_{\text{tot.}} = 0.38 \pm 0.05$.

A discussion of the structure of the measured states requires a calculation of the reduced α decay width, γ_α^2, which is related to the partial width Γ_α by the penetrability using equation 2.7. By removing this factor from the decay widths, the reduced widths provide a much better indicator of the structure present. The reduced widths can be calculated using equation 2.6, noting that they are a function of R_m which introduces an

undesirable model dependence. To mitigate this, the reduced widths are often stated as a ratio to some extremal value within the same model. The most common comparison is to the Wigner limit, γ_W^2, which is found when the probability density, $|u(r)|^2$, in the internal region is constant to be

$$\gamma_W^2 = \frac{3\hbar^2}{2\mu R_m}. \tag{5.5}$$

Calculations of penetrabilities and reduced widths were performed with an in-house code `ckin` [68], which uses the routine `WCLBES` to calculate Bessel functions from the CERN Program Libraries [69]. For the state at 19.1 MeV the ratio to Wigner of the reduced width, $\gamma_\alpha^2/\gamma_W^2$ was found to be 3.8%. Clustered states typically show values of 10–30% or higher, which suggests this state is not strongly α clustered.

Cluster structure

A better indicator than this simple calculation would be to compare the measured width and branching ratio to a cluster model. The code Gamow [70] calculates observable decay widths of states in a two-body nuclear system by solving the Schrödinger equation for the properties of the light particle under the influence of the potential generated by the heavy particle. In this case, the code considers, for example, an α particle in the potential of the ^{24}Ne core. A solution is found iteratively by ensuring that the logarithmic derivative of the wavefunction is continuous at some matching radius between the internal and external regions.

The formalism used in the Gamow code is similar to that of R-matrix theory: the compound nucleus is split into the internal and external regions for which the system wavefunction can be found separately. The boundary conditions applied to the radial wavefunction $u(r) = r\psi(r)$ are:

$$u(0) = 0 \tag{5.6}$$

and

$$u(R_m)O'_\ell(kR_m) - u'(R_m)O_\ell(kR_m) = 0 \tag{5.7}$$

where $O_\ell(kr)$ is the outgoing Coulomb wave given by the regular and irregular Coulomb functions F_ℓ and G_ℓ as

$$O_\ell = G_\ell + iF_\ell, \tag{5.8}$$

and the prime denotes the derivative with respect to r. The code varies the depth of the potential and the state energy in order to satisfy these conditions. The complex state energy, E, is given by

$$E = E_x - i\frac{\Gamma}{2} \tag{5.9}$$

so that the real part gives the resonance energy E_x and the imaginary part gives the decay width Γ. The code can solve the Schrödinger equation for an arbitrary potential, but calculations were performed with a standard Woods-Saxon shape [71], given by

$$V(r) = -\frac{V_0}{1 + \exp{(r - R)/a}} \tag{5.10}$$

where V_0 is the magnitude of the potential depth, a is the diffuseness parameter, and R is the nuclear radius given by $R = r_0 A^{1/3}$ for the radius parameter r_0 and the mass number of the core nucleus A.

The number of nodes in the internal wavefunction, n, is given for single particles by their shell model quantum numbers. For a composite particle such as an α particle, n is found using the Wildermuth condition [72]:

$$G = 2n + \ell = \sum_i g_i \tag{5.11}$$

where G is the global quantum number determined by the sum of the quantum numbers of the constituent nucleons, g_i. For an α particle this gives $G = 8$.

The choice of the potential parameters r_0 and a has the largest influence on the results. The lack of existing data for ^{28}Mg means that there are no calculations of potential parameters in the literature. In order to choose values for r_0 and a, it was assumed that the shape of the potential would not change significantly from ^{24}Mg to ^{28}Mg, so the same

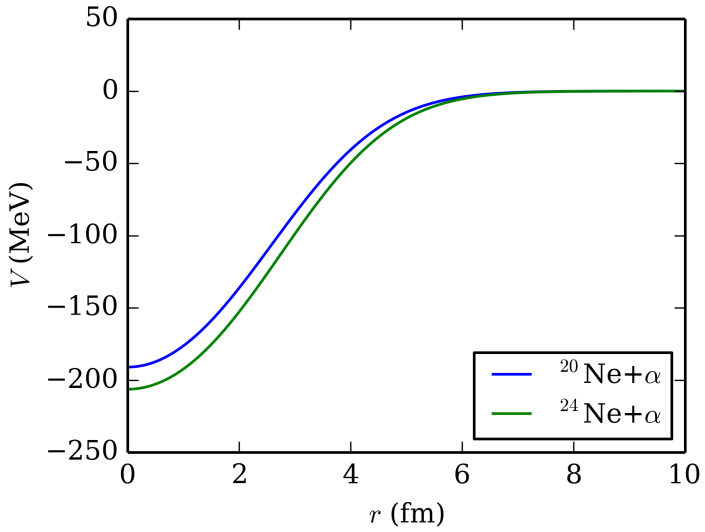

Figure 5.10: Potential for the ^{20,24}Ne+α system calculated by A. Soylu using a double folding potential.

potential parameters could be used in both cases (i.e. the radius of the potential scales only as $A^{1/3}$).

Previous theoretical studies have characterised the interaction potential of the ^{20}Ne+α system phenomenologically, by comparison to experimental data. Baktybayev *et al.* [73] analysed cross section data using the method of strongly coupled channels and found $r_0 = 1.25$ fm and $a = 0.8$ fm. Wang *et al.* [74] calculated α decay widths from ^{24}Mg with a cluster model which they then compared to experimental data, using $r_0 = 1.24$ fm and $a = 0.63$ fm.

From a microscopical approach, A. Soylu [75] calculated potential parameters for ^{24,28}Mg using a double folding model. This method, reviewed comprehensively in Ref. [76], provides a nuclear potential for the ^{20,24}Ne+α system by convolving a chosen nucleon-nucleon interaction with the densities of the cluster cores. The resulting potentials are shown in Fig. 5.10. For comparison these potentials were fitted with the standard Woods-Saxon form, giving $r_0 = 0.93$ fm and $a = 0.93$ fm for ^{24}Mg, with $r_0 = 0.93$ fm and $a = 0.94$ fm for ^{28}Mg. These potentials are narrower and more diffuse than the phenomenological potentials, but the similarity between the results for both systems does support the assumption that the potential parameters will be similar for ^{24}Mg and ^{28}Mg.

Finally, Gamow calculations for states in ^{24}Mg were used to constrain the values of the potential parameters for ^{28}Mg. By performing calculations of partial widths for states measured in this work and Ref. [64], the potential that best reproduces the experimental results could be found. The results of these calculations for 29 states in ^{24}Mg are shown in Tab. 5.3 where the radius of the potential has been fixed using $r_0 = 1.0$ fm and the value of a that best reproduces the experimental width has been found. These calculations were performed using a cosh potential shape [77], given by

$$V(r) = -V_0 \frac{1 + \cosh R/a}{\cosh R/a + \cosh r/a}, \tag{5.12}$$

which is almost identical to the Woods-Saxon shape. Calculations for selected states with both cosh and Woods-Saxon type potentials showed that the required diffuseness parameter never varied by more than 1%. For states between $E_x = 12.8$ and 18.0 MeV, the resulting values of a vary from 0.10–0.85 fm.

The resulting diffuseness parameters from Tab. 5.3 are shown in Fig. 5.11 as a function of excitation energy in ^{24}Mg, where they are coloured by the spin of the state and the width is indicated by the size of the data points. The mean value for diffuseness with $r_0 = 1.0$ fm is $a = 0.47 \pm 0.04$ fm, where the uncertainty is given by the standard error on the mean. The variation in diffuseness is quite large, however, so this method does not provide a strong constraint on the potential parameters. Calculations with different radius parameters show that there is an inverse relationship between r_0 and a: smaller radii require larger diffuseness to reproduce the experimental widths, and vice versa.

Using these constraints on the radius and diffuseness parameters, calculations can be performed using the Gamow code for the expected α and neutron widths for the measured state at 19.1 MeV. Figure 5.12 shows the calculated values of Γ_α and Γ_n as a function of r_0 and a. For the potential parameters of Wang *et al.* ($r_0 = 1.24$ fm and $a = 0.63$ fm), the calculated widths are $\Gamma_\alpha = 2.5$ MeV and $\Gamma_n = 6.0$ MeV; for those of the double folding potential ($r_0 = 0.93$ fm and $a = 0.94$ fm) the widths are larger and the code does

Table 5.3: Measured and calculated widths in ^{24}Mg.

E_x (MeV)	J^π	Γ_α (keV) measured	a (fm)	Γ_α (keV) calculated
12.78	1^-	26.4	0.261	26.43
13.1	2^+	10.3	0.205	10.27
13.2	4^+	1.28	0.43	1.23
13.7	3^-	122	0.65	122.1
14.257	4^+	16(2)	0.51	16.22
14.348	(3^-)	112(29)	0.47	112.2
14.454	4^+	46	0.606	45.89
15.172	4^+	57(7)	0.493	57.2
15.207	5^-	36(3)	0.651	36.15
15.226	4^+	27(6)	0.382	27.04
15.347	4^+	21(4)	0.317	20.96
15.378	4^+	31(7)	0.374	30.97
15.526	6^+	18(2)	0.835	18.09
15.786	4^+	13	0.18	12.94
15.879	4^+	42	0.33	41.91
16.196	6^+	8	0.64	7.95
16.271	4^+	30	0.225	30.35
16.433	7^-	10	0.846	10.03
16.447	6^+	8(2)	0.606	7.94
16.521	6^+	31	0.743	31.14
16.597	4^+	30	0.175	29.65
16.867	(5^-)	73(17)	0.492	72.84
16.922	6^+	44(6)	0.724	44.07
17.01	7^-	15(10)	0.807	14.94
17.08	6^+	44(6)	0.704	44.23
17.133	5^-	26(6)	0.338	26.2
17.615	5^-	23(8)	0.264	23.04
17.94	4^+	56(8)	0.095	56.07
18.03	5^-	50(8)	0.317	49.91

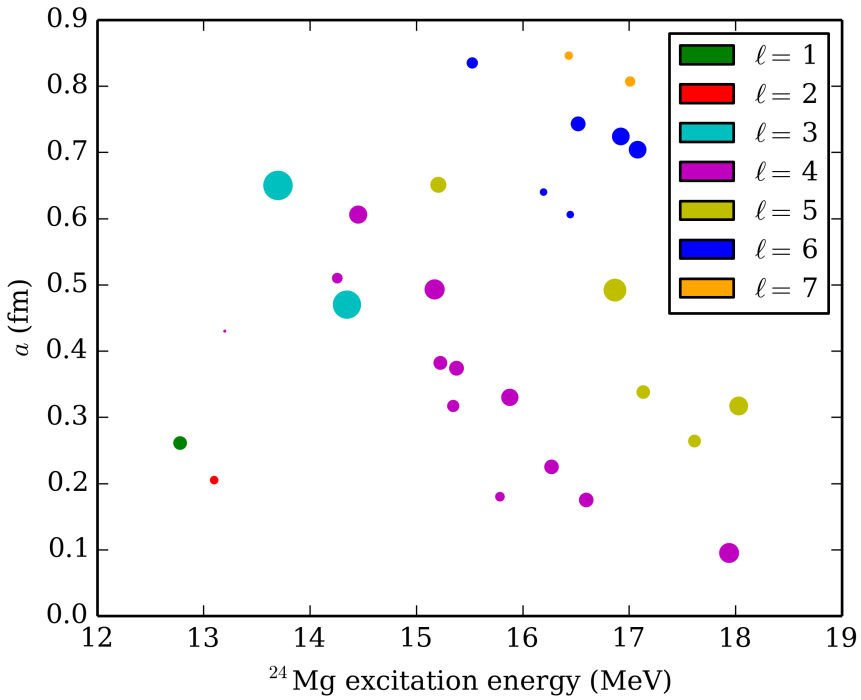

Figure 5.11: Diffuseness parameter, a, required to reproduce experimental widths of states in ^{24}Mg with the Gamow code [70] using a standard Woods-Saxon potential with $r_0 = 1.0$ fm. Colour indicates the spin of the state, and the area of each data point is proportional to the width.

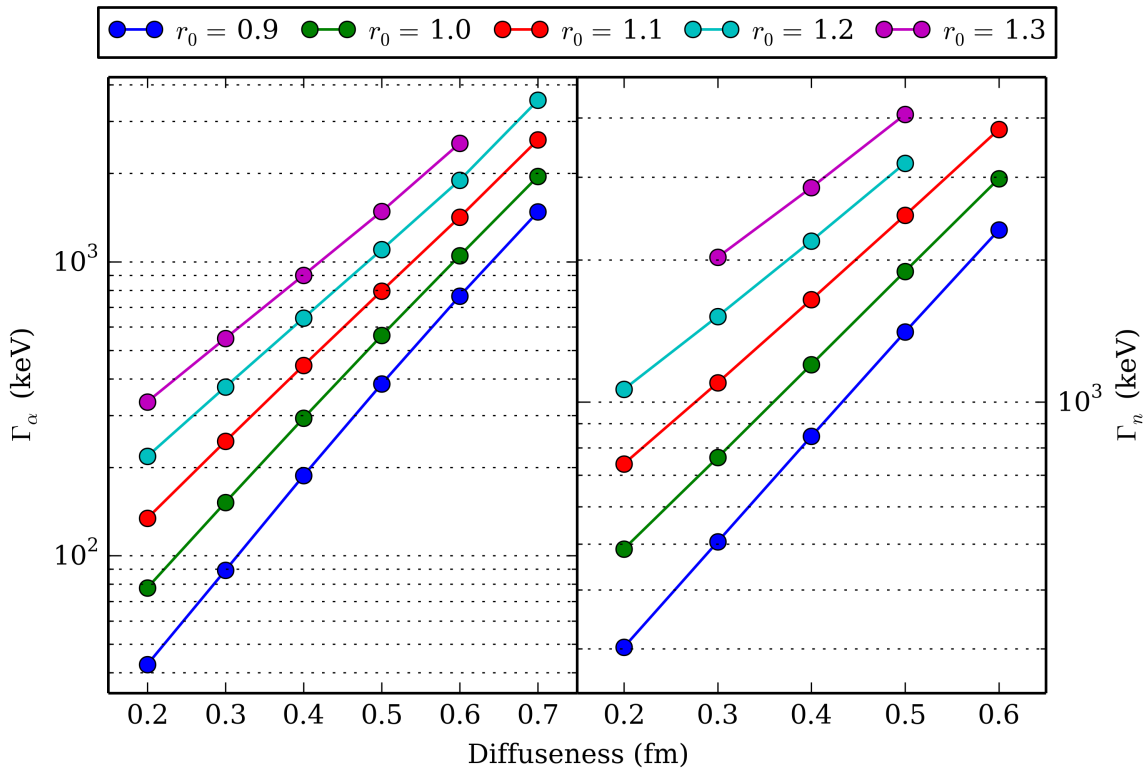

Figure 5.12: Calculated decay widths for (left) ^{24}Ne+α and (right) ^{27}Mg+n, as a function of radius and diffuseness parameters.

not converge. A lower limit is found by reducing the diffuseness to 0.8 fm, which gives $\Gamma_\alpha = 3.3$ MeV and $\Gamma_n = 6.9$ MeV. The same approach is required for the parameters of Baktybayev *et al.*, where convergence is acheived for $r_0 = 1.1$ fm and $a = 0.7$ fm, giving $\Gamma_\alpha = 2.6$ MeV and $\Gamma_n = 6.0$ MeV. Finally, the mean potential parameters found to reproduce experimental widths in ^{24}Mg ($r_0 = 1.0$ fm and $a = 0.47$ fm) give $\Gamma_\alpha = 460$ keV and $\Gamma_n = 1650$ keV.

These calculations, summarised in Tab. 5.4, give consistently larger widths that those calculated from the data ($\Gamma_\alpha = 90$ keV, $\Gamma_n = 150$ keV). This suggests that the state at 19.1 MeV is not strongly α clustered, which is in agreement with the comparison to the Wigner limit. In the case of the neutron channel, however, the calculated widths are also much larger than those measured, so it is not yet clear what structure this state represents.

The discrepancy between the calculated and measured decay widths could be caused by a number of factors. If the interaction potential used in the calculations is poorly

Table 5.4: Decay widths for α and neutron channels from ^{28}Mg calculated using the Gamow code, with the values found from an R-matrix fit to the data shown for comparison. Dashes indicate that the Gamow calculation did not converge for the stated parameters. In these cases, similar parameter sets for which convergence was obtained are shown.

Method used	Potential parameters (fm)		Widths (keV)		Branching ratio
	r_0	a	Γ_α	Γ_n	$\Gamma_\alpha/\Gamma_{\text{tot.}}$
R-matrix fit to data	–	–	90	150	0.375
Baktybayev *et al.* [73]	1.25	0.80	–	–	–
	1.10	0.70	2600	6000	0.302
Wang *et al.* [74]	1.24	0.63	2500	6000	0.294
Double folding potential [75]	0.93	0.94	–	–	–
	0.93	0.80	3300	6900	0.324
States in ^{24}Mg	1.00	0.47	460	1650	0.218

chosen, then the results will not be reliable. In particular, the calculations performed (both with the Gamow code and the R-matrix approach) assume a spherical potential. AMD calculations for ^{24}Ne [78] have, however, suggested that this nucleus is prolate deformed in its ground state with deformation parameters for protons and neutrons of $\beta_p = 0.3$ and $\beta_n = 0.2$, both of which indicate significantly deformed shapes.

It is also possible that the strength of this state lies in another reaction channel that has not been considered. As shown in Tab. 5.2, other mass partitions are unlikely as they are either strongly inhibited (in the case of the proton channel) or below threshold; it would not be expected for these levels to dominate over the unbound α and neutron channels. Inelastic scattering is possible, as although it is possible in this work to show that inelastic contaminants in the measured excitation spectrum are small this does not constitute a measurement of the inelastic scattering cross section. While this would be expected to be non-zero, it is still not clear why it would dominate over elastic scattering.

Further work that would help to clarify the structure present in this state is discussed in the following chapter.

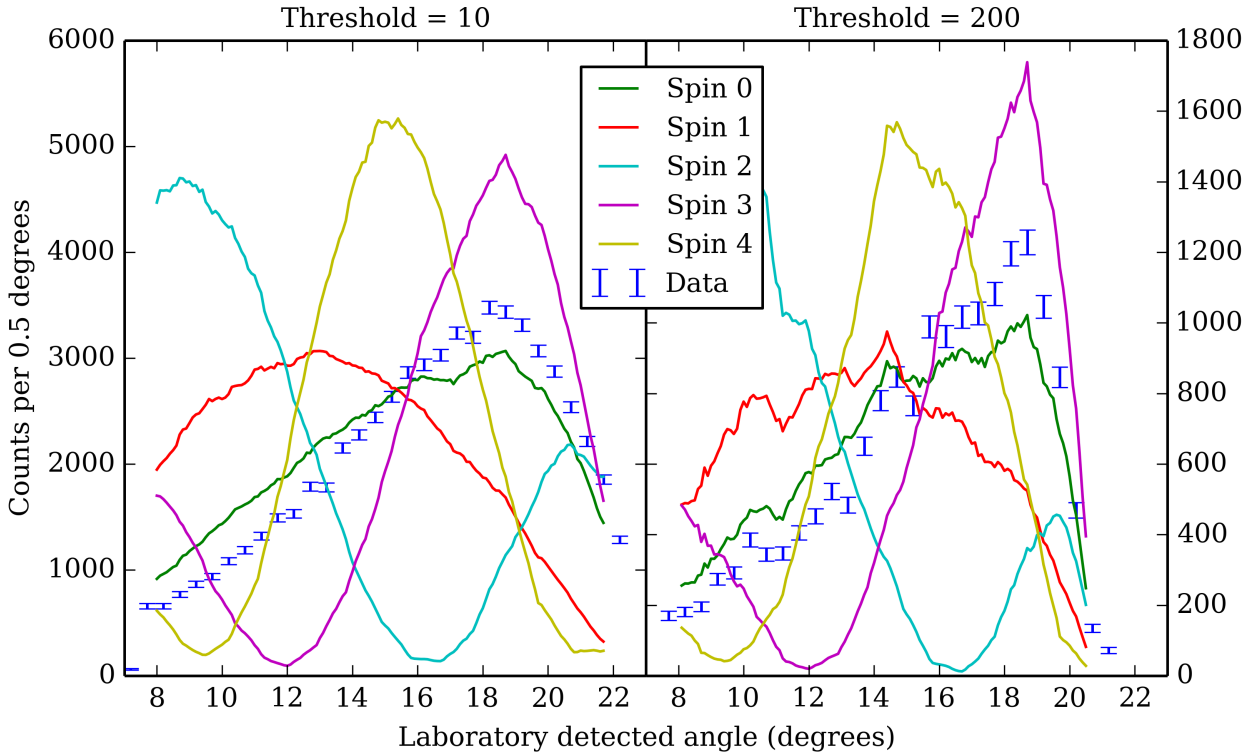

Figure 5.13: Measured angular distribution for the state at 18.14 MeV (data points) compared to simulated angular distributions of a state at this energy with $\ell = 0$–4. These data were selected using a wide gate (left, threshold = 10 counts per bin) and a narrow gate (threshold = 200 counts per bin).

5.2.2 18.1 MeV state

The angular distribution for the state at 18.1 MeV is shown in Fig. 5.13 with a range of simulated distributions. The agreement is not as clear as for the state at 19.1 MeV, and so the distributions with two different gates are shown. The first gate uses a low threshold of 10 counts per bin, so that the distribution is selected from almost the full extent of the simulated distribution giving a distribution that agrees best with the $\ell = 0$ case. A flat distribution could, however, also result from the mixing of different distributions from nearby states. In order to isolate the contribution from the 18.1 MeV state, a narrow gate was created using a threshold of 200 counts per bin, and the resulting distributions are shown in the right hand panel of Fig. 5.13.

The narrower gate appears to enhance the peaked nature of the distribution, so that a maximum may be present that would agree with the location of the maximum for a 3^-

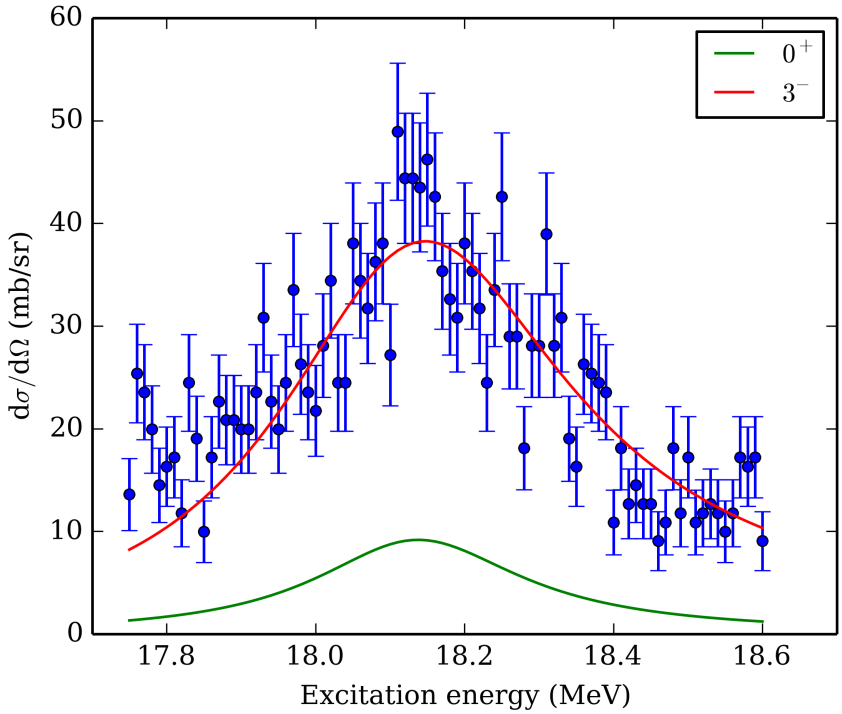

Figure 5.14: R-matrix calculations of a state at 18.1 MeV showing (green) $J^\pi = 0^+$ with $\Gamma_\alpha = \Gamma_{\text{tot.}} = 340$ keV and (red) $J^\pi = 3^-$ with $\Gamma_\alpha = 140$ keV and $\Gamma_\alpha/\Gamma_{\text{tot.}} = 0.29$.

state. At smaller angles, however, the distribution still follows the 0^+ simulation, i.e. flat in the c.m. frame. In order to determine if the observed cross section can be explained by a single 0^+ state, an R-matrix calculation was performed for a state at 18.1 MeV with the measured total width $\Gamma_{\text{tot.}} = 340$ keV, and the maximum possible cross section which occurs when the branching ratio to α decay $\Gamma_\alpha/\Gamma_{\text{tot.}} = 100\%$.

The fit was performed using the same two-channel method as described for the 19.1 MeV state in section 5.2.1, and is shown in Fig. 5.14. Clearly a single 0^+ state cannot reproduce the observed cross section, so there must either be a single state present with a higher spin or there are multiple states in this region that cannot be resolved due to the experimental resolution.

If a single state is present, then the best interpretation of the angular distribution leads to the assignment of 3^- for this state. If multiple states are present, the lack of a clear spin assignment from the angular distribution suggests that spins of states in this region are mixed. An R-matrix calculation for a single 3^- state is also shown in Fig. 5.14, for

which the branching ratio has been varied to find the best fit. The parameters obtained were $\Gamma_\alpha = 140 \pm 20$ keV and $\Gamma_\alpha/\Gamma_{\text{tot.}} = 0.29 \pm 0.07$, again assuming $\Gamma_{\text{tot.}} = \Gamma_\alpha + \Gamma_n$, giving a χ^2/d.o.f. of 1.72 between $E_x = 17.8$ and 18.6 MeV.

A comparison to the Wigner limit in the same way as for the 19.1 MeV state for a single 3^- resonance with the parameters obtained above gives $\gamma_\alpha^2/\gamma_W^2 = 6.0\%$, again suggesting that it is not a strongly clustered state.

5.3 Implications for clustering

First indications for the structure in ^{28}Mg suggest that clustering is not prominent. Both of the states that have been characterised appear to have a weak α-particle component, and it is clear that if any α-clustered states did exist in this energy region they would have been observed in this experiment. It should be noted that the thresholds for the ^{23}Ne+n+α and ^{22}Ne+2n+α structures are at 20.4 and 25.6 MeV respectively, so the first molecular structures would be expected close to these energies. If strong cluster structures are observed above these thresholds in future experiments, this would be a strong indicator of the influence of molecular orbitals.

Chapter 6

Conclusions

The first results of the particle spectroscopy of ^{28}Mg have been reported. Despite the lack of previous data with which to compare the current work, confidence in the results is given by the use of the same experimental set-up to measure the excitation function of the well-studied ^{24}Mg with excellent agreement to previous data. Thirteen new states in ^{28}Mg are reported between $E_x = 15.5$ and 20.5 MeV, and preliminary characterisation of strengths and widths is given. For one state with $E_x = 19.14$ MeV a spin-parity assignment of $J^\pi = 4^+$ is given, and for a second feature at $E_x = 18.14$ MeV a tentative assignment of $J^\pi = 3^-$ is made. For both states with spin-parity assignments, calculations of the branching ratios are possible; these are found to be $\Gamma_\alpha/\Gamma_{\text{tot.}} = 0.38 \pm 0.05$ and 0.29 ± 0.07 for α-decay widths of $\Gamma_\alpha = 90 \pm 10$ keV and 140 ± 20 keV respectively.

In addition to branching ratios, a first indication of the level of α clustering present is given by comparison of the reduced width to the Wigner limit. For the states at 19.1 and 18.1 MeV this gives $\gamma^2_\alpha/\gamma^2_W = 3.8\%$ and 6.0% respectively, suggesting that in both cases α clustering is weak. For the state at 19.1 MeV, further calculations using a simple α-cluster model (the Gamow code) support the result that the measured α-decay width is much smaller than would be expected for a pure ^{24}Ne+α system. Curiously, this effect is also seen for the neutron channel, where the model of ^{27}Mg+n greatly over-estimates the measured neutron decay width of $\Gamma_n = 150$ keV. It is not yet clear what structure is

present in the measured state, and further work is required.

6.1 Future work

Nuclei that have well understood structures are those where a clear picture exits of both experimental and theoretical work. Agreement between these two approaches allows measured energy levels to be matched with calculations of density distributions and an understanding of the nuclear dynamics can be reached. In order to move towards this for ^{28}Mg additional experimental data, as well as initial theoretical work, is required.

6.1.1 Experiments

In order to build a clearer experimental picture, new data should be taken with a focus on improving the energy resolution of the measurements. The experiment of the current work was designed to maximise efficiency, as it was not known what cross section would be measured. In order to characterise the spins of a greater number of states—particularly those that are close to each other in energy—a resolution of better than 100 keV FWHM is required.

Optimisation of the experimental resolution is described in detail in Ref. [56], and is achieved by using Mylar instead of Havar for the chamber entrance window. This would reduce the angular straggling of the beam, which is the dominant contribution to the resolution. As Mylar is a weaker material, the gas pressure would be reduced by half and correspondingly the detector array moved twice as far away from the window to take into account the lower energy loss of the beam. The resulting resolution would be better than 100 keV FWHM at almost all energies and angles, and as good as 30 keV in the zero degree detector.

Another way of improving the resolution is by redesigning the array to allow detection of the recoiling ^{24}Ne in coincidence with the corresponding α particle. Since the range of the heavy recoil is much less than that of the α particle, this requires detectors to be close

to the beam axis. Detection of both reaction products allows complete reconstruction of the reaction, in particular allowing the decay angle to be much more accurately determined from the detected energies. This in turn greatly improves the experimental resolution, eliminating the effects of both angular straggling and the limit placed on the position resolution by the detector strip size. Detailed simulations are required to quantify the resolution that would be achievable.

Both of these methods improve the experimental resolution at the cost of detection efficiency, in the first case by moving the detectors further from the interactions, and in the second by requiring coincident detections. The cross section measurement in the current work, however, allows the expected rate to be accurately predicted by simulations and thus the required beam time determined with confidence for any future proposed experiment. In addition, since the excitation function of ^{28}Mg in this work was measured with 1.5 days of beam time (see Tab. 4.1), an acceptable counting rate even with reduced efficiency should be realistically achievable.

Consideration of the decay thresholds in ^{28}Mg (Tab. 5.2) suggests that it would be of interest to extend the measured energy range to include the n+α and $2n$+α channels in order to investigate the effect that this has on the cluster structure. In particular, it is near these thresholds that molecular structures would be expected to appear. In order to investigate higher energies, a more sophisticated experimental set-up would be required with particle identification being much more important due to the large number of channels that become available between 20 and 25 MeV.

6.1.2 Theory

As discussed in section 5.2.1, better understanding of the underlying nuclear structure of the measured states will require the use of more advanced theoretical frameworks such as those discussed in chapter 2. With the measurements reported in the current work, comparisons are now possible between measured and calculated levels. Discussion of complex structures such as molecular orbitals requires the use of models that treat the

nucleons separately, and so calculations using frameworks such as AMD would be of great interest.

It is clear, however, that an understanding of the structure of ^{28}Mg will require both improved and extended experimental data, as well as theoretical work.

6.2 Outlook

The thick target inverse kinematics technique provides a powerful method for the measurement of elastic scattering cross sections, and is particularly suited to radioactive beams that require hours rather than minutes for accelerator tuning, and are typically provided with low intensities. The use of helium gas as a target allows the study of α cluster states, and with new facilities for radioactive beams such as SPIRAL2 [79] and FRIB [80] currently under construction there are excellent prospects for understanding how α clustering persists in unstable nuclei.

Bibliography

[1] R. P. Feynman, *Perfectly Reasonable Deviations from the Beaten Track*, Basic Books (2005).

[2] R. P. Feynman, *Phys. Rev.*, **76**:769–789 (1949).

[3] J. Schwinger, *Phys. Rev.*, **73**:416–417 (1948).

[4] S. G. Karshenboim, *Phys. Rep*, **422**, 12:1 – 63 (2005), ISSN 0370-1573.

[5] W. Marciano and H. Pagels, *Phys. Rep.*, **36**, 3:137–276 (1978), ISSN 0370-1573.

[6] M. Thoennessen, Discovery of nuclides project, https://people.nscl.msu.edu/~thoennes/isotopes/index.html (Accessed 2015).

[7] E. Rutherford, *Philos. Mag.*, **6**, 21 (1911).

[8] E. Rutherford, *P. Roy. Soc. Lond. A*, **97**, 686:374–400 (1920).

[9] J. Chadwick, *Nature*, **129**, 3252:312 (1932).

[10] J. Chadwick, *P. Roy. Soc. Lond. A*, **142**, 846:1–25 (1933).

[11] K. S. Krane, *Introductory Nuclear Physics*, Wiley (1988).

[12] C. F. Weizsäcker, *Z. Phys.*, **96**:431–458 (1935).

[13] M. Freer, *Rep. Prog. Phys.*, **70**:2149–2210 (2007).

[14] W. von Oertzen, M. Freer and Y. Kanada-En'yo, *Phys. Rep.*, **432**, 2:43–113 (2006), ISSN 0370-1573.

[15] B. R. Fulton, *Contemp. Phys.*, **40**, 5:299–311 (1999).

[16] M. Freer and H. O. U. Fynbo, *Prog. Part. Nucl. Phys.*, **78**:1–23 (2014).

[17] M. G. Mayer, *Phys. Rev.*, **75**, 12:1969–1970 (1949).

[18] E. Caurier, G. Martinez-Pinedo, F. Nowacki, A. Poves and A. Zuker, *Rev. Mod. Phys.*, **77**, 2:427–488 (2005), ISSN 0034-6861.

[19] R. Machleidt, *Phys. Rev. C*, **63**, 2 (2001), ISSN 0556-2813.

[20] P. Navratil, J. P. Vary and B. R. Barrett, *Phys. Rev. Lett.*, **84**, 25:5728–5731 (2000), ISSN 0031-9007.

[21] A. H. Wapstra, G. Audi and C. Thibault, *Nucl. Phys. A*, **729**:129–336 (2003).

[22] G. Audi, A. H. Wapstra and C. Thibault, *Nucl. Phys. A*, **729**:337–676 (2003).

[23] Tz. Kokalova, Private communication.

[24] K. Ikeda, N. Tagikawa and H. Horiuchi, *Prog. Theor. Phys.*, pages 464–475 (1968).

[25] D. M. Brink and B. E, *Nucl. Phys. A*, **91**:1–26 (1967).

[26] H. T. Richards, *Phys. Rev. C*, **29**, 1:276–283 (1984).

[27] B. Buck, J. C. Johnston, A. C. Merchant and S. M. Perez, *Phys. Rev. C*, **52**:1840–1844 (1995).

[28] A. Astier, P. Petkov, M. Porquet, D. S. Delion and P. Schuck, *Phys. Rev. Lett.*, **104**, 4 (2010), ISSN 0031-9007.

[29] S. Marsh and W. Rae, *Phys. Lett. B*, **180**, 3:185–190 (1986), ISSN 0370-2693.

[30] Y. Kanada-En'yo and H. Horiuchi, *Prog. Theor. Phys. Suppl.*, **142**:205 (2001).

[31] Y. Kanada-En'yo, M. Kimura and H. Horiuchi, *C. R. Physique*, **4**:497 (2003).

[32] W. von Oertzen, *Eur. Phys. J. A*, **11**:403–411 (2001).

[33] G. V. Rogachev *et al.*, *Phys. Rev. C*, **64**, 051302 (2001).

[34] M. Kimura, *Phys. Rev. C*, **75**, 3 (2007), ISSN 0556-2813.

[35] E. P. Wigner and L. Eisenbud, *Phys. Rev.*, **72**, 1:29–41 (1947).

[36] A. M. Lane and R. G. Thomas, *Rev. Mod. Phys.*, **30**, 2:257–353 (1958).

[37] I. J. Thompson and F. M. Nunes, *Nuclear Reactions for Astrophysics: Principles, Calculation and Applications of Low-Energy Reactions*, Cambridge University Press (2009).

[38] M. Abramowitz and I. A. Stegun, *Handbook of Mathematical Functions*, National Bureau of Standards (1964).

[39] C. R. Brune, *Phys. Rev. C*, **66**, 044611 (2002).

[40] C. Detraz, *Nature*, **325**:291–3 (1985).

[41] National Nuclear Data Center, The Chart of Nuclides, http://www.nndc.bnl.gov/chart/ (Accessed 2012).

[42] R. K. Sheline and N. R. Johnson, *Phys. Rev.*, **89**, 2:520–521 (1953).

[43] M. Thoennessen, *At. Data Nucl. Data Tables*, **98**, 5:933–959 (2012).

[44] B. Rastegar, G. Guillaum, P. Fintz and A. Gallmann, *Nuc. Phys. A*, **225**:80–92 (1974).

[45] T. Fisher, T. Bardin, J. Becker, L. Chase, D. Kohler, R. McDonald, A. Poletti and J. Pronko, *Phys. Rev. C*, **7**, 5 (1973).

[46] R. Middleton and D. Pullen, *Nuc. Phys.*, **51**:77 (1964).

[47] S. Hinds, H. Marchant and R. Middleton, *Proc. Phys. Soc.*, **4**:473 (1961).

[48] K. Kura *et al.*, *Phys. Rev. C*, **85**, 034310 (2012).

[49] D. Guillemaud-Mueller, C. Détraz, M. Langevin, F. Naulin, M. de Saint-Simon, C. Thibault, F. Touchard and M. Epherre, *Nucl. Phys. A*, **426**:37 (1984).

[50] C. Détraz, D. Guillemaid, G. Huber, R. Klapisch, M. Langevin, F. Naulin, C. Thibault, L. Carraz and F. Touchard, *Phys. Rev. C*, **19**, 1 (1979).

[51] GANIL, Chart of beams, http://www.ganil-spiral2.eu/ (Accessed 2015).

[52] GANIL, http://www.ganil-spiral2.eu/ (Accessed 2012).

[53] A. C. C. Villari, *Nucl. Inst. Meth. B*, **204**:31–41 (2003).

[54] K. P. Artemov *et al.*, *Sov. J. Nucl. Phys.*, **52**, 3:408–411 (1990), ISSN 0038-5506.

[55] Micron Semiconductor W1 Specification, http://www.micronsemiconductor.co.uk/pdf/w1.pdf.

[56] N. Curtis and J. Walshe, *Nucl. Instrum. Meth. A*, **797**:44–56 (2015).

[57] T. Davinson *et al.*, *Nucl. Instrum. Meth. A*, **454**:350–358 (2000).

[58] V. Pucknell and S. Letts, MIDAS, http://npg.dl.ac.uk/MIDAS/ (2011).

[59] Goodfellow group, http://www.goodfellow.com/ (Accessed 2012).

[60] H. Geissel, C. Scheidenberger, P. Malzacher, J. Kunzendorf and H. Weick, ATIMA energy loss code, https://web-docs.gsi.de/~weick/atima/ (Accessed 2015).

[61] J. F. Ziegler, *The Stopping and Range of Ions in Solids*, Pergamon Press (1985).

[62] O. B. Tarasov, D. Bazin, M. Lewitowicz and O. Sorlin, Lise++, http://lise.nscl.msu.edu/lise.html (Accessed 2012).

[63] Armstrong, Chandler and Manning, de/dx, http://npg.dl.ac.uk/Charissa/documents/CODES/dedx/ (Accessed 2012).

[64] R. Abegg and C. A. Davis, *Phys. Rev. C*, **43**, 6:2523–2540 (1991).

[65] Engauge digitizer, http://digitizer.sourceforge.net/ (Accessed 2015).

[66] R. E. Azuma *et al.*, *Phys. Rev. C*, **81**, 045805 (2010).

[67] T. Rauscher, *Phys. Rev. C*, **81**, 045807 (2010).

[68] C. Wheldon, ckin, Private communication.

[69] Cern program library, https://cernlib.web.cern.ch/cernlib/ (Accessed 2015).

[70] T. Vertse, K. F. Pal and Z. Balogh, *Comput. Phys. Commun.*, **27**, 3:309–322 (1982).

[71] R. D. Woods and D. S. Saxon, *Phys. Rev.*, **95**, 2:577–578 (1954).

[72] K. Wildermuth and Y. C. Tang, *A Unified Theory of the Nucleus*, Academic Press (1977).

[73] K. Baktybayev, A. Dalelkhankyzy and N. Koilyk, *Adv. Stud. Theor. Phys.*, **8**, 28:1205–1212 (2014).

[74] W. SiMin, X. Chen, R. J. Liotta, Q. Chong, X. FuRong and J. DongXing, *Sci. China. Phys. Mech. Astron.*, **54**, 1:S130–S135 (2011), ISSN 1674-7348.

[75] A. Soylu, Private communication.

[76] G. R. Satchler and W. G. Love, *Phys. Rep.*, **55**, 3:183–254 (1979), ISSN 0370-1573.

[77] B. Buck, A. C. Merchant and S. M. Perez, *Phys. Rev. C*, **45**, 5 (1992).

[78] Y. Kanada-EnYo, *Frontiers of Collective Motions*, pages 254–259 (2003).

[79] M. Lewitowicz, *Nucl. Phys. A*, **805**:519C–525C (2008), 23rd International Nuclear Physics Conference, Tokyo Int Forum, Tokyo, Japan, Jun 03-08, 2007.

[80] G. Bollen, in Y. E. Penionzhkevich and S. M. Lukyanov, editors, *International Symposium on Exotic Nuclei 2009*, volume 1224 of *AIP Conference Proceedings*, pages 432–441 (2010), 5th International Symposium on Exotic Nuclei, Sochi, Russia, Sep 28-Oct 02, 2009.